ULTRASONIC TOPOGRAPHICAL AND PATHOTOPOGRAPHICAL ANATOMY

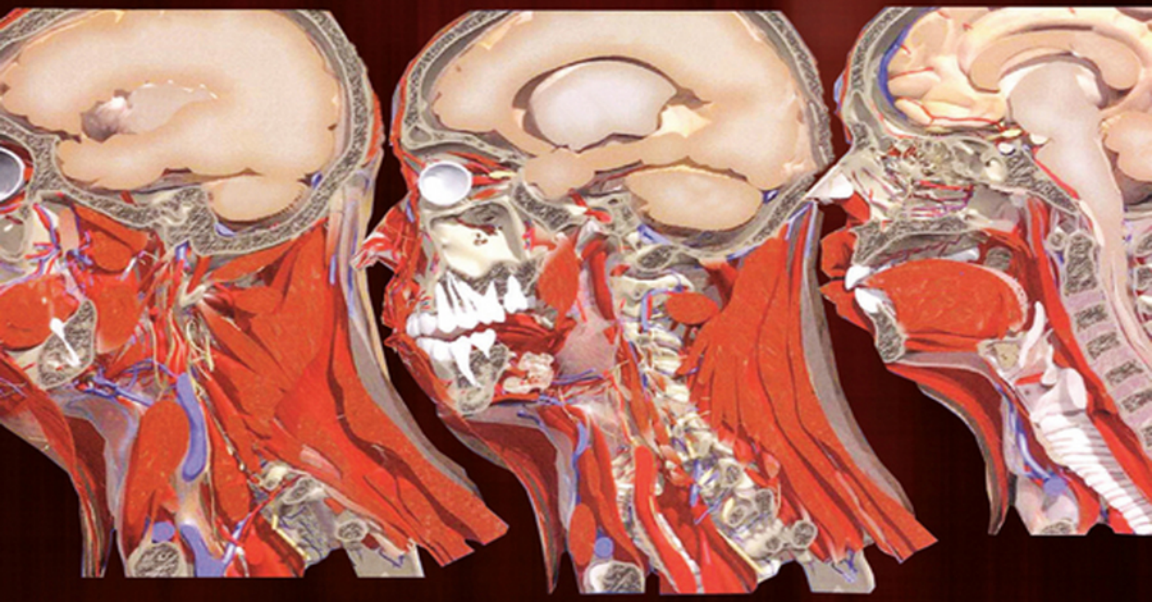

A COLOR ATLAS

Z. M. SEAGAL
O. M. SURNINA

Scrivener Publishing

WILEY

Ultrasonic Topographical and Pathotopographical Anatomy

Scrivener Publishing
100 Cummings Center, Suite 541J
Beverly, MA 01915-6106

Publishers at Scrivener
Martin Scrivener (martin@scrivenerpublishing.com)
Phillip Carmical (pcarmical@scrivenerpublishing.com)

Ultrasonic Topographical and Pathotopographical Anatomy

A Color Atlas

Z. M. Seagal and O. M. Surnina

WILEY

Copyright © 2016 by Scrivener Publishing LLC. All rights reserved.

Co-published by John Wiley & Sons, Inc. Hoboken, New Jersey, and Scrivener Publishing LLC, Salem, Massachusetts.
Published simultaneously in Canada.

No part of this publication may be reproduced, stored in a retrieval system, or transmitted in any form or by any means, electronic, mechanical, photocopying, recording, scanning, or otherwise, except as permitted under Section 107 or 108 of the 1976 United States Copyright Act, without either the prior written permission of the Publisher, or authorization through payment of the appropriate per-copy fee to the Copyright Clearance Center, Inc., 222 Rosewood Drive, Danvers, MA 01923, (978) 750-8400, fax (978) 750-4470, or on the web at www.copyright.com. Requests to the Publisher for permission should be addressed to the Permissions Department, John Wiley & Sons, Inc., 111 River Street, Hoboken, NJ 07030, (201) 748-6011, fax (201) 748-6008, or online at http://www.wiley.com/go/permission.

Limit of Liability/Disclaimer of Warranty: While the publisher and author have used their best efforts in preparing this book, they make no representations or warranties with respect to the accuracy or completeness of the contents of this book and specifically disclaim any implied warranties of merchantability or fitness for a particular purpose. No warranty may be created or extended by sales representatives or written sales materials. The advice and strategies contained herein may not be suitable for your situation. You should consult with a professional where appropriate. Neither the publisher nor author shall be liable for any loss of profit or any other commercial damages, including but not limited to special, incidental, consequential, or other damages.

For general information on our other products and services or for technical support, please contact our Customer Care Department within the United States at (800) 762-2974, outside the United States at (317) 572-3993 or fax (317) 572-4002.

Wiley also publishes its books in a variety of electronic formats. Some content that appears in print may not be available in electronic formats. For more information about Wiley products, visit our web site at www.wiley.com.

For more information about Scrivener products please visit www.scrivenerpublishing.com.

Cover design by [To come]

Library of Congress Cataloging-in-Publication Data:

ISBN 978-1-119-22357-3

Printed in the United States of America

10 9 8 7 6 5 4 3 2 1

Abstract

A new description of the ultrasonic topographical and pathotopographical anatomy of the head, neck, chest, anterolateral abdominal wall, abdominal organs, retroperitoneal space, male and female pelvises, and lower extremities is presented.

Specific and non-specific ultrasonic symptoms are suggested for normal and abnormal developmental variants, diffuse and local pathotopographical anatomy. The color atlas contains comparative topographical and pathotopographical data. This atlas is the first manual of its kind for students and medical specialists in different areas, including those specializing in medical sonography. The original technology was tested at clinics in patients subjected to ultrasonic monitoring. Because of early detection there were no false-positive or false-negative results. The therapy was effective; in some cases, the use of the original method of "seagalography" (optometry and pulsemotorgraphy) has made it possible to develop new methods of treatment and/or to determine the optimal doses of drugs, as well as to develop effective drug complexes for treatment of a given pathology.

The monograph is intended to be used by physicians, junior physicians, medical residents, lecturers in medicine, and medical students.

Contents

Preface

N. I. Pirogov, the founder of topographical anatomy, introduced the term "surgical anatomy" for the location and interaction of organs and tissues in surgical diseases. Surgical anatomy is changed during surgery as a result of the surgeon's activity. At certain stages of operation the tissue patterns are invariable, i.e., the topographical anatomy is observed. In other areas, normal topographical anatomy is converted into pathotopographical anatomy.

Presently, the problem of atraumatic visualization of topographical and pathotopographical anatomy is fairly urgent for practical medicine for the purposes of differentiation between norm and pathology, variants of the norm, and specific and non-specific variants of pathotopography. The method of ultrasonic topographical and pathotopographical anatomy developed by the authors of this monograph provides an opportunity for solving this problem.

During the last decade we have used this method to study normal and pathological topographoanatomical structures of the human body and development anomalies. Specific features of topographical anatomy due to inflammatory processes, obstruction of tubular organs, in tissues modified as a result of dystrophy, obesity, tuberculosis, and tumor have been determined. Layer-by-layer ultrasonic topography, holotopy, and syntopy have been studied. The data obtained in this work were compared with the conventional topographical data, as well as the results obtained by functional methods of optometry and pulsomotorgraphy developed by Prof. Z. M. Seagal.

It is important to note that a living human body was tested both in the norm and pathology. This provides more reliable diagnosis,

development of sparing operations, and atraumatic and effective control of therapy.

Further development of ultrasonic topography and pathotopography should be focused on typical anatomy, i.e., the study of distribution of tissues and systems within the human body, as well as location of organs and parts of the body. It was noted that people with a certain constitution and of a definite age had an extreme type of structure and location of organs. The importance of ultrasonic scanning for the typical anatomy is that it provides differentiation between the age norm and the pathology.

For the first time ultrasonic topographical anatomy was used for diagnosis in studies of this kind, in full accordance with the physician's motto "to treat the patient rather than the disease".

Ultrasonic topographical anatomy contributes to differentiating congenital defects that could necessitate urgent treatment.

In addition to development of new topographical and pathotopographical human anatomy, we acquired the experience in teaching this discipline to physicians of various specialties. It was taught to interns, junior physicians, medical residents, and medical students, as well as specialists in surgery, traumatology, neurosurgery, oncology, urology, obstetrics and gynecology, dental surgery, anesthesiology, and other medical specialists concerned with different topographical and anatomical structures (neurologists, dentists, ophthalmologists, pathologists, forensic medical examiners, etc.).

This color atlas of ultrasonic topographical and pathotopographical anatomy is an original scientific manual intended to be used by physicians of different specialties in their everyday work.

About the Authors

Zoltan M. SEAGAL, Doctor of Medicine, Honorary Academic of the Izhevsk State Medical Academy, Honored Scientific Worker of Russia, three Soros Professor Awards, Director of the Department of Topographical Anatomy and Operative Surgery at the Izhevsk State Medical Academy

Olga V. SURNINA, Ph. D. (Medicine), Highest Category Physician, Chief non-staff expert on medical ultrasound of the Ministry of Health of the Udmurt Republic, President of the Association of Sonographers (Udmurt Republic), Director of the Ultrasound Diagnosis Department at the Republican Clinic Diagnostic Center, Senior Teacher in the Department of Topographical Anatomy and Operative Surgery (Izhevsk State Medical Academy).

Topography and Pathotopography of the Head

The chapter on the ultrasonic topography and pathotopographical anatomy of the head includes layer-by-layer topography of the visceral and cerebral craniums with the cross-sectional imaging of the head.

Ultrasonic images of external and internal bone lamellae, vessels of the subcutaneous layer, skin, and subcutaneous fat, depressed compression and linear fractures are demonstrated. Ultrasonic images of the medial cerebral artery, infundibulum, posterior communicating artery, pons cerebelli, medulla oblongata, anterior inferior cerebellar artery, basilar artery, anterior cerebral artery, posterior cerebral artery, and olfactory tract are verified based on the topographical anatomy of the basilar region of the cranium.

The deep facial area contains the internal wing muscle, mandibulum, and submandibular salivary gland; the oral cavity contains the tongue, peripharyngeal space, and posterior veil of the soft palate, as well as the

superficial temporal artery, auriculotemporal nerve, maxillary artery, and middle meningeal artery. The ultrasonic images of the internal and external muscles are shown.

Images of the parotid gland, superficial cervical lymph nodes, and common carotid artery are presented.

Linear fracture is associated with the external bone lamella of the area of intact bone, with the intracranial space, and the hypoechogenic track. Under conditions of tamponade of the fourth ventricle of cerebrum with transition to the pons cerebelli, a blood clot is revealed in the vicinity of the clinoid plate at the pyramid apex of the temporal bone. The intraventricular blood clot can be pathotopographically associated with the left lateral ventricle, whereas liquid blood is observed at the lumen of the right lateral ventricle.

The atlas also contains images of the pathotopographical anatomy of the intraventricular hemorrhage, hematoma in the thalamus, fronto-basal intracerebral hematoma, and acute epidural hematoma in the left parieto-occipital space accompanied by the phenomenon of the "boundary amplification".

Thus, the ultrasonic topographic anatomy of the head provides the basis for the research into the pathotopographical anatomy of a given pathology and determines specific diagnostic features of injuries and/or volume structures.

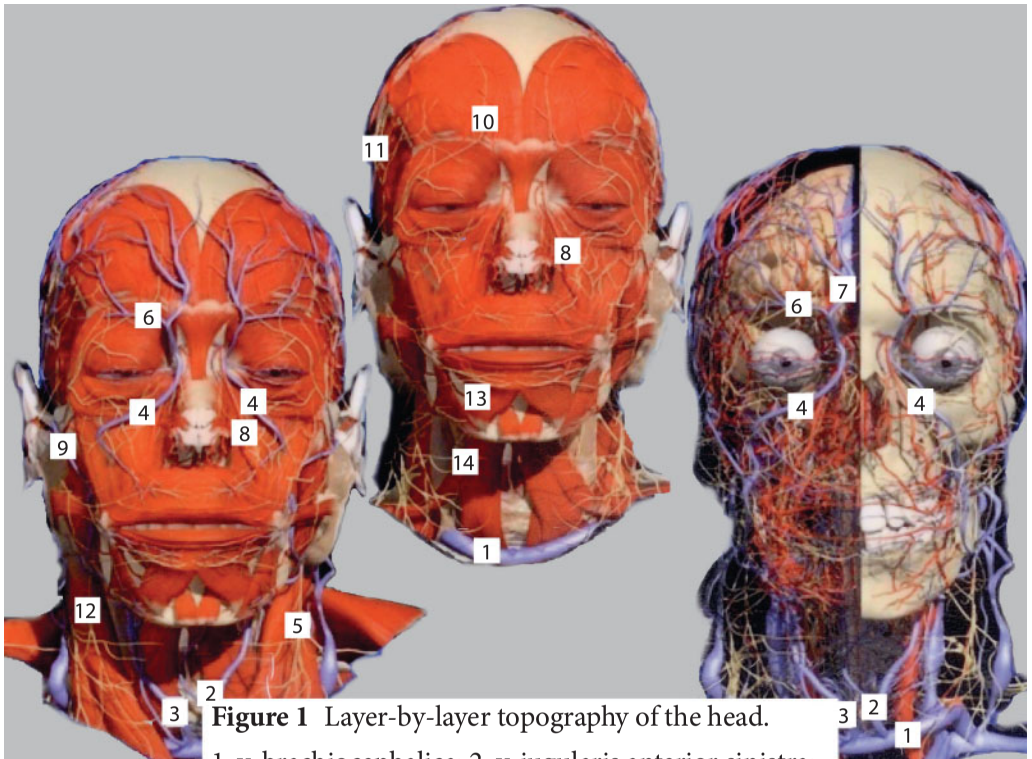

Figure 1 Layer-by-layer topography of the head.

1. v. brachiocephalica; 2. v. jugularis anterior sinistra; 3. v. jugularis anterior dextra; 4. v. angularis; 5. Plexus cervicalis; 6. v. supratrochlearis; 7. v. nasofrontalis; 8. a. angularis; 9. v. temporalis superlicialis; 10. n. supraorbitalis; 11. n. auriculotemporalis; 12. Plexus cervixalis; 13. m. depressor labii inferioris; 14. m. dieastricus (venter anterior).

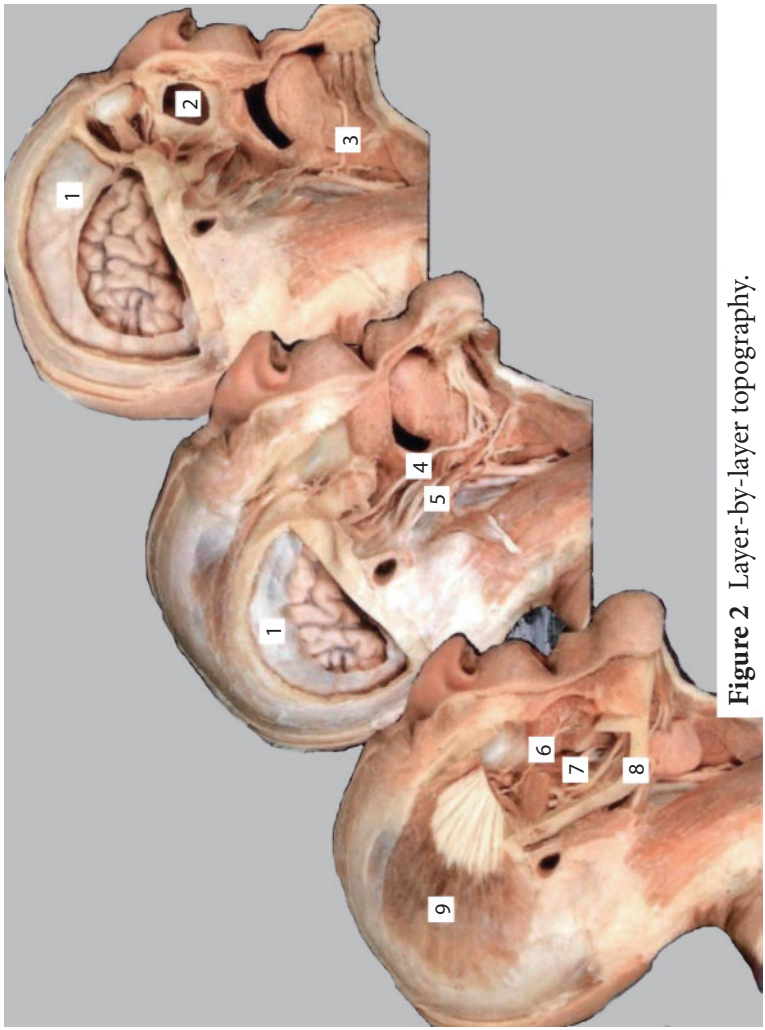

Figure 2 Layer-by-layer topography.
1. Falx cerebri; 2. Sinus maxillaries; 3. n. hypoglossus; 4. n. hypoglossus; 5. n. facialis; 6. n. lingualis; 7. n. alveolaris inferior; 8. Arcus maxillae inferioris; 9. m. temporalis

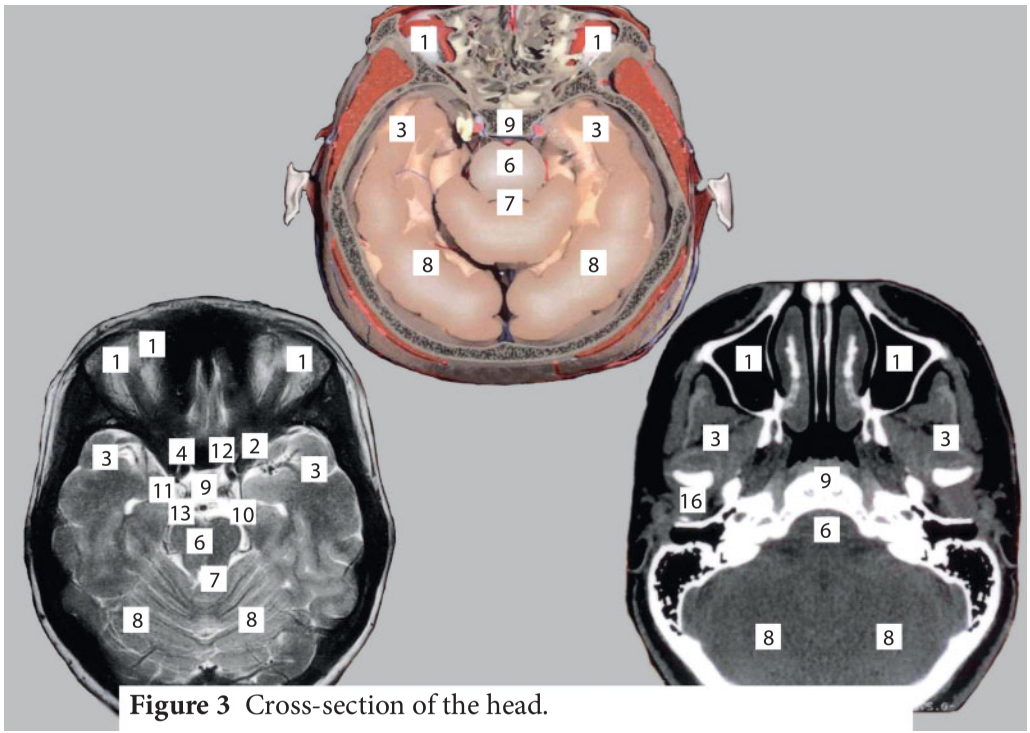

Figure 3 Cross-section of the head.

1. Eye bulb; 2. Optic nerve; 3. Temporal lobe; 4. Internal carotid artery; 6. Pons varolii; 7. Ventricle of the brain IV; 8. Cerebellar hemisphere; 9. Optic nerve; 10. Visual tract; 11. Middle cranial fossa; 12. Temporal lobe of cerebral hemisphere; 13. Ephippium; 16. Temporal gyrus.

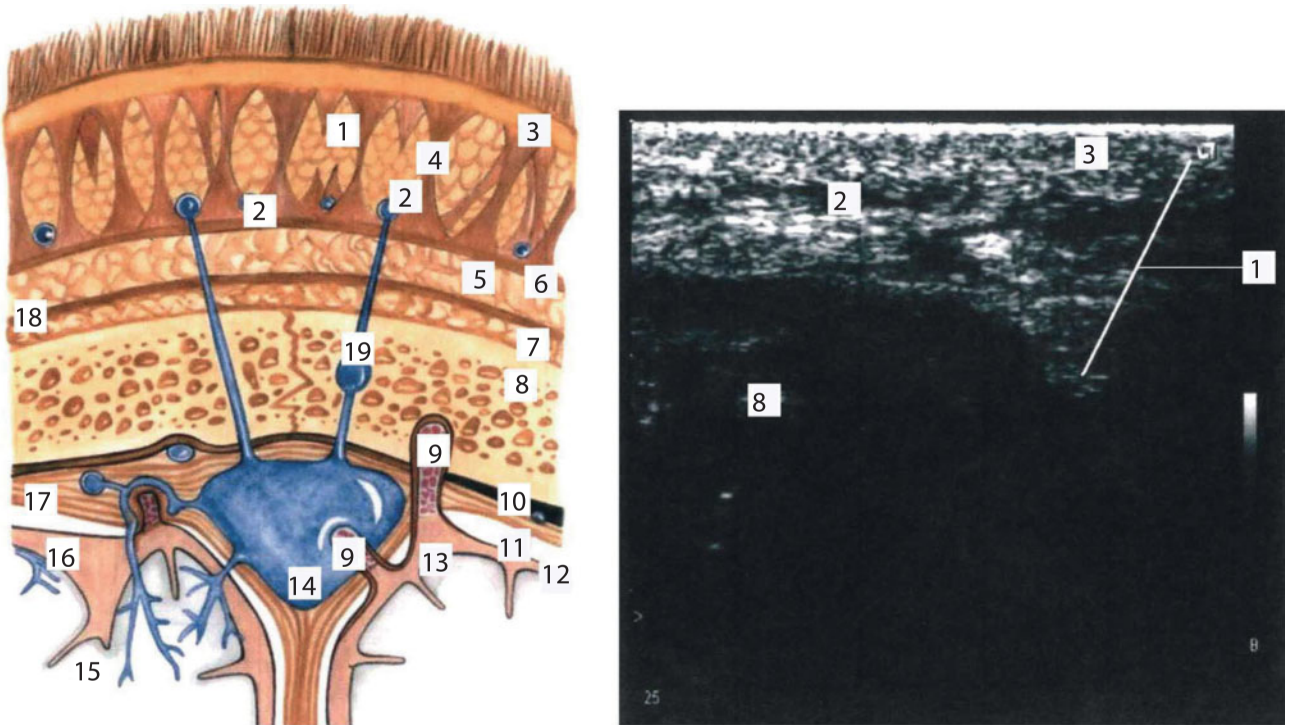

Figure 4 Comparative ultrasonic topographical anatomy of the head.

1. Subcutaneous tissue; 2. Vessels of the subcutaneous layer; 3. Skin; 5. Subgaleal cellular tissue; 8. Bone.

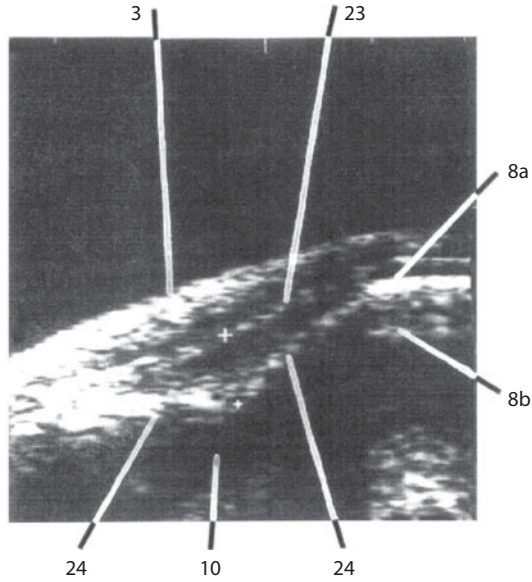

Figure 5 Hollow depressed fracture.

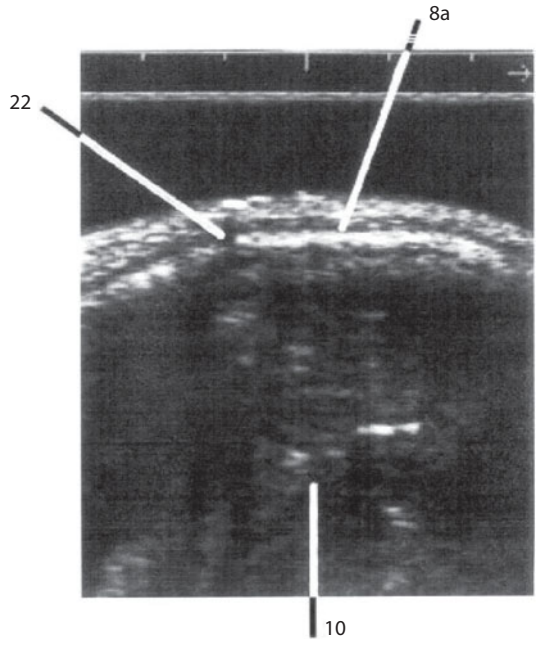

Figure 6 Linear fracture.

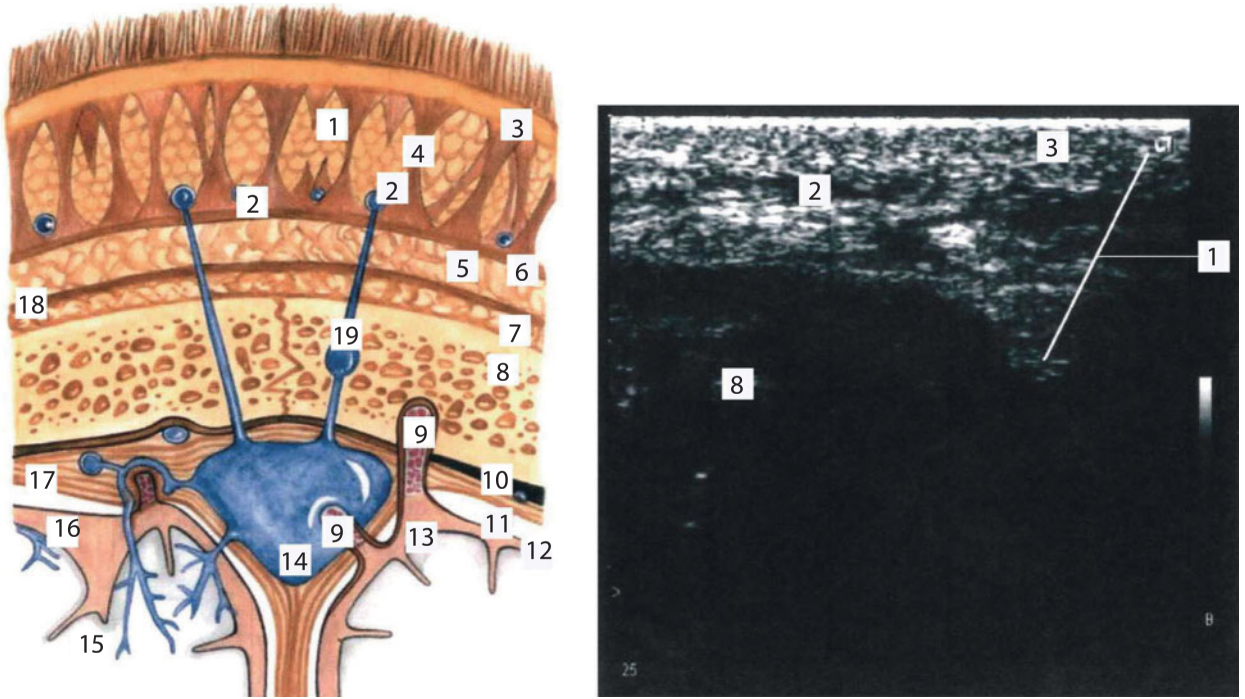

Figure 7 Layer-by-layer ultrasonic topographical anatomy of the head.

1. Subcutaneous tissue; 2. Vessels of the subcutaneous layer; 3. Skin; 4. Tendinous intersections; 5. Subgaleal cellular tissue; 6. Aponeurosis; 7. Subperiosteal cellular tissue; 8. Bone; 9. Pacchionian granulations; 10. Epidural cavity; 11. Subdural space; 12. Arachnoid membrane; 13. Choroid; 14. Venous sinus; 15. Encephalon; 16. Subarachnoid space; 17. Dura mater; 18. Periosteal coverage; 19. Diploic vein and draining vein.

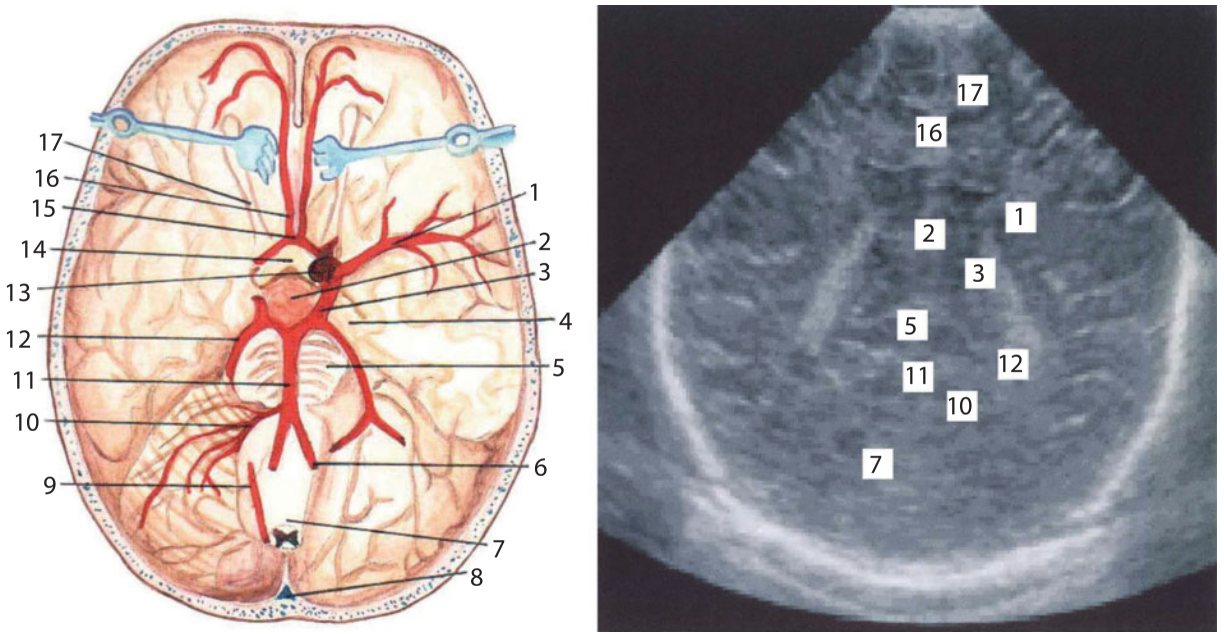

Figure 8 Basilar region of the cranium.

1. Medial cerebral artery; 2. Infundibulum; 3. Posterior communicating artery; 4. Cerebral peduncles; 5. Pons cerebelli; 6. Vertebral artery; 7. Medulla oblongata; 8. Occipital sinus; 9. Posterior inferior artery of cerebellum; 10. Anterior inferior artery of cerebellum; 11. Basilar artery; 12. Posterior cerebral artery; 13. Interior carotid artery; 14. Optic chiasma; 15. Anterior communicating artery; 16. Anterior cerebral artery; 17. Olfactory tract.

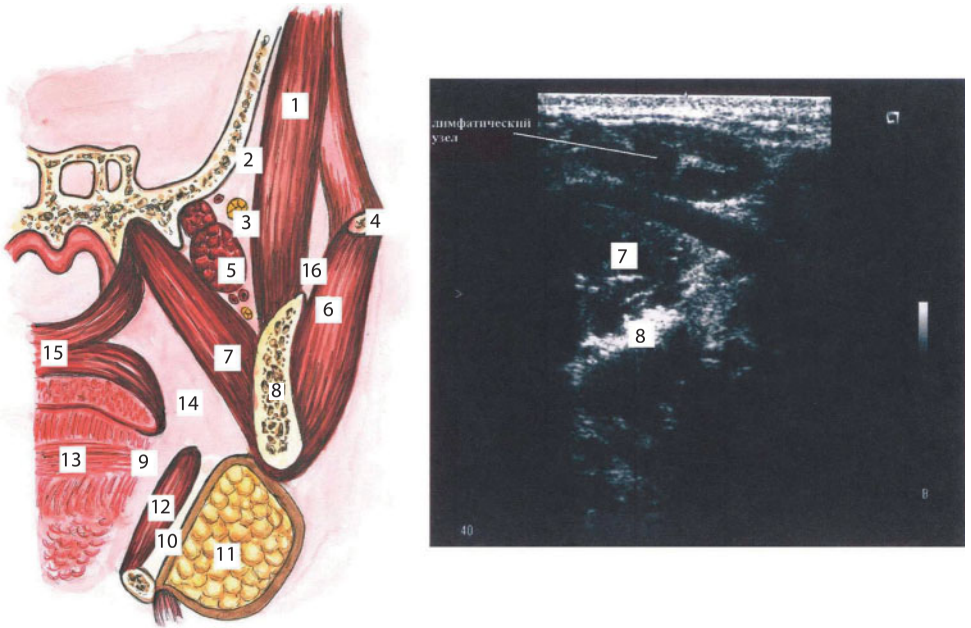

Figure 9 Deep facial area.

1. Temporal muscle; 2. Temporal pterygoid space; 3. Buccal nerve; 4. Arcus zygomaticus; 5. Exterior pterygoid muscle; 6. Masticatory muscle; 7. Interior pterygoid muscle; 8. Mandible; 9. Subglossal cellular space; 10. Bed of submandibular salivary gland; 11. Submandibular salivary gland; 12. Mylohyoid muscle; 13. Tongue; 14. Peripharyngeal space; 15. Soft palate; 16. Masticator maxillary space.

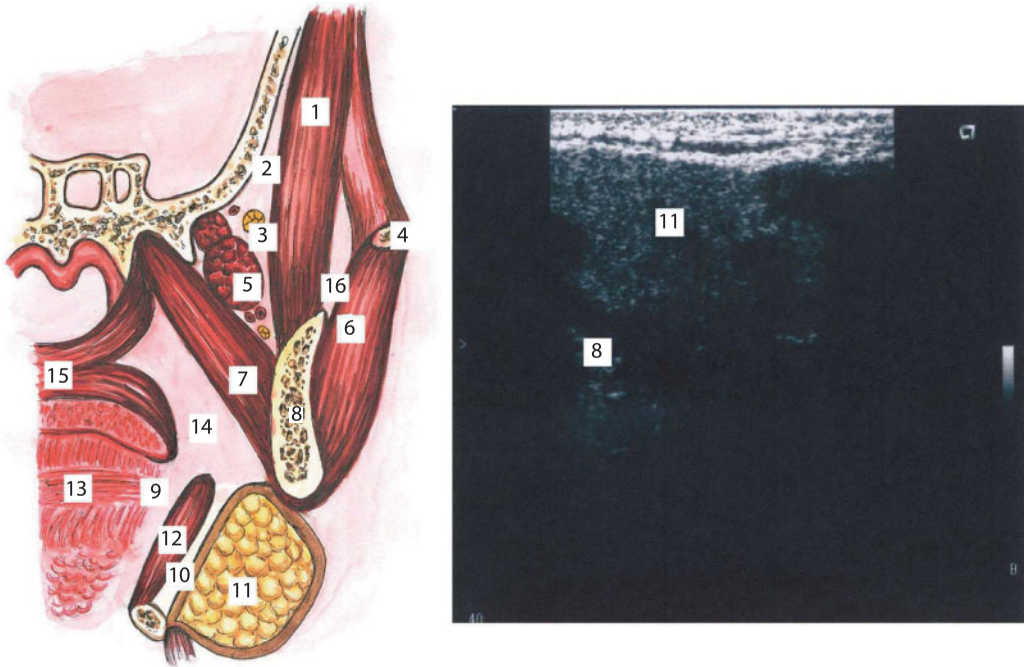

Figure 10 Facial area of the head.

1. Temporal muscle; 2. Temporal pterygoid space; 3. Buccal nerve; 4. Arcus zygomaticus; 5. Exterior pterygoid muscle; 6. Masticatory muscle; 7. Interior pterygoid muscle; 8. Mandible; 9. Subglossal cellular space; 10. Bed of submandibular salivary gland; 11. Submandibular salivary gland; 12. Mylohyoid muscle; 13. Tongue; 14. Peripharyngeal space; 15. Soft palate; 16. Masticator maxillary space.

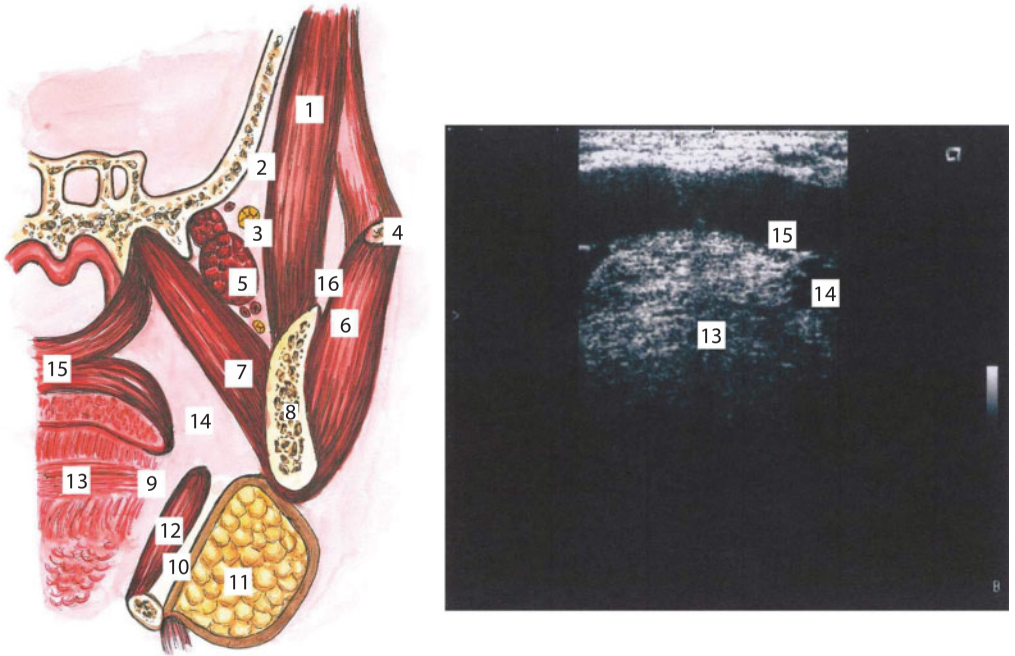

Figure 11 Infratemporal fossa.

1. Temporal muscle; 2. Temporal pterygoid space; 3. Buccal nerve; 4. Arcus zygomaticus; 5. Exterior pterygoid muscle; 6. Masticatory muscle; 7. Interior pterygoid muscle; 8. Mandible; 9. Subglossal cellular space; 10. Bed of submandibular salivary gland; 11. Submandibular salivary gland; 12. Mylohyoid muscle; 13. Tongue; 14. Peripharyngeal space; 15. Soft palate; 16. Masticator maxillary space.

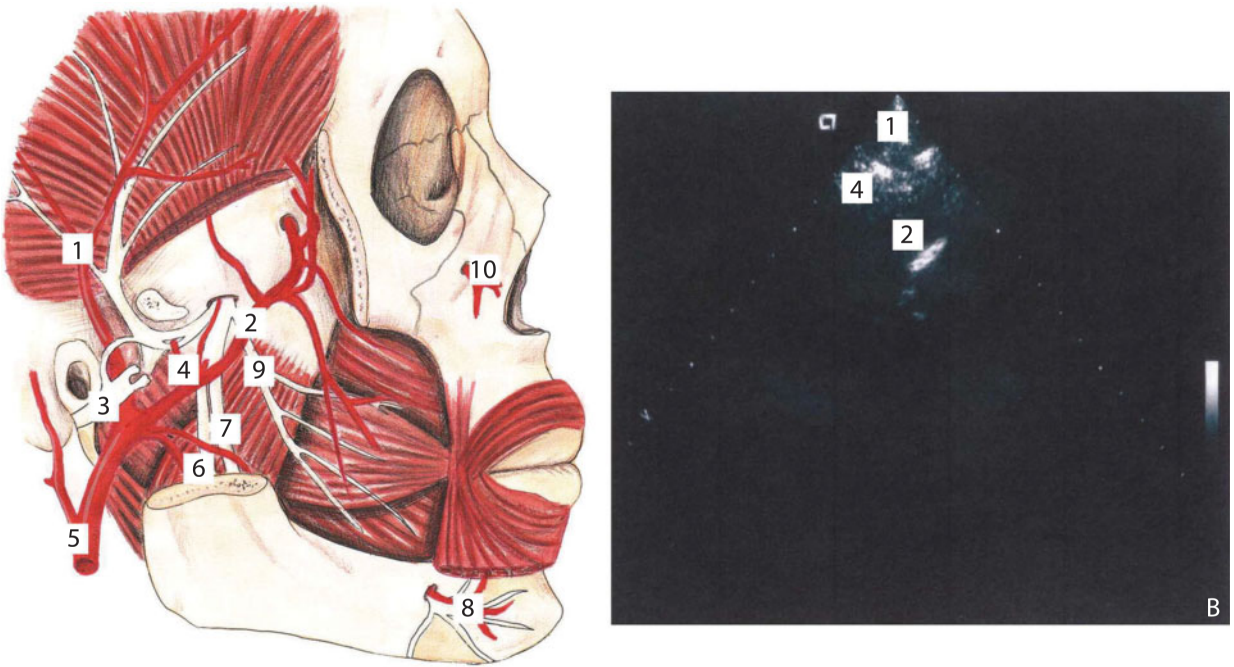

Figure 12 Maxillary artery with medial meningeal artery and superficial temporal artery.

1. Superficial temporal artery and auriculotemporal nerve; 2. Internal maxillary artery; 3. Facial nerve; 4. Medial meningeal artery; 5. Exterior carotid artery; 6. Inferior alveolar nerve; 7. Lingual nerve; 8. Submental artery and nerve; 9. Buccal nerve; 10. Suborbital artery.

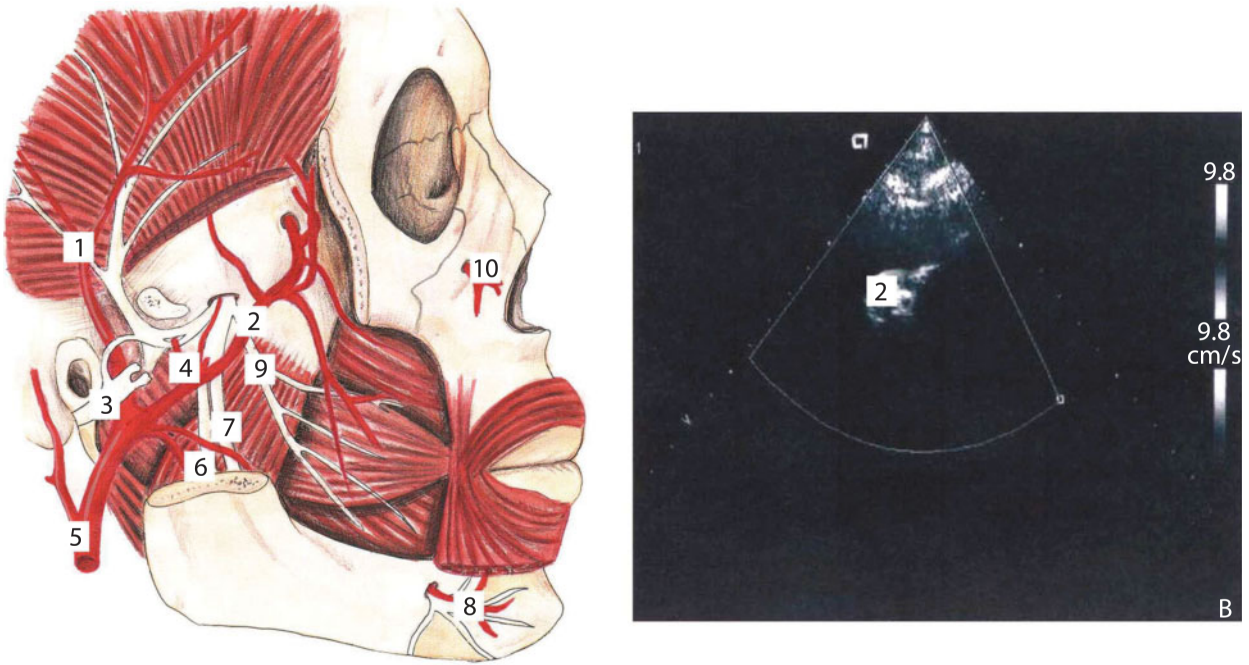

Figure 13 Maxillary artery.

1. Superficial temporal artery and auriculotemporal nerve; 2. Maxillary artery; 3. Facial nerve; 4. Medial meningeal artery; 5. Exterior carotid artery; 6. Inferior alveolar nerve; 7. Lingual nerve; 8. Submental artery and nerve; 9. Buccal nerve; 10. Suborbital artery.

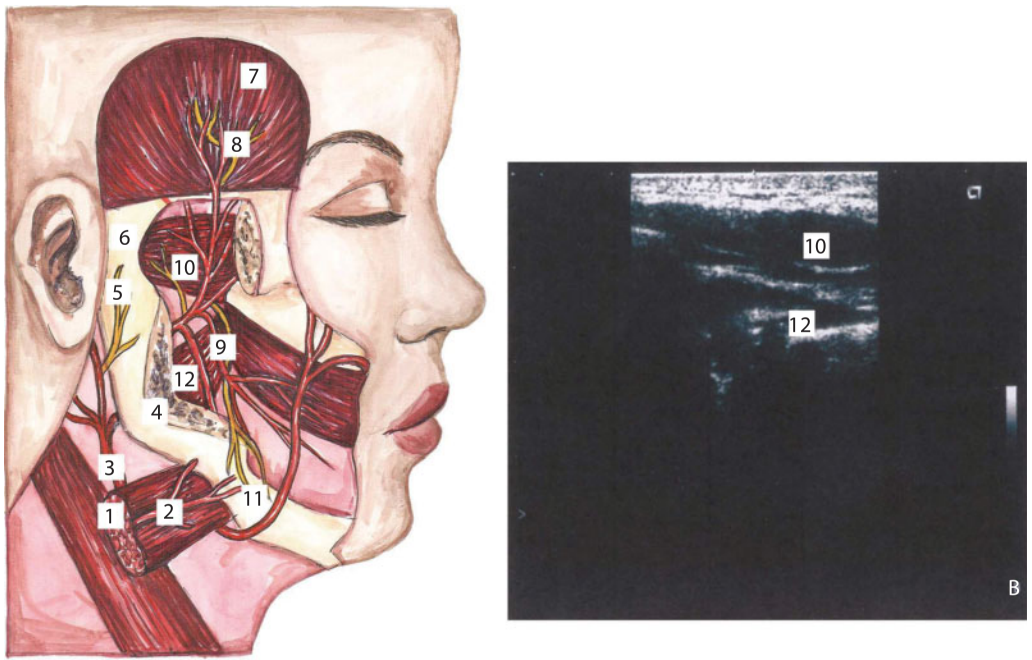

Figure 14 Mastication muscles.

1. M. masseter; 2. A. masseterica; 3. A. carotis externa; 4. Mandibular dipole; 5. N. auriculotemporalis; 6. Collum mandibulae; 7. M. temporalis; 8. A. et n. temporalis profunda; 9. A. buccalis; 10. M. pterigoideus externus; 11. Ramus marginalis mandibulae; 12. M. pterigoideus internus.

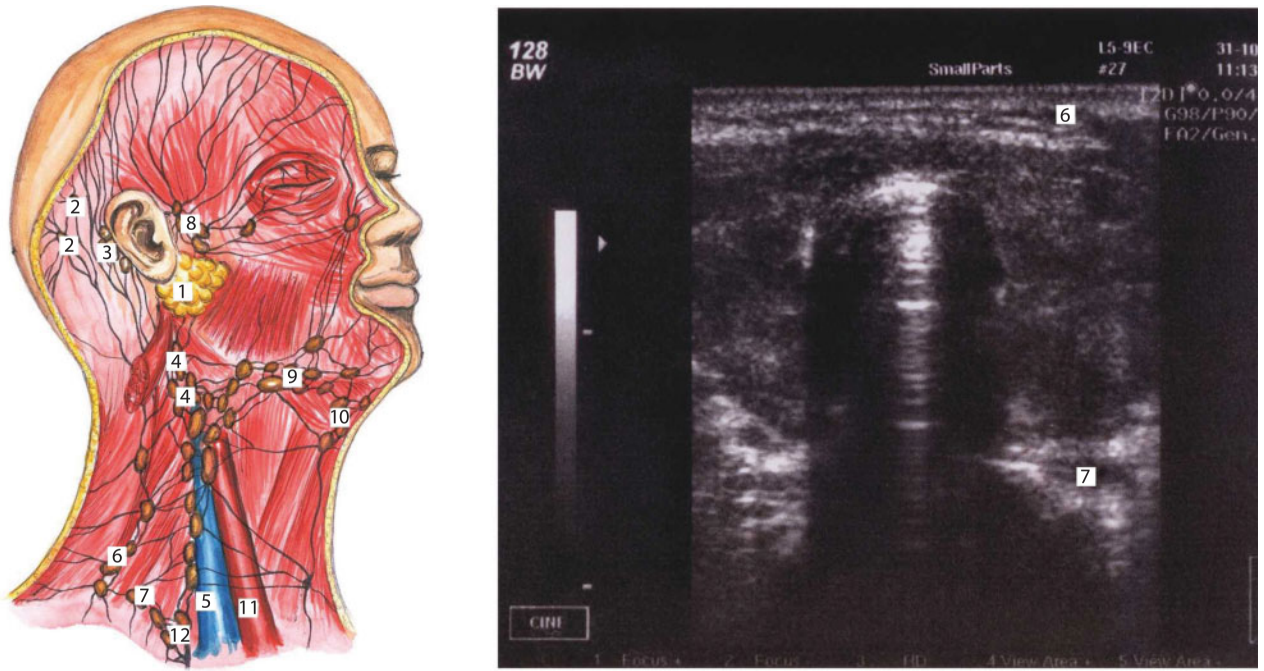

Figure 15 Lymphatic system of the head and neck.

1. Parotid gland; 2. Occipital lymph nodes; 3. Posterior auricular lymph nodes; 4. Deep superior cervical glands; 5. Internal jugular; 6. Superficial cervical glands; 7. Deep inferior cervical glands; 8. Anterior auricular lymph nodes; 9. Mandibular lymph nodes; 10. Submental lymph nodes; 11. Common carotid artery; 12. Right jugular lymph trunk.

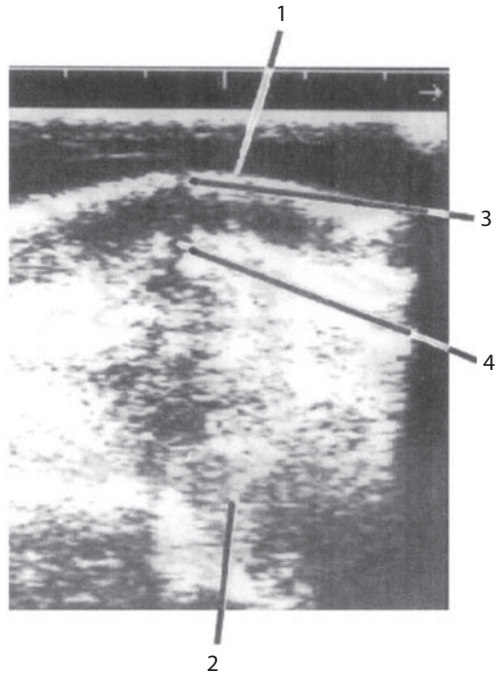

Figure 16 Linear fracture.

1. External bone lamella at the region of intact bone; 2. Intracranial space; 3. Linear fracture; 4. Hypoechogenic track.

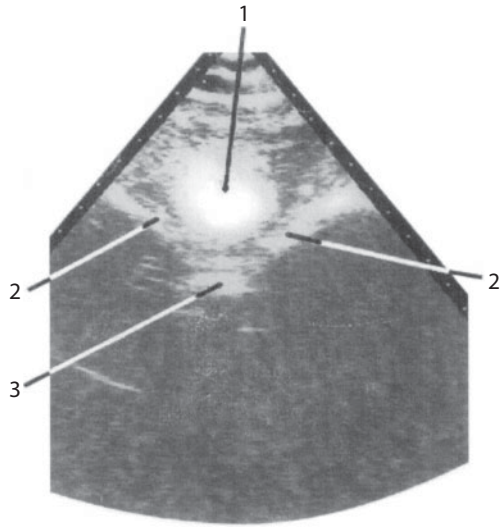

Figure 17 Tamponade of the ventricle of the brain IV with transition to pons cerebelli.

1. Blood clot; 2. Pyramid apex of the temporal bone; 3. Clinoid plate.

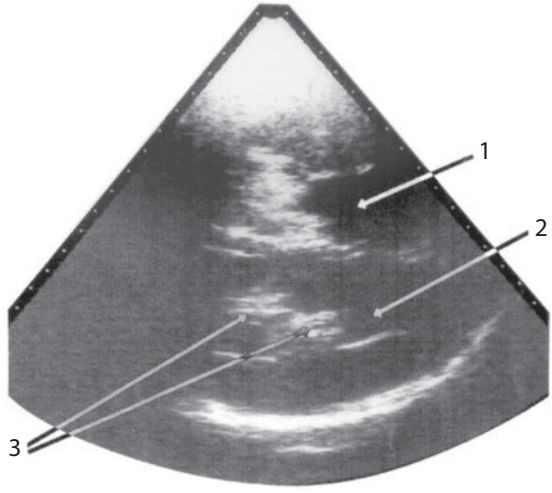

Figure 18 Intraventricular blood clot.

1. Left lateral ventricle; 2. Liquid blood in the lumen of the right lateral ventricle; 3. Blood clot.

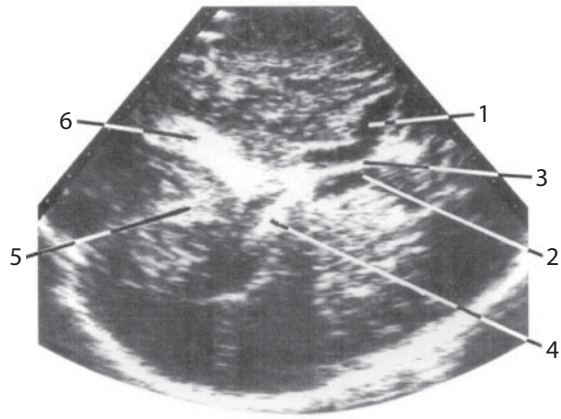

Figure 19 Intraventricular hemorrhage.

1. Anterior horn of the homolateral side ventricle; 2. Anterior horn of the contralateral side ventricle; 3. Pellucid septum; 4. Vascular plexus; 5. Longitudinal fissure of cerebrum; 6. Blood clot in the posterior regions of the right lateral ventricle.

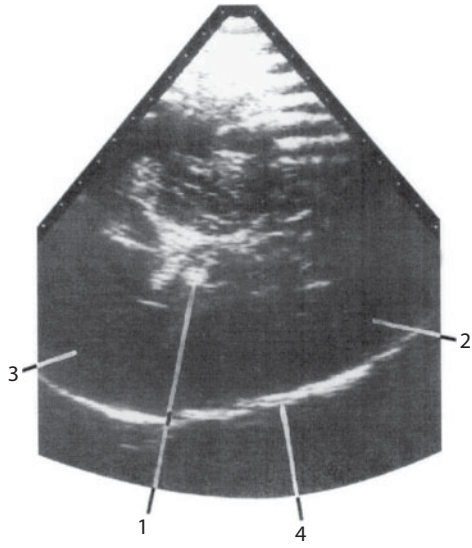

Figure 20 Hematoma at the optic thalamus.

1. Blood clot; 2. Frontal region; 3. Occipital region; 4. Cranium bone from the opposite side.

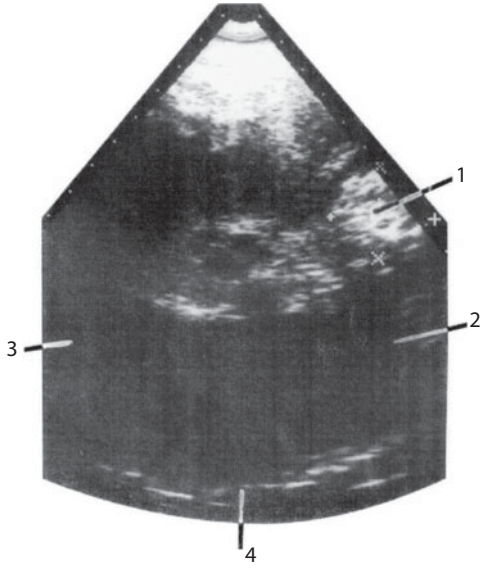

Figure 21 Frontobasal intracerebral hematoma.

1. Blood clot; 2. Frontal region; 3. Occipital region; 4. Cranium bone from the opposite side.

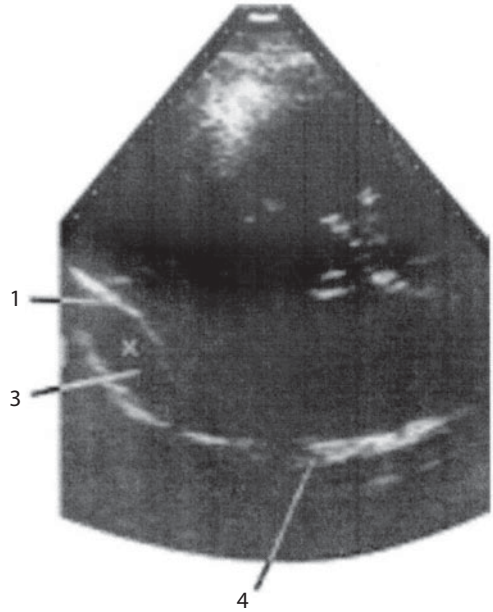

Figure 22 Acute epidural hematoma of the parieto-occipital left region.
1. Phenomenon of the boundary amplification; 3. Hematoma; 4. Cranium bones.

Topography and Pathotopography of the Neck

A wide variety of methods can be used to study the topographical anatomy: layer-by-layer preparation, transverse frozen sections, "ice anatomy", injection method, corrosion method. Intra-organ and extra-organ intravital transillumination, palpation, percussion, auscultation, X-ray, computer tomography, magnetic resonance imaging, and ultrasonic tests are used as intravital methods. Topographical anatomy can be studied on the basis of pictures illustrating the topographical anatomy and providing information about standard locations of organs and adjacent blood vessels, as well as the morphological structure of organs. Cadaver studies provide volume images of organs. However, in this case, the organ and its structure are distorted because of the effect of fixative agents. The topographical anatomy of the organ during functioning remains obscure.

Ultrasonic imaging is based on reflection of ultrasonic waves from the interface of tissues with different acoustic properties. Ultrasonography

is effective for testing the objects containing soft tissues. Such objects contain considerable amounts of fluids and interfaces between tissues with different acoustic properties providing high quality of sonographic imaging. Ultrasonic testing can be used for real-time individual examination of anatomical variability. Thus, ultrasonic tests are very useful for studying the topographical anatomy of the thyroid.

Pictures illustrating the topographical anatomy of the thyroid provide standard images of the thyroid and adjacent anatomical structures: blood vessels (superior thyroid vein, inferior thyroid artery, vein of uncus, common carotid artery, internal jugular vein), muscles (sternohyoid muscle, sternothyroid muscle, subcutaneous neck muscle, sternocleidomastoid muscle), organs (esophagus), and fasciae.

The possibility of ultrasonic imaging of objects depends on the selected cross-section plane. The use of the cross-section of the left lobe provides, in addition to imaging of skin and subcutaneous fat, information about the structure and shape of the lobe, esophagus, common carotid artery, internal jugular vein, and inferior thyroid artery. The superior neck fasciae and undifferentiated muscles of the neck can also be seen. If the sensor is located perpendicular to the median line, the thyroid shape and the thyroid isthmus thickness can be estimated. The use of the longitudinal cross-section of the lobe provides information about the longitudinal dimensions of the parts of the organ. In addition, the ultrasonic tests provide estimation of the topography of blood supply to the thyroid.

The positive feature of the ultrasonic method, as used for the study of topographical anatomy, is the possibility of intravital tests of individual anatomical variability, which allows developmental variants and anomalies of the thyroid to be visualized. This method allows the layer-by-layer topographical anatomy of the neck to be studied. It also provides imaging of the inflammation processes on the walls and parenchyma of organs. It is important to note that this method is non-invasive and low-traumatic.

Ultrasonic topographical anatomy has a considerable practical significance in surgery. Preliminary ultrasonic examination makes it possible to avoid iatrogenic complications. It also provides differential diagnosis of normal and pathological structures in topographical anatomy. The echography contributes to the development and evaluation of new methods of surgical access. Thus, the ultrasonic tests hold much promise for the study of the topographical anatomy of the neck.

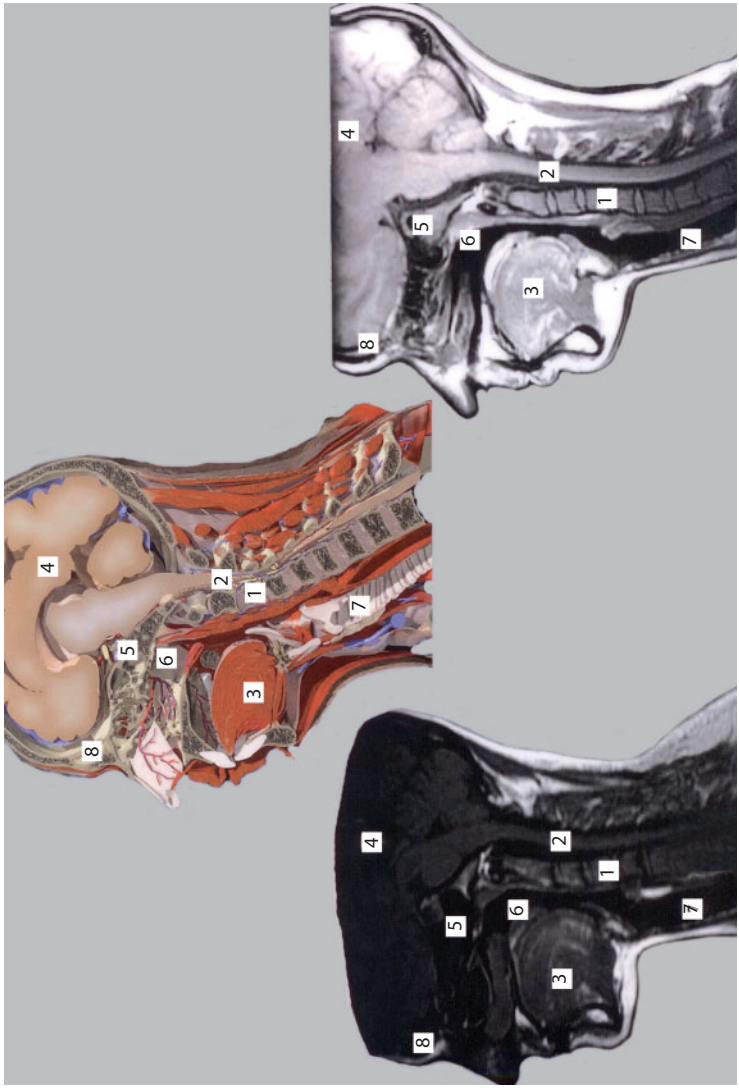

Figure 23 Sagittal slice of the head and the neck.
1. Column; 2. Spinal cord; 3. Tongue; 4. Cerebral hemispheres; 5. Sphenoidal sinus; 6. Nasopharynx; 7. Gorge; 8. Frontal sinus.

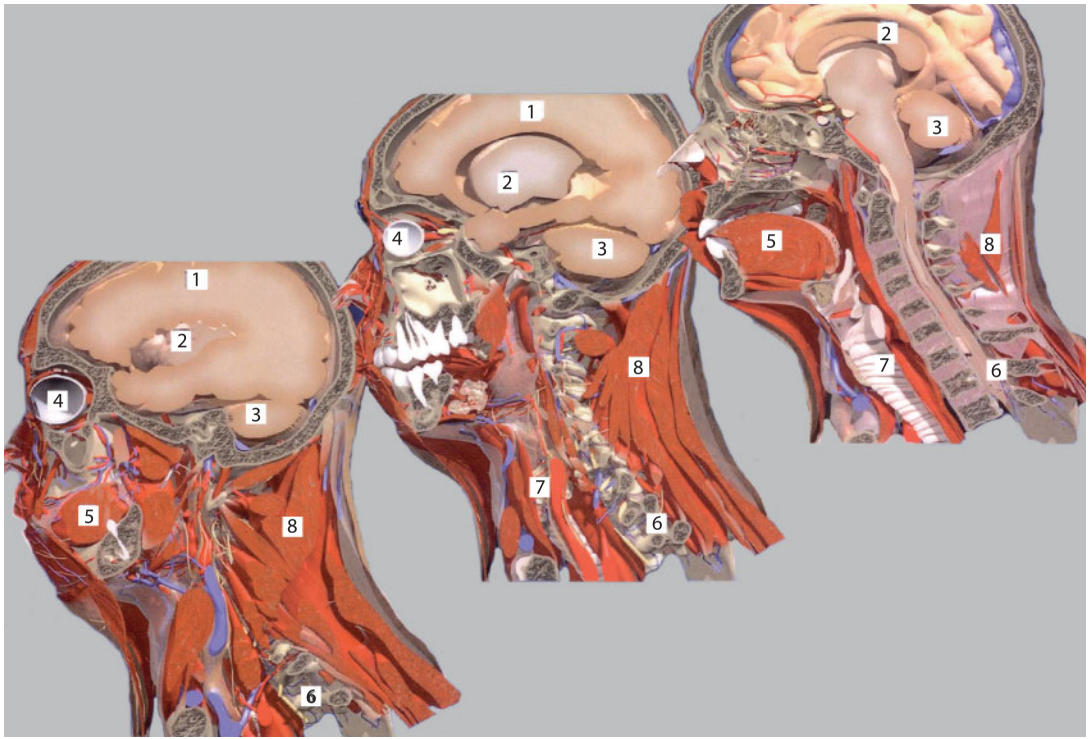

Figure 24 Sagittal slice of the head and the neck.

1. Cerebral hemispheres; 2. Diencephalon; 3. Cerebellum; 4. Eye bulb; 5. Tongue; 6. Column; 7. Trachea; 8. Anterior group of the neck muscles.

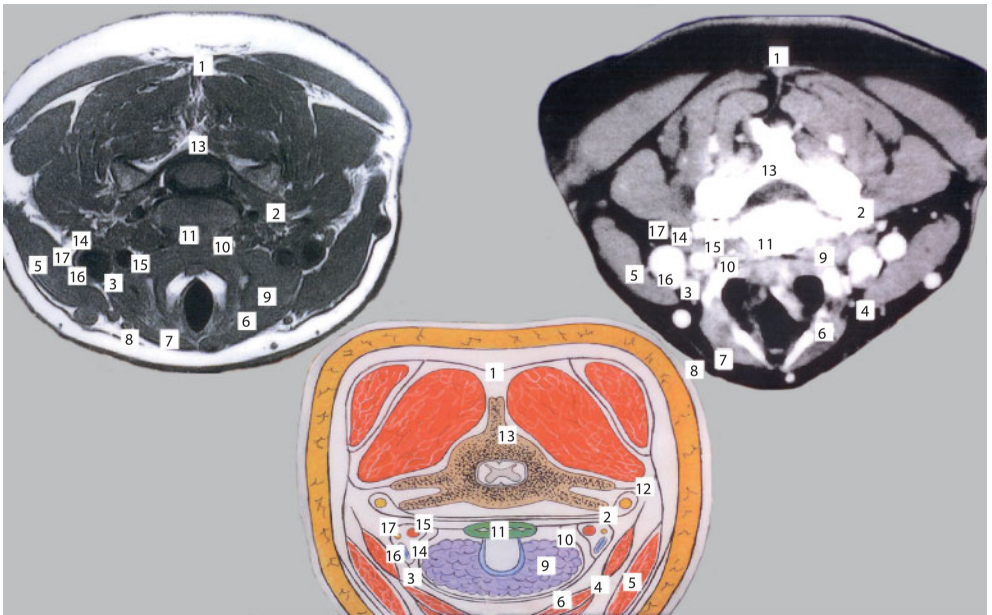

Figure 25 Cross-section of the neck.

1. Second fascia of the neck; 2. Wedge of the second fascia; 3. Parietal layer of the fourth fascia; 4. Third fascia of the neck; 5. Sternocleidomastoid muscle; 6. Sternothyroid muscle; 7. Sternohyoid muscle; 8. First fascia of the neck; 9. Thyroid; 10. Visceral layer of the fourth fascia; 11. Esophagus; 12. Prevertebral fascia; 13. Cervical vertebra; 14. Neurovascular bundle; 15. Common carotid artery; 16. Internal jugular vein; 17. Nervus vagus.

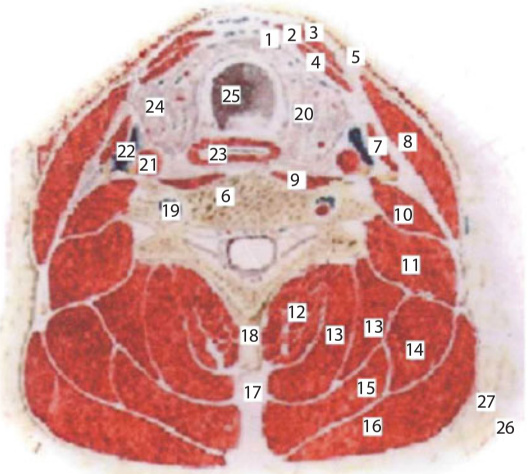

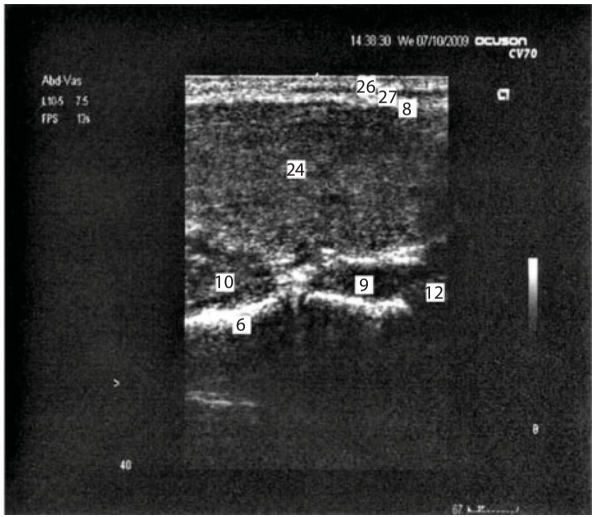

Figure 26 Muscles and fasciae of the neck.

1. Pretracheal layer of cervical fascia (medium fascia of the neck); 2. Sternohyoid muscle; 3. Lamina superficialis fasciae cervicalis (superficial fascia of the neck); 4. Sternothyroid muscle; 5. Subcutaneous neck muscle; 6. Fifth cervical vertebra; 7. Scapular supraglossal muscle; 8. Sternocleidomastoid muscle; 9. Long muscle of the neck; 10. Superior scalene muscle; 11. Medium and posterior scalene muscles; 12. Semispinal muscle of the neck; 13. Semispinalis capitis muscle; 14. Levator scapulae muscle; 15. Splenius muscles of the head and neck; 16. Trapezius muscle; 17. Nuchal ligament; 18. Spinous process of cervical vertebra; 19. Vertebral artery and vein; 20. Left lobe of the thyroid; 21. Common carotid artery; 22. Internal jugular vein; 23. Esophagus; 24. Right lobe of the thyroid; 25. Trachea; 26. Skin; 27. Subcutaneous fat.

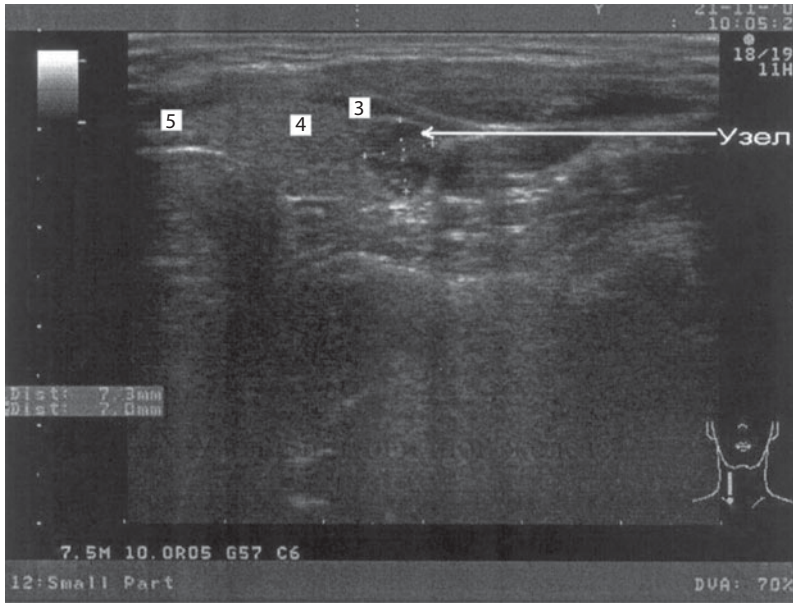

Figure 27 Thyroid node.

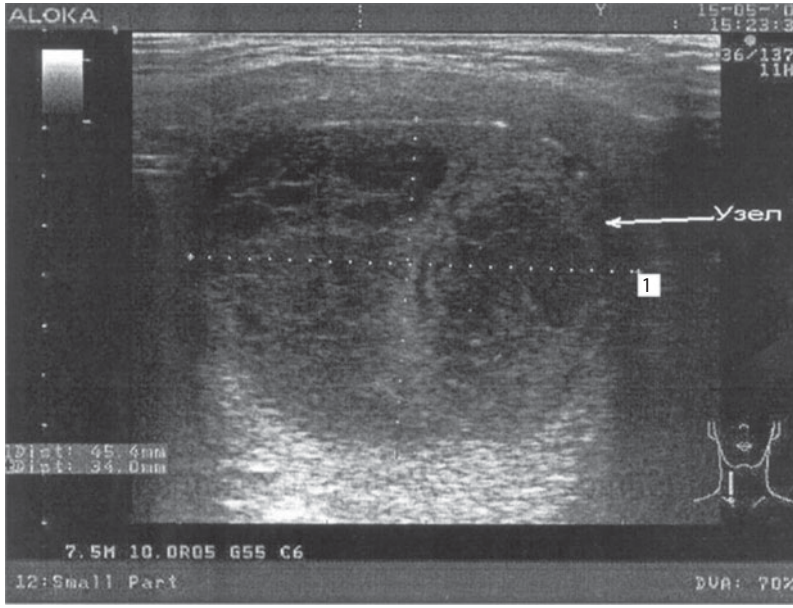

Figure 28 Thyroid node (magnified).

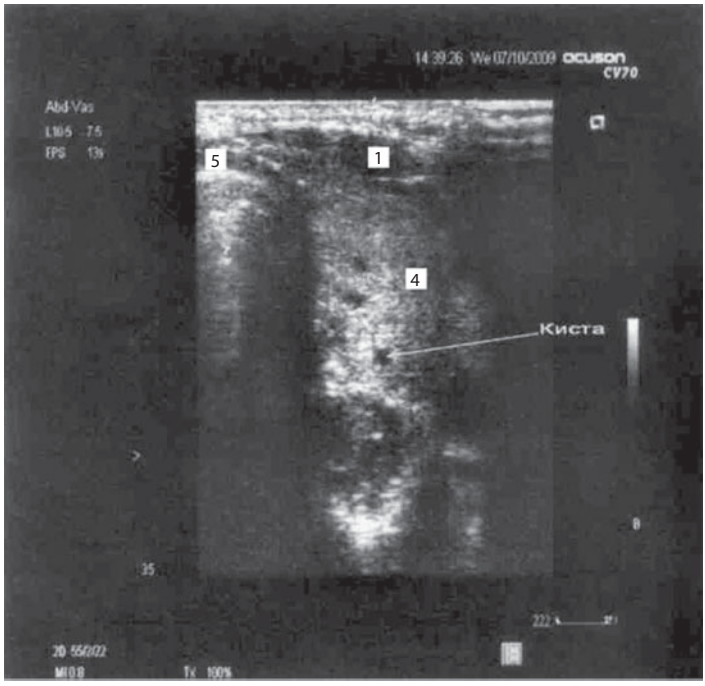

Figure 29 Thyroid left lobe cysts.

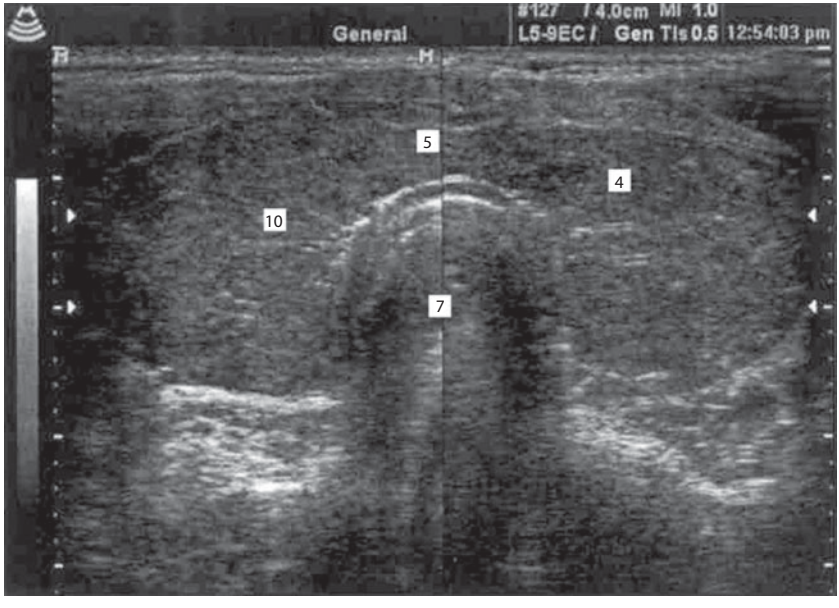

Figure 30 Chronic thyroiditis.

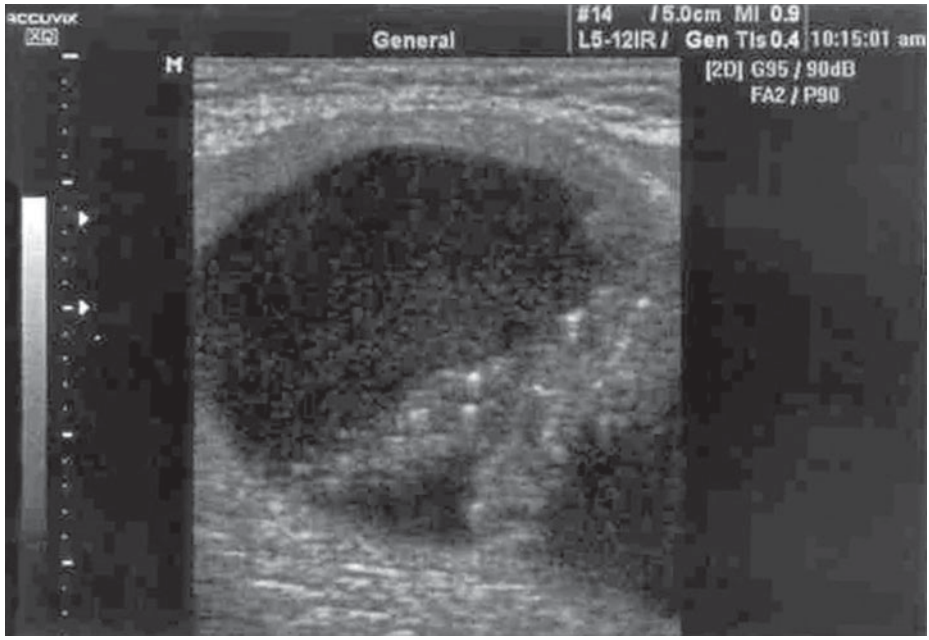

Figure 31 Thyroid hemorrhagic cyst (magnified).

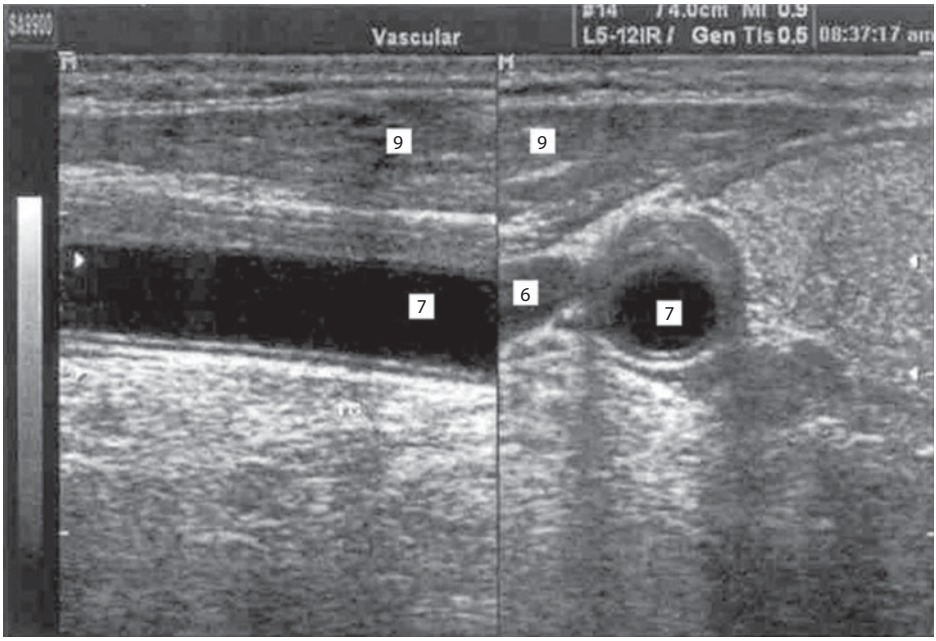

Figure 32 Common carotid artery sternosis.

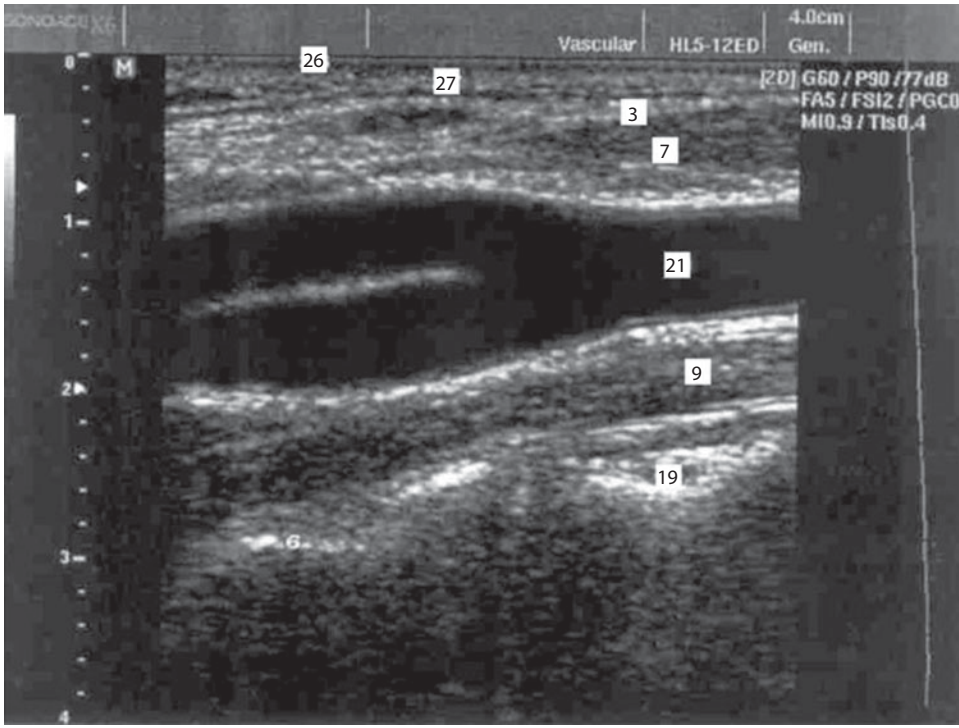

Figure 33 Topography of carotid and vertebral arteries. Muscles and fasciae of the neck.

1. Pretracheal layer of cervical fascia (medium fascia of the neck); 2. Sternohyoid muscle; 3. Lamina superficialis fasciae cervicalis (superficial fascia of the neck); 4. Sternothyroid muscle; 5. Subcutaneous neck muscle; 6. Fifth cervical vertebra; 7. Scapular supraglossal muscle; 8. Sternocleidomastoid muscle; 9. Long muscle of neck; 10. Superior scalene muscle; 11. Medium and posterior scalene muscles; 12. Semispinal muscle of the neck; 13. Semispinalis capitis muscle; 14. Levator scapulae muscle; 15. Splenius muscle of the head and neck; 16. Trapezius muscle; 17. Nuchal ligament; 18. Spinous process of cervical vertebra; 19. Vertebral artery and vein; 20. Left lobe of the thyroid; 21. Common carotid artery; 22. Internal jugular vein; 23. Esophagus; 24. Right lobe of the thyroid; 25. Trachea; 26. Skin; 27. Subcutaneous fat.

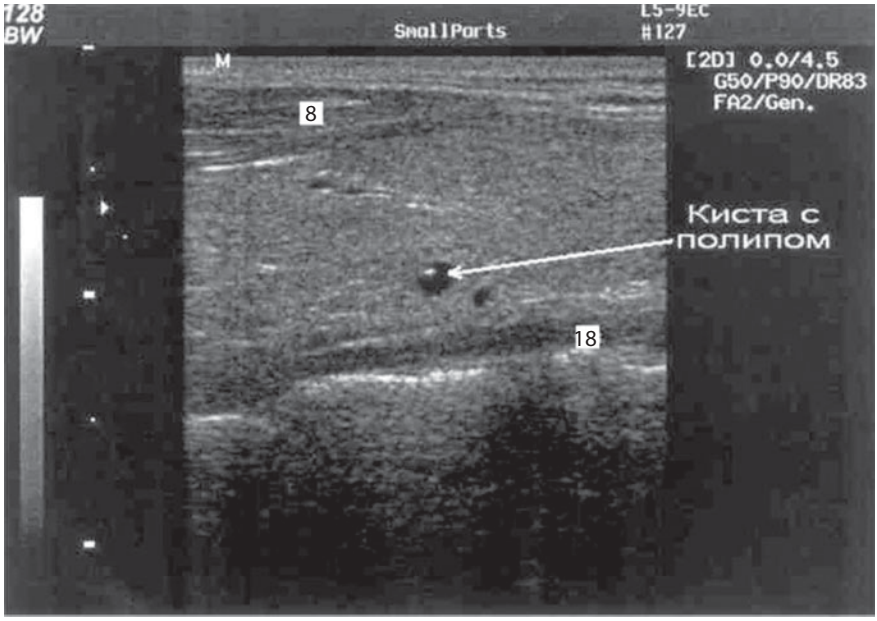

Figure 34 Cyst with polyp.

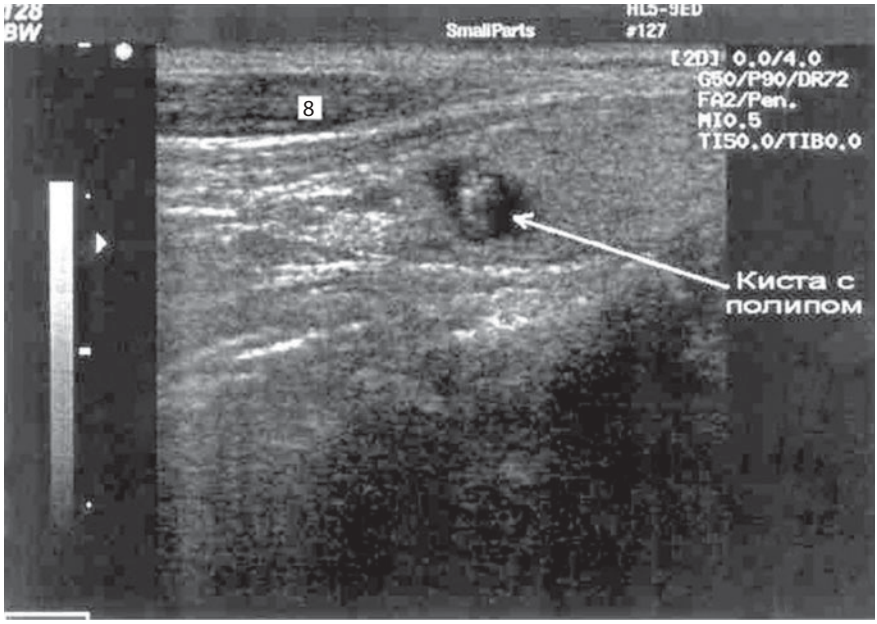

Figure 35 Cyst with polyp (magnified).

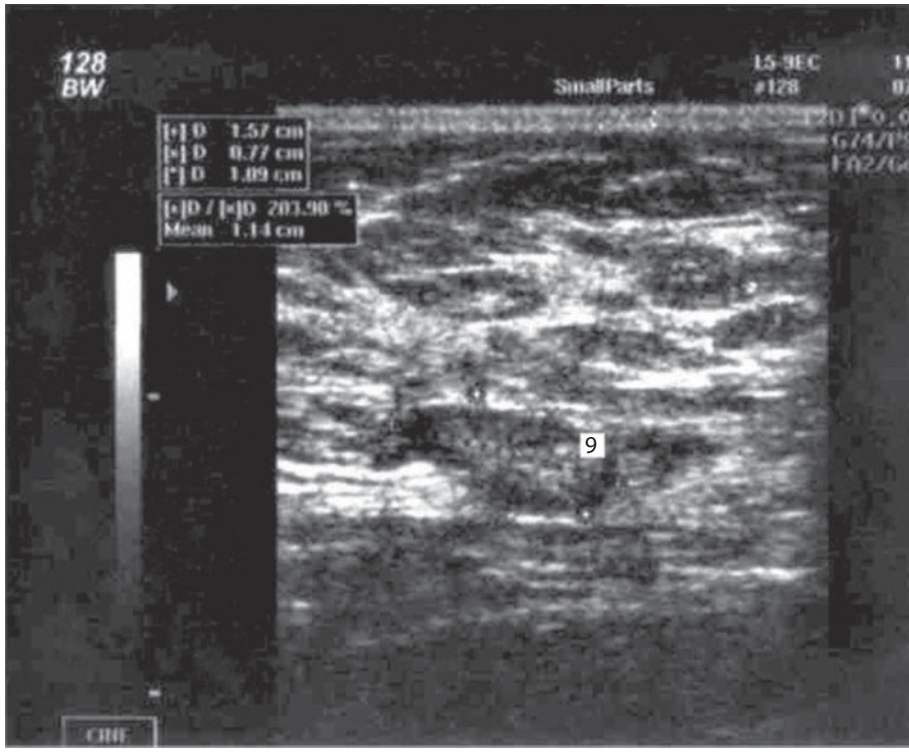

Figure 36 Submaxillary lymphatic node.

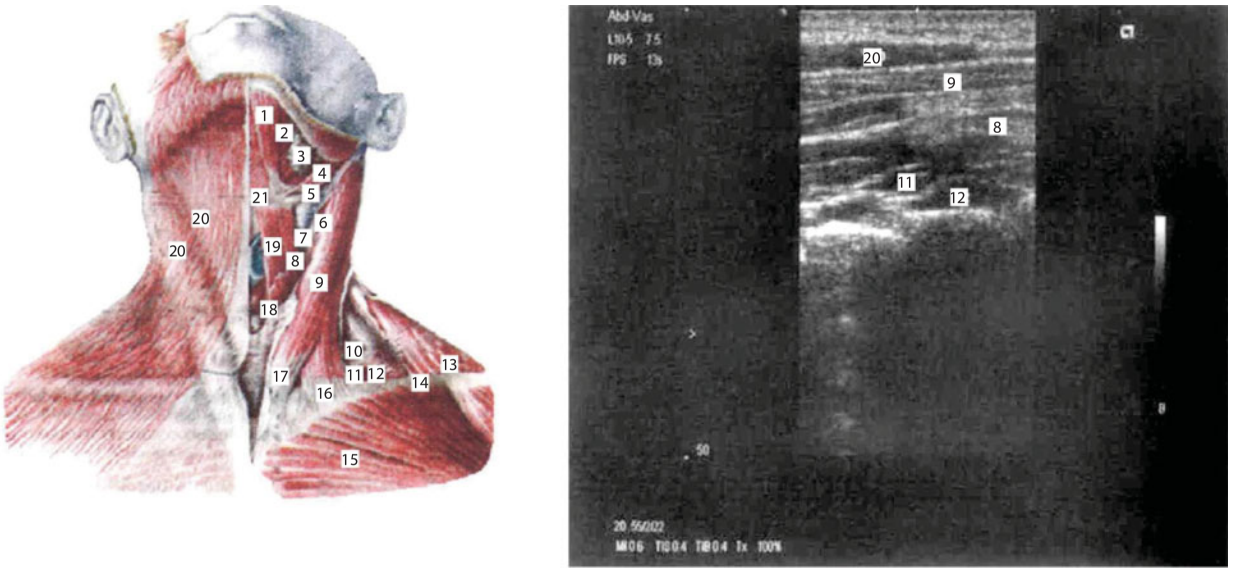

Figure 37 Interfacial muscles of the neck.

1. Anterior belly of the digastric muscle; 2. Mylohyoid muscle; 3. Submaxillary salivary gland; 4. Stylo-subglossal muscle; 5. Posterior belly of the digastric muscle; 6. Internal jugular vein; 7. Common carotid artery; 8. Superior belly of the omohyoid muscle; 9. Sternocleidomastoid muscle; 10. Inferior belly of the omohyoid muscle; 11. Middle scalene muscle; 12. Posterior scalene muscle; 13. Trapezius muscle; 14. Clavicula; 15. Greater pectoral muscle; 16. Clavicular portion of the sternocleidomastoid muscle; 18. Sternothyroid muscle; 19. Sternohyoid muscle; 20. Subcutaneous neck muscle; 21. Hyoid.

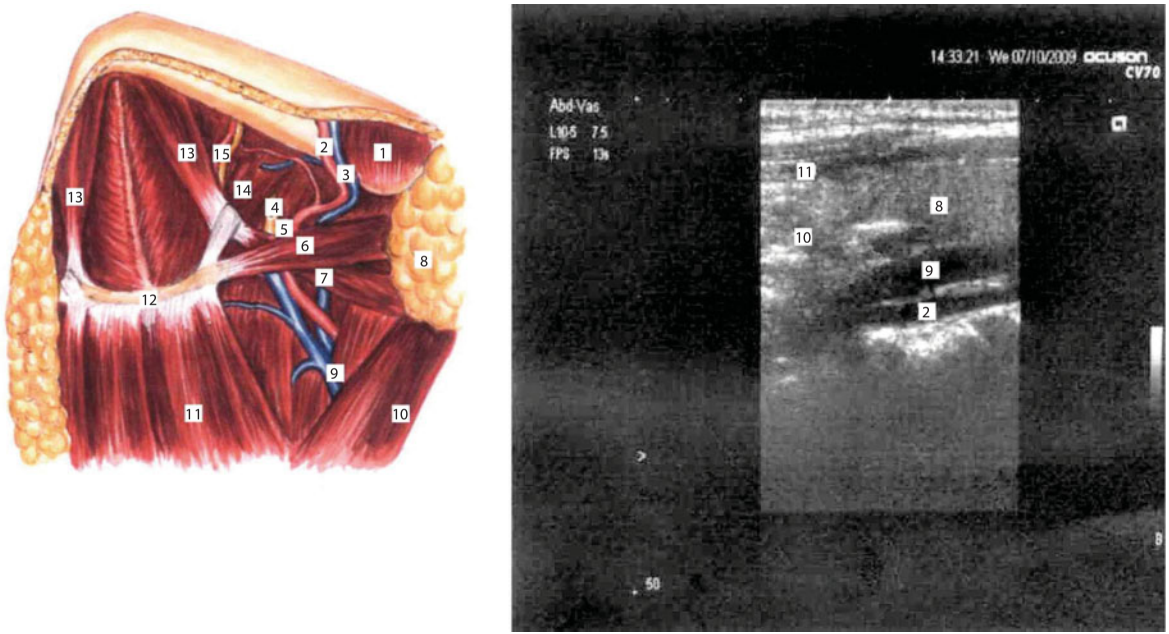

Figure 38 Deep layers of the suprahyoid area.

1. Muscles of mastication; 2. Facial artery; 3. Facial vein; 4. Hypoglossal nerve; 5. Hyoglossal muscle; 6. Stylohyoid muscle; 7. Posterior belly of the digastric muscle; 8. Parotid gland; 9. Common facial vein; 10. Sternocleidomastoid muscle; 11. Long muscle of the larynx; 12. Hyoid; 13. Anterior belly of the digastric muscle; 14. Mylohyoid muscle; 15. Submental artery and mylohyoid nerve.

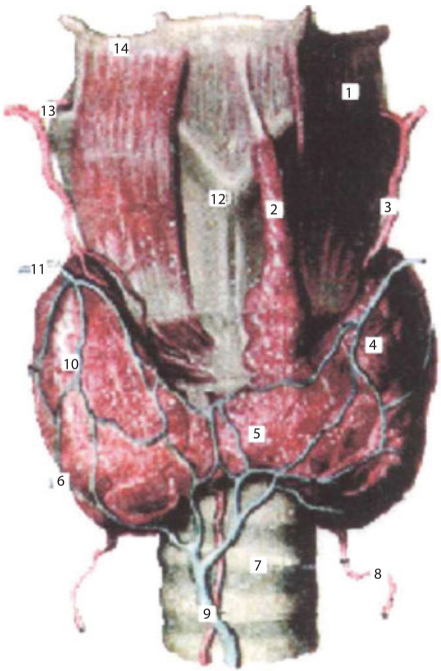

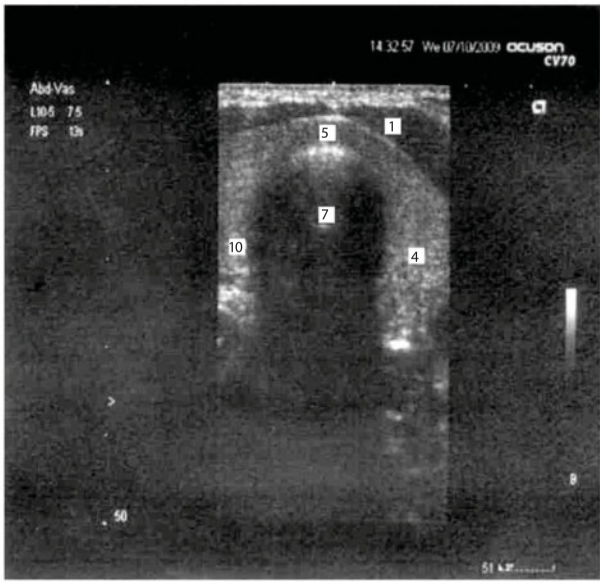

Figure 39 Thyroid.

1. Thyrohyoid muscle; 2. Pyramidal lobe of thyroid; 3. Superior thyroid artery; 4. Left lobe of thyroid; 5. Isthmus of thyroid; 6. Inferior thyroid vein; 7. Trachea; 8. Inferior thyroid artery; 9. Azygous thyroid vein; 10. Right lobe of thyroid; 11. Superior vein of thyroid; 12. Cartilago thyroidea; 13. Superior laryngeal artery; 14. Hyoid bone.

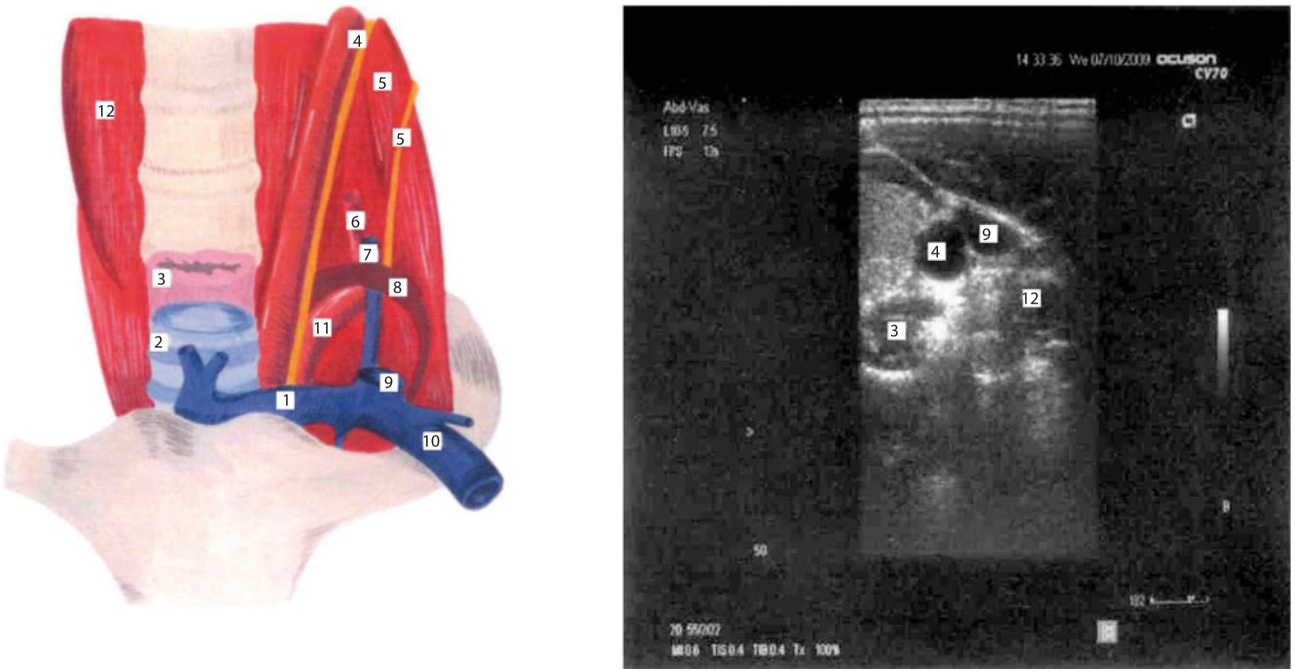

Figure 40 Topography of the scalenovertebral triangle.

1. Left brachiocephalic vein; 2. Trachea; 3. Esophagus; 4. Common carotid artery and vagus nerve; 5. Phrenic nerve and anterior scalene muscle; 6. Vertebral artery; 7. Vertebral vein; 8. Thoracic duct flow; 9. Internal jugular vein; 10. Left subclavian vein; 11. Left subclavian artery; 12. Longi capitis and long muscles of the neck.

Topographical and Pathotopographical Anatomy of the Chest

The chapter on the ultrasonic topography and pathotopographic anatomy of the chest includes the layer-by-layer topography of surface structures (skin, subcutaneous fat, surface and deep muscles of the chest, ribs, ligaments), surface organs (mammary glands, lymph nodes), and deeply situated organs (heart, vessels, including ascending and descending aorta, aortic arch, lungs, and pleura).

Ultrasonic images of the skin, subcutaneous fat, surface and deep muscles, vessels of subcutaneous layer, and thoracic aorta are presented. Images of the base, apex, and chambers of the heart have been verified based on comparison with the topographic anatomy data.

Echocardiography (EchoCG) is the method of cardiac research based on the use of reflected ultrasonic waves.

The history of EchoCG dates back more than 40 years to the works of I. Edler and C. Hertz, who for the first time used ultrasonic pulse reflection in cardiac studies.

Modern echocardiography is a complex method providing a broad range of diagnostic procedures. Modern cardiographic techniques use 2-D, 1-D, and Doppler EchoCG, which allow volume of the heart chambers to be measured, morphology and functions of both natural and artificial valves to be studied, the contractile activity of the myocardium to be estimated, and the location and volume of intracardiac shunts and the presence of intracardiac structures to be determined.

2-D EchoCG (B-mode) is the method for obtaining 2-D images of the heart (cross-sections) with respect to the long and short axes in real-time mode. 2-D EchoCG provides:

- assessment of the size and volume of the heart chambers, thickness of the heart walls, weight of the left ventricular myocardium;
- assessment of global and local ventricular contractility;
- calculation of the liquid volume in pericardium;
- detection of developmental anomalies and acquired pathologies of the valve apparatus and subvalvular structures;
- detection of atrial and ventricular septal defects, their number and location;
- detection of outlet anomalies of the heart;
- detection of cardiac tumors and intracardiac blood clots.

Introduction of EchoCG in clinical practice increased the quality of diagnosis of congenital and acquired heart diseases. EchoCG became indispensable for cardiac surgery because of its high information content and simple use, which made it possible to avoid more sophisticated invasive diagnosis.

1-D EchoCG (M-mode) is a technique for the imaging of heart wall and valve motion in time. 1-D EchoCG provides information about

mobility of heart structures intercepted by a single ultrasonic beam. Presently, 1-D EchoCG is used as an accessory mode of echocardiography, primarily for measurements.

The problem of correlation of the thyroid and mammary gland pathologies is of interest to endocrinologists, reproductive endocrinologists, and mammologists, as well as ultrasound diagnosticians.

It is well known that the pituitary-thyroid system and pituitary-gonadal system are controlled by the hypothalamus, which determines to a large extent the functional correlation between the systems. The neurons of the mediobasal region of the hypothalamus synthesize a gonadotropin-releasing hormone and release it into the hypophyseal portal system. The neurons of the preoptic region of the hypothalamus synthesize a thyrotropin-releasing hormone. In pituitary gland cells, the thyrotropin secretion is stimulated by a thyrotropin-releasing hormone. Dysfunction of the pituitary-thyroid system can modify secretion not only of gonadotropin, but of prolactin as well. Therefore, the hypothalamic thyrotropin-releasing hormone potentially stimulates the release not only of thyrotropin, but also of prolactin. Increase in T3 and T4 above the normal level inhibits prolactin, while the decrease of T3 and T4 in blood plasma enhances the prolactin release stimulated by the thyrotropin-releasing hormone, thereby leading to hyperprolactinemia.

Presently, breast ultrasound is the most available diagnostic procedure. It is noninvasive and inexpensive, has no contraindications, provides valuable diagnostic information, and exhibits no pharmacologic or radiation load on the human body.

The diagnostic importance of ultrasound has considerably increased due to improvements in high-frequency sensors and introduction of digital technologies.

Color Doppler Imaging (CDI) and Power Doppler Imaging (PDI) allow the hemodynamics to be diagnosed in cases both of normal results of breast ultrasound, and of diffuse changes and the presence of pathological foci.

Complex ultrasonic research was implemented using standard scanning modes:

- gray-scale (B-mode);
- color Doppler mapping of blood flow energy and rate;
- spectral Doppler imaging.

In some cases, 3-D reconstruction was used to provide better spatial presentation of anatomical interaction between the structures.

The presence of any of the symptoms listed below was considered as an indication for examination: palpated neoplasms in thyroid or mammary gland; any clinical form of mastopathy; any clinical form of thyroid dysfunction; plugged duct or mastitis in anamnesis; mammary gland injury; changes observed in mammogram; severe family medical history concerning mammary gland and thyroid.

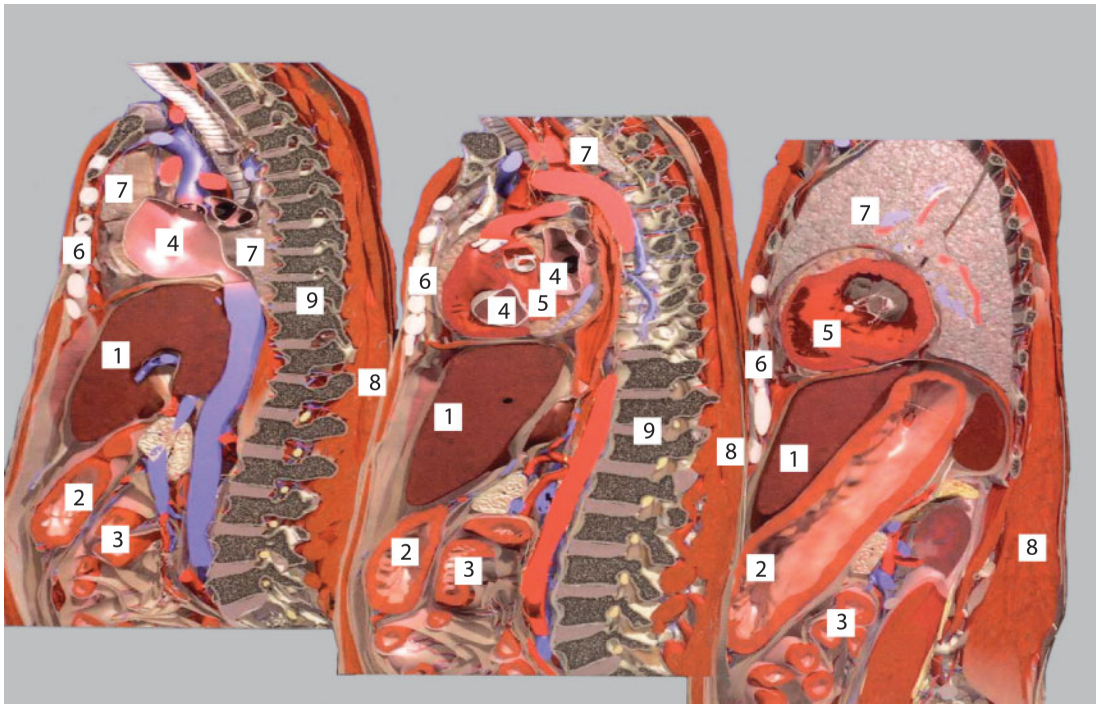

Figure 41 Sagittal section of the chest and abdomen.

1. Liver; 2. Large intestine; 3. Small intestine loops; 4. Right atrium; 5. Left ventricle; 6. Breast bone; 7. Lung; 8. Long muscles of the back; 9. Spinal column.

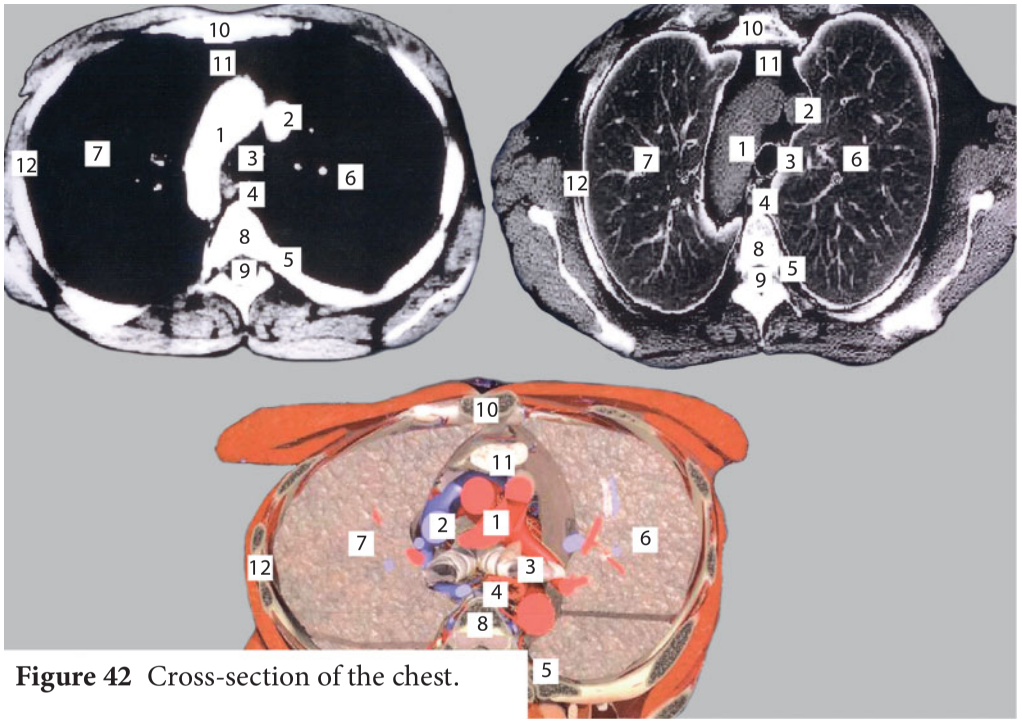

Figure 42 Cross-section of the chest.

1. Arch of aorta; 2. Superior vena cava; 3. Trachea; 4. Esophagus; 5. Sympathetic trunk; 6. Right lung; 7. Left lung;
8. Vertebra; 9. Spinal cord; 10. Breast bone; 11. Mediastinal cellular tissue; 12. Pleura.

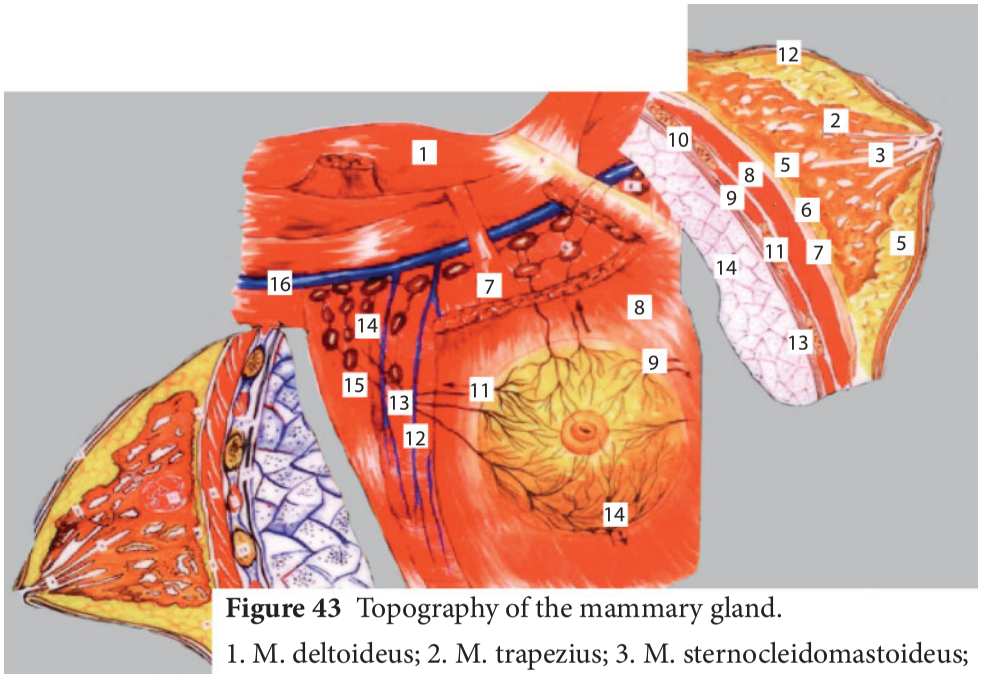

Figure 43 Topography of the mammary gland.

1. M. deltoideus; 2. M. trapezius; 3. M. sternocleidomastoideus; 4. N. lymphatici supraclaviculares; 5. Clavicula; 6. N. lymphatici subclaviculares; 7. M. pectoralis minor; 8. M. pectoralis major; 9. Tracti lymphatici ut nodi lumphatici sternalis; 10. Tracti lumphatici ut noda lymphatici epigastrici et subphrenici; 11. Tracti lymphatici ut nodi lymphatici axillares; 12. V. thoracica externa; 13. N. l. paramammaria; 14. N. lymphatici axillares; 15. M. latissimus dorsi; 16. V. axillaris.

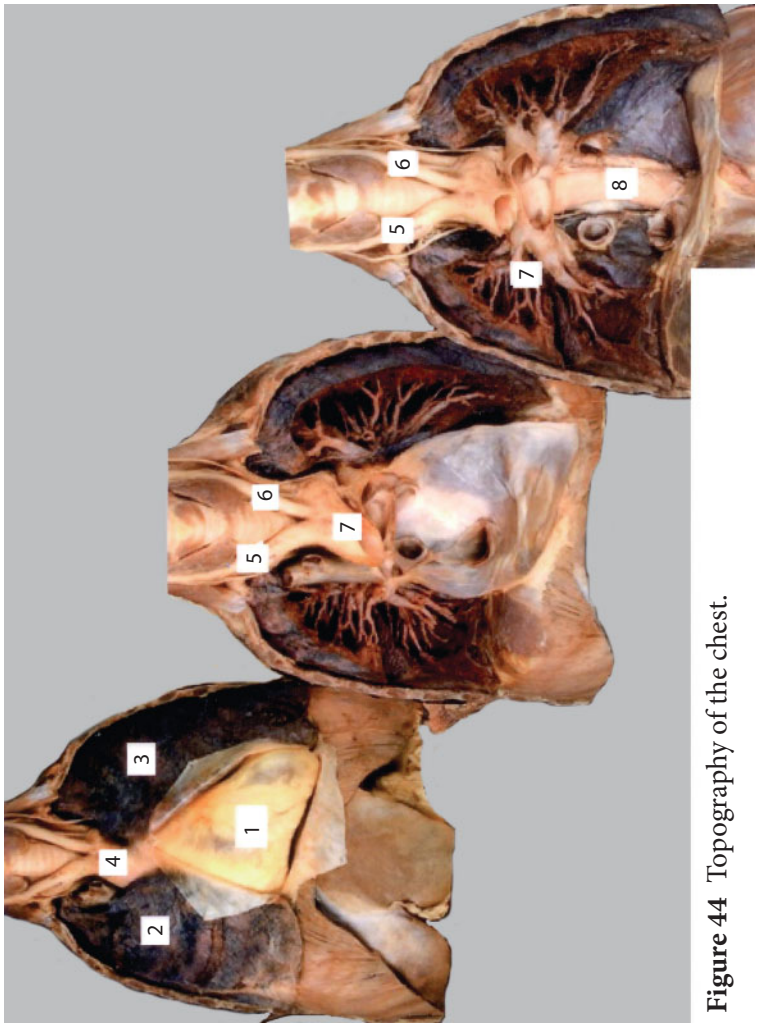

Figure 44 Topography of the chest.

1. Cor; 2. Pulmo dextrum; 3. Pulmo sinistrum; 4. Arcus aortae; 5. a. carotis communis dextra; 6. a. carotis communis sinistra; 7. Bronchi; 8. Aorta thoracica.

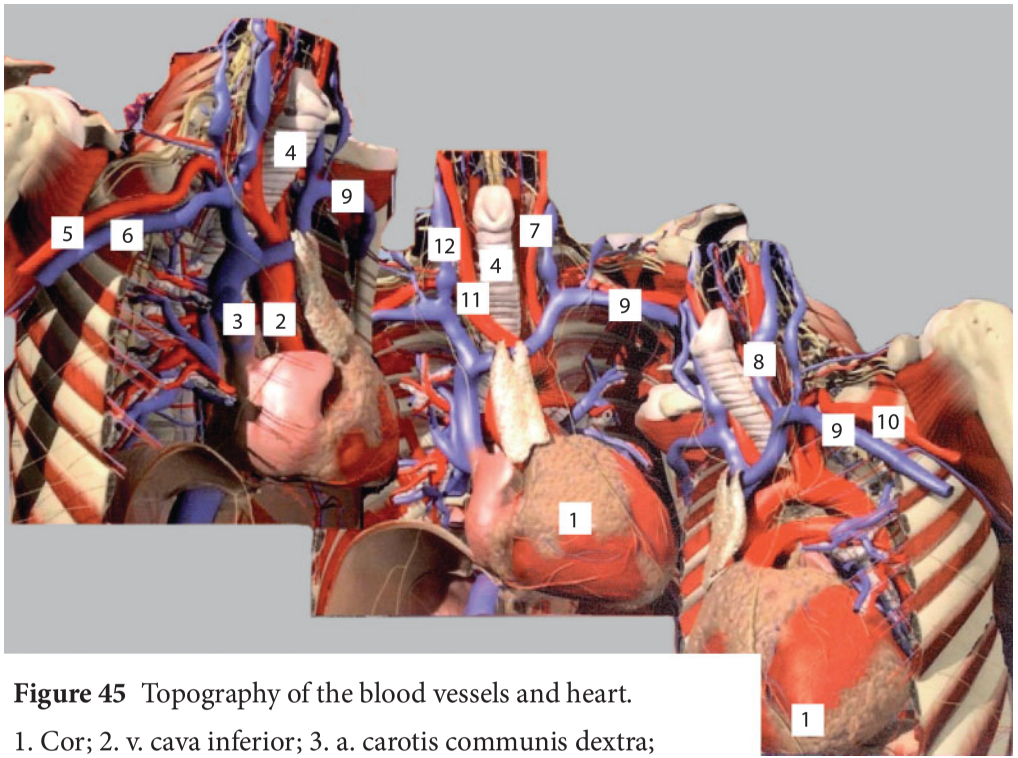

Figure 45 Topography of the blood vessels and heart.

1. Cor; 2. v. cava inferior; 3. a. carotis communis dextra;
4. Trachea; 5. v. jugularis interna; 6. v. subclavia sinistra; 7. a. subclavia sinistra;
8. a. carotis communis sinistra; 9. aa. et vv. intercostales.

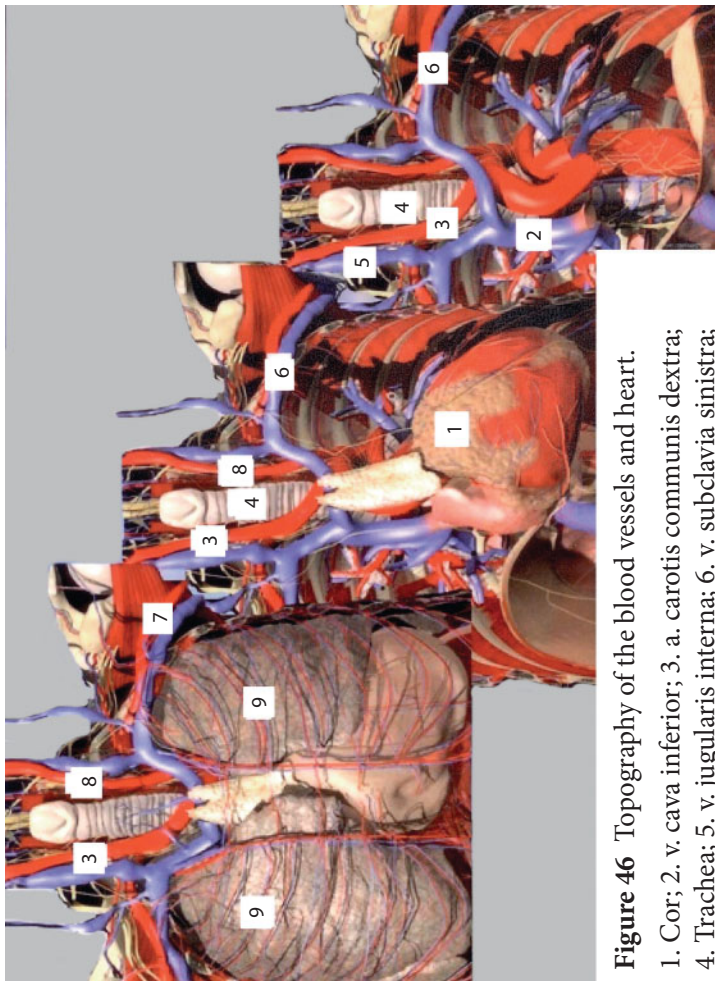

Figure 46 Topography of the blood vessels and heart.
1. Cor; 2. v. cava inferior; 3. a. carotis communis dextra; 4. Trachea; 5. v. jugularis interna; 6. v. subclavia sinistra; 7. a. subclavia sinistra; 8. a. carotis communis sinistra; 9. aa. et vv. intercostales.

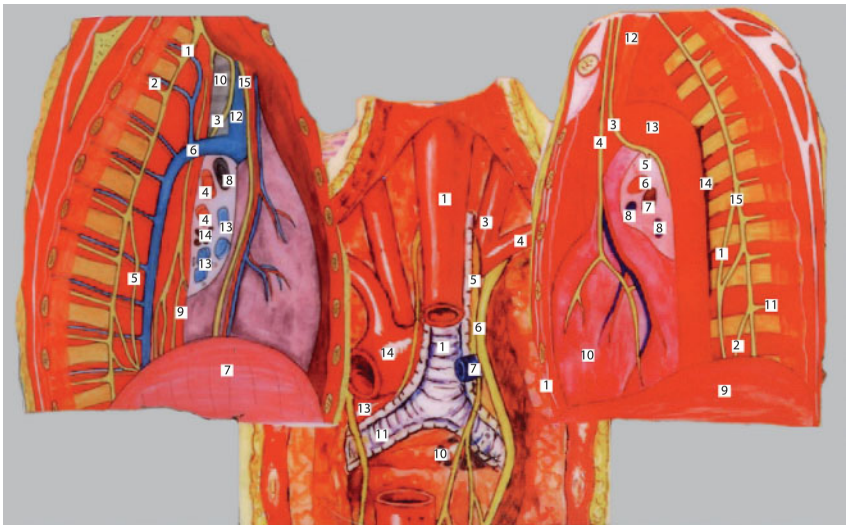

Figure 47 Topography of the lung roots.

1. Truncus sympathcus; 2. aa. et nervi intercostales; 3. n. vagus; 4. a. pulmonalis; 5. n. splanchnicus major; 6. v. azygos; 7. Diaphragm; 8. Bronchi dexter; 9. Easophageus; 10. Trachea; 11. n. phrenicus; 12. vena cava superior; 13. vv. pulmonales; 14. Nodus lymphaticus.

1. n. splanchnicus major; 2. n. splanchnicus minor; 3. n. vagus; 4. n. phrenicus; 5. n. recurrens; 6. a. pulmonales; 7. Bronchi sinister; 8. vv. pulmonales; 9. Diaphragm; 10. Pericardium; 11. r. sympathies n. intercostales; 12. a. subclavia; 13. Arcus aortae; 14. v. hemiazygos; 15. Truncus sympathicus.

1. Easophageus; 2. Trachea; 3. a. carotis communis; 4. a. subclavia; 5. n. recurrens; 6. n. vagus; 7. v. hemiazygos; 8. Pulmo sinister; 9. Bronchi dexter; 10. Nodi lymphatici tracheobronchiales; 11. Bronchi sinister; 12. Pulmo dexter; 13. a. pulmonales sinister; 14. Arcus aortae.

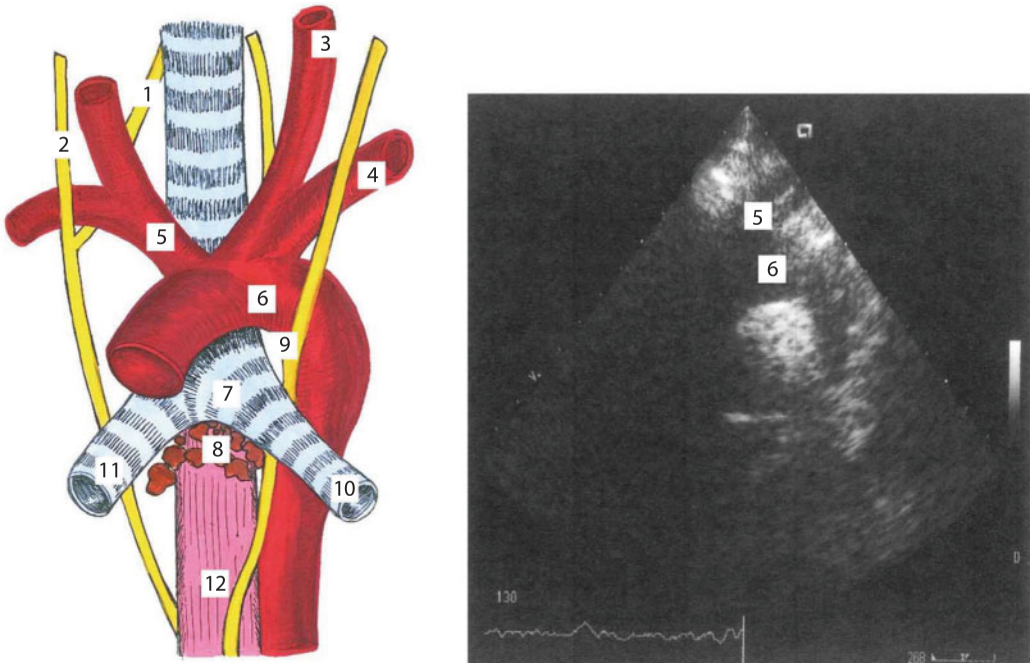

Figure 48 Topography of the bifurcation of the trachea and the aorta.

1. Right recurrent nerve; 2. Vagus nerve; 3. Common carotid artery; 4. Clavicular artery; 5. Brachiocephalic trunk; 6. Arch of aorta; 7. Tracheal bifurcation; 8. Tracheobronchial lymph nodes; 9. Left recurrent nerve; 10. Left bronchus; 11. Right bronchus; 12. Esophagus.

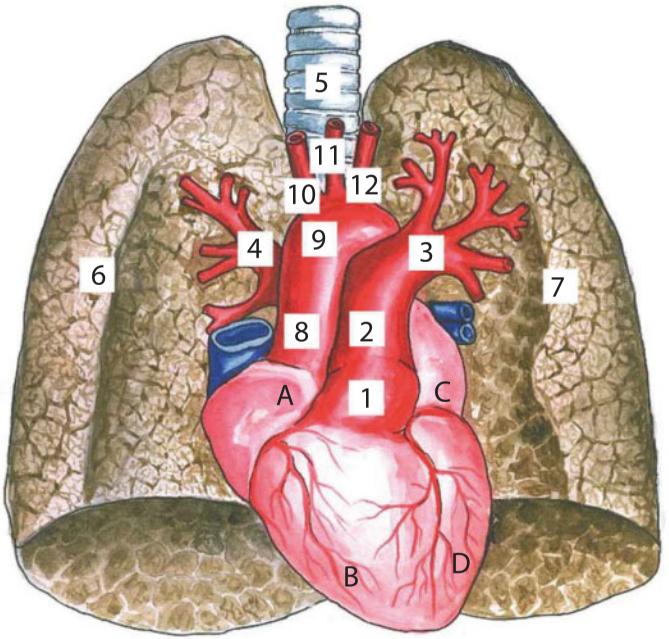

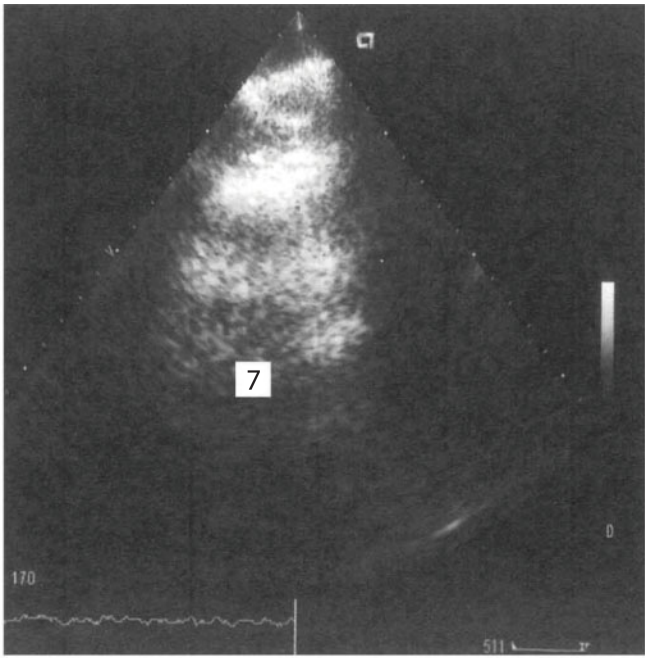

Figure 49 Topography of the heart and the lungs.

1. Arterial cone; 2. Pulmonary trunk; 3. Left pulmonary artery; 4. Right pulmonary artery; 5. Trachea; 6. Right lung; 7. Left lung; 8. Ascending aorta; 9. Arch of aorta; 10. Brachiocephalic trunk; 11. Common carotid artery; 12. Clavicular artery; 13. Right atrium; 14. Right ventricle; 15. Left atrium; 16. Left ventricle.

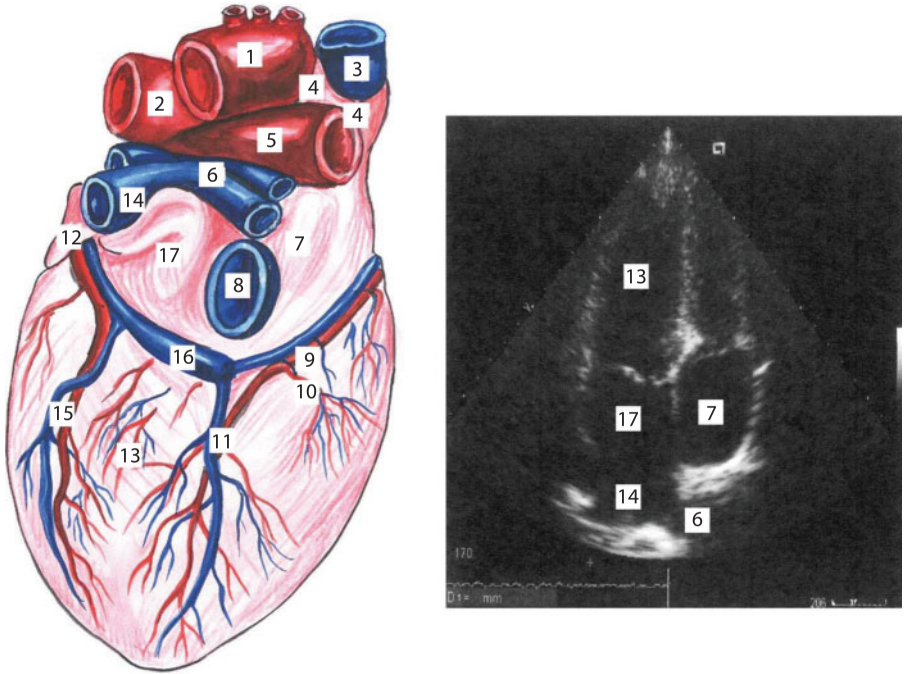

Figure 50 Topography of the heart.

1. Arch of aorta; 2. Left pulmonary artery; 3. Superior vena cava; 4. Transition line of the pericardium; 5. Right pulmonary artery; 6. Right pulmonary veins; 7. Right atrium; 8. Inferior vena cava; 9. Right coronary artery; 10. Blood vessels of the right ventricle; 11. Middle cardiac vein and right descending coronary artery; 12. Left auricle; 13. Left ventricle; 14. Left pulmonary veins; 15. Blood vessels of the left ventricle; 16. Coronary sinus; 17. Left atrium.

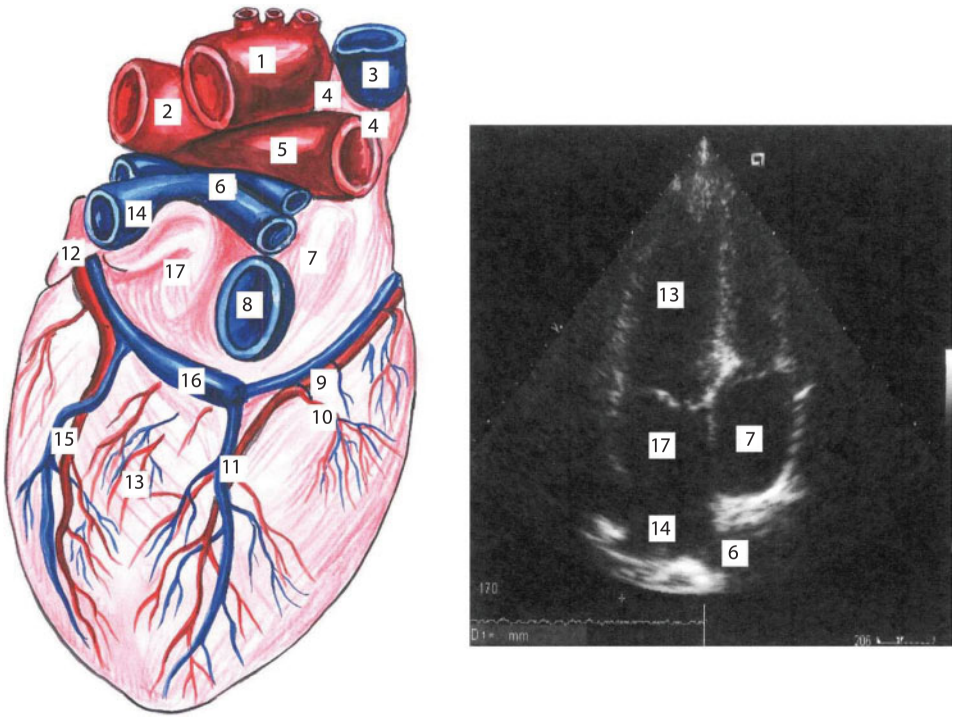

Figure 51 Topography of the heart and blood.

1. Arch of aorta; 2. Left pulmonary artery; 3. Superior vena cava; 4. Transition line of the pericardium; 5. Right pulmonary artery; 6. Right pulmonary veins; 7. Right atrium; 8. Inferior vena cava; 9. Right coronary artery; 10. Blood vessels of the right ventricle; 11. Middle cardiac vein and right descending coronary artery; 12. Left auricle; 13. Left ventricle; 14. Left pulmonary veins; 15. Blood vessels of the left ventricle; 16. Coronary sinus; 17. Left atrium.

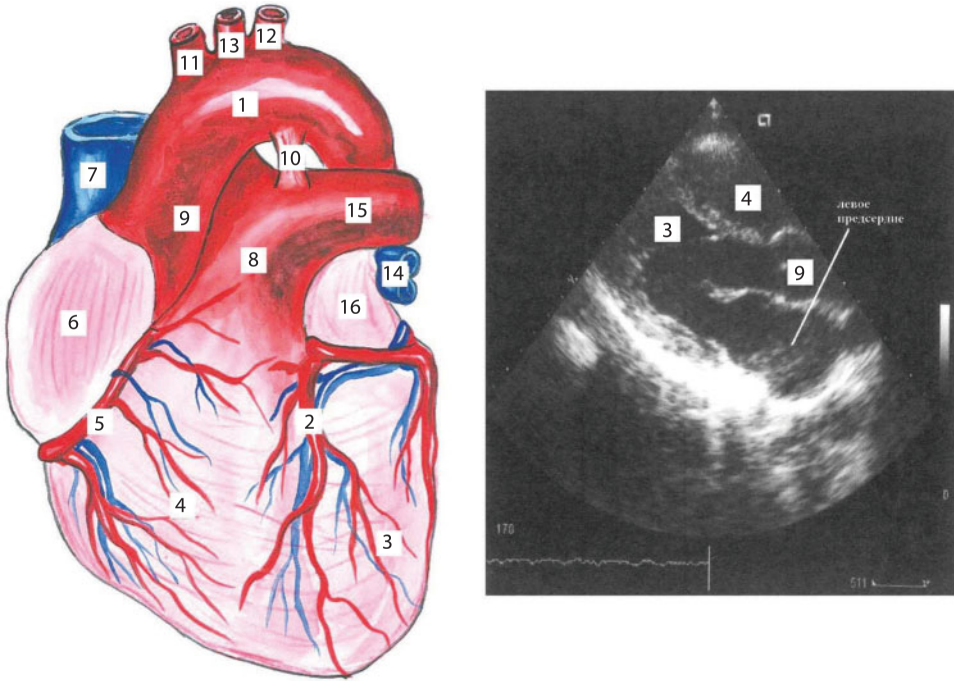

Figure 52 Topography of the heart and blood vessels.

1. Arch of aorta; 2. Left coronary artery; 3. Left ventricle; 4. Right ventricle; 5. Right coronary artery; 6. Right auricle; 7. Superior vena cava; 8. Pulmonary trunk; 9. Ascending part of aorta; 10. Arterial ligament; 11. Brachiocephalic trunk; 12. Left clavicular artery; 13. Left common carotid artery; 14. Left pulmonary veins; 15. Left branch of the pulmonary trunk; 16. Left auricle.

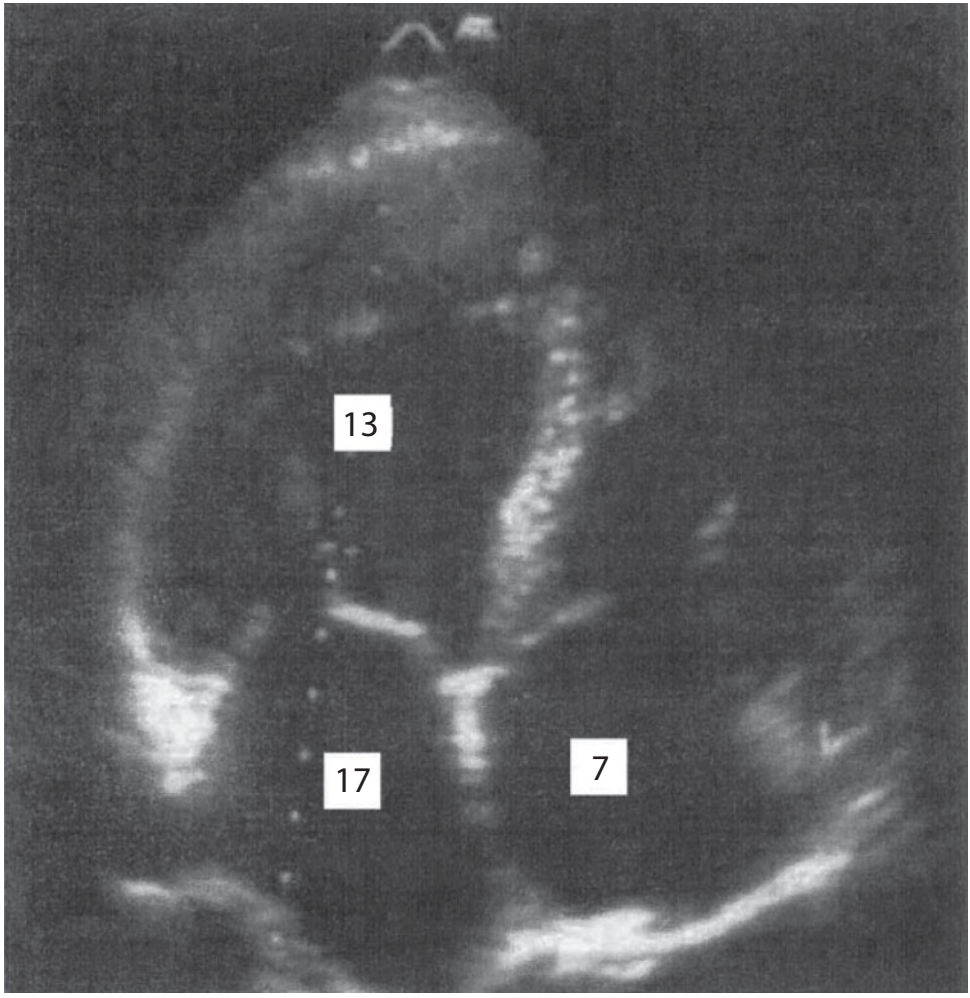

Figure 53 Dilatation of the cardiac chambers.

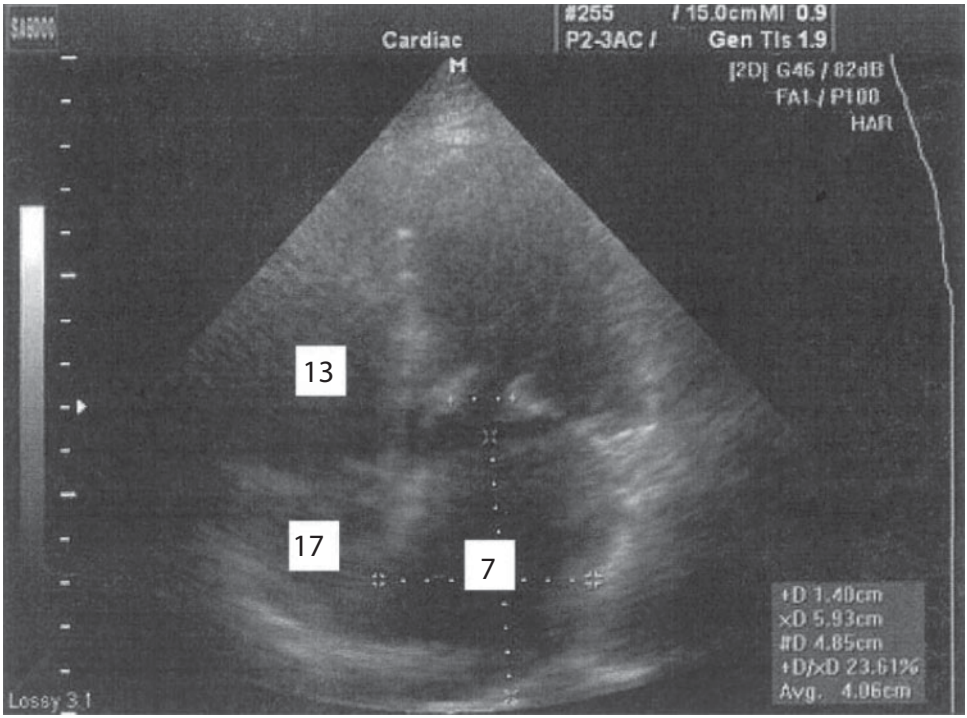

Figure 54 Mitral stenosis.

Topographical and Pathotopographical Anatomy of the Abdomen

Ultrasonic topographical anatomy of the abdomen still faces a few problems. These include the layer-by-layer topography of the anterolateral abdominal wall, syntopy of the abdominal cavity organs, vascular system, lines of attachment of mesostenium and mesocolon, etc. Comparative topography of different anatomical structures is presented in the atlas; such organs as liver, gallbladder, and spleen are described.

The pathotopography of the liver is represented by hepatic hemangioma, concrements, hepatic cysts, and tumors of the right and left hepatic lobes. Gallbladder pathology is represented by acute cholecystitis, cholelithiasis, and abnormal development of the gallbladder. Accessory spleens are also represented. These new data on the topography and pathotopography of the abdominal cavity organs are important for correct diagnosis and differentiation between norm and pathology. The presented data can be useful both for students and physicians of different specialties; primarily, for ultrasound diagnosticians. Comparison with topographic anatomy pictures allows previously unknown ultrasonic picture details to be detected in both norm and pathology.

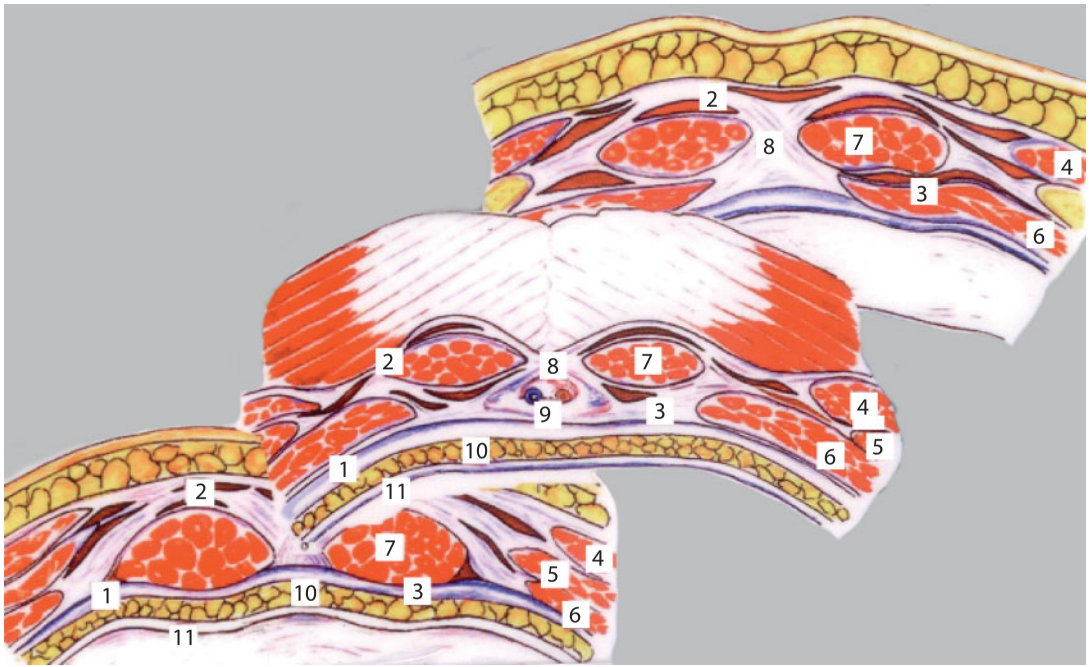

Figure 55 Layer-by-layer topography of the anterior wall of the abdomen.

1. Fascia transversalis; 2. Lamina anterior vaginae mm. recti abdominis; 3. Lamina posterior vaginae mm. recti abdominis; 4. Mobliquus extemus abdominis; 5. m. obliquus interims abdominis; 6. m. rectus abdominis; 7. Linea alba; 8. lig. teres hepatis; 10. Peritoneum.

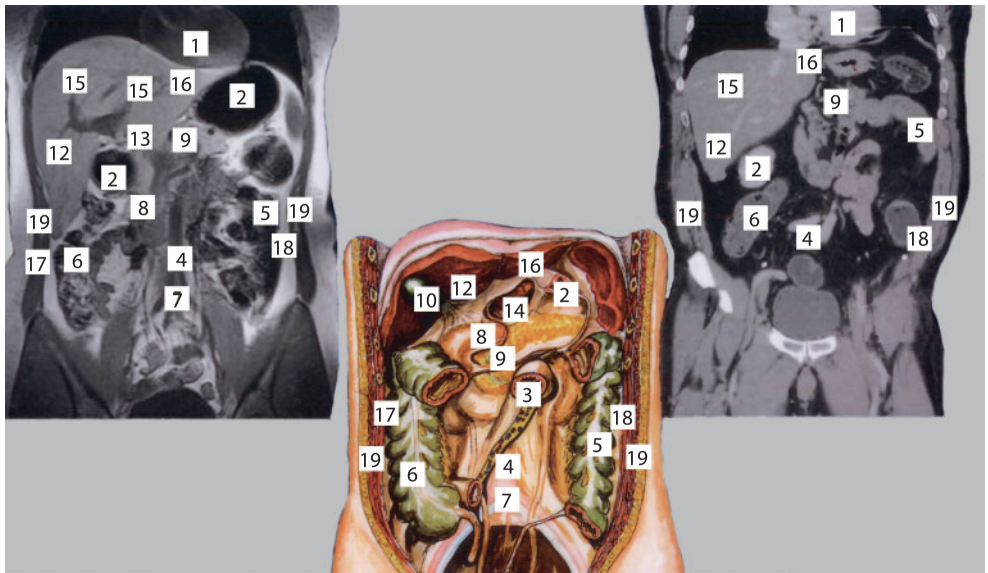

Figure 56 Frontal section of the abdominal cavity.

1. Heart; 2. Stomach; 3. Small intestine; 4. Abdominal aorta; 5. Descending colon; 6. Ascending colon; 7. Inferior vena cava; 8. Ascending colon; 9. Head of pancreas; 10. Gallbladder; 11. Common bile duct; 12. Right hepatic lobe; 13. Portal vein; 14. Caudate lobe of liver; 15. Hepatic veins; 16. Left hepatic lobe; 17. Right lateral canal; 18. Left lateral canal; 19. Lateral wall of the abdomen.

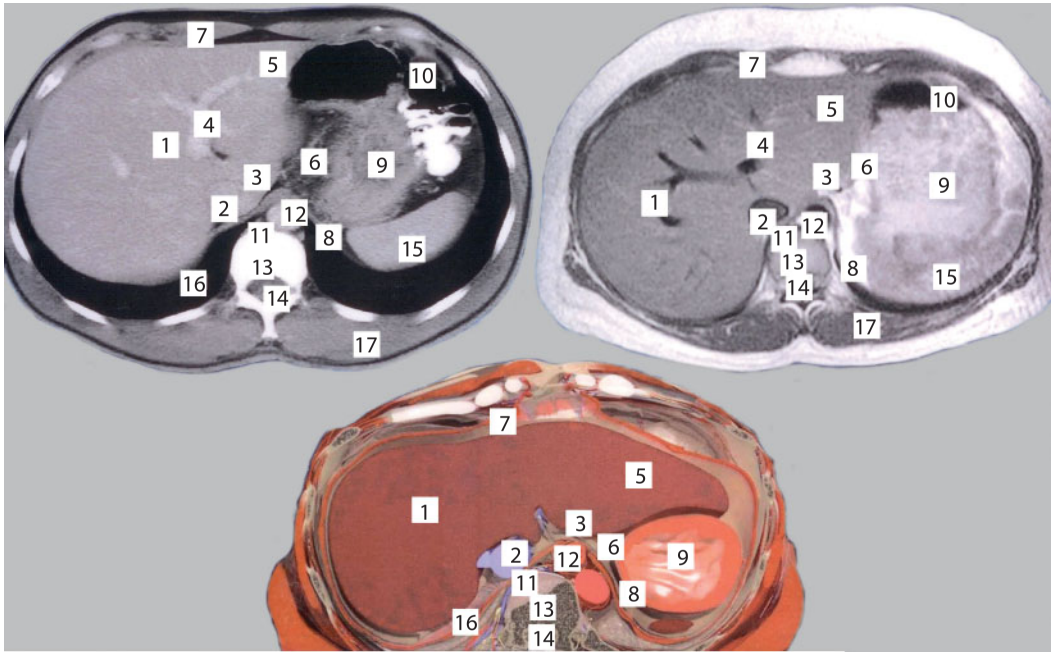

Figure 57 Cross-section at the level of the liver.

1. Right hepatic lobe; 2. Inferior vena cava; 3. Caudate lobe of liver; 4. Portal vein; 5. Left hepatic lobe; 6. Left gastric artery; 7. Rectus; 8. Diaphragm; 9. Stomach; 10. Left deflection of the large intestine; 11. Thoracic duct flow; 12. Abdominal aorta; 13. Dorsal vertebra; 14. Vertebral canal and spinal medulla; 15. Spleen; 16. Right lung; 17. Latissimus dorsi.

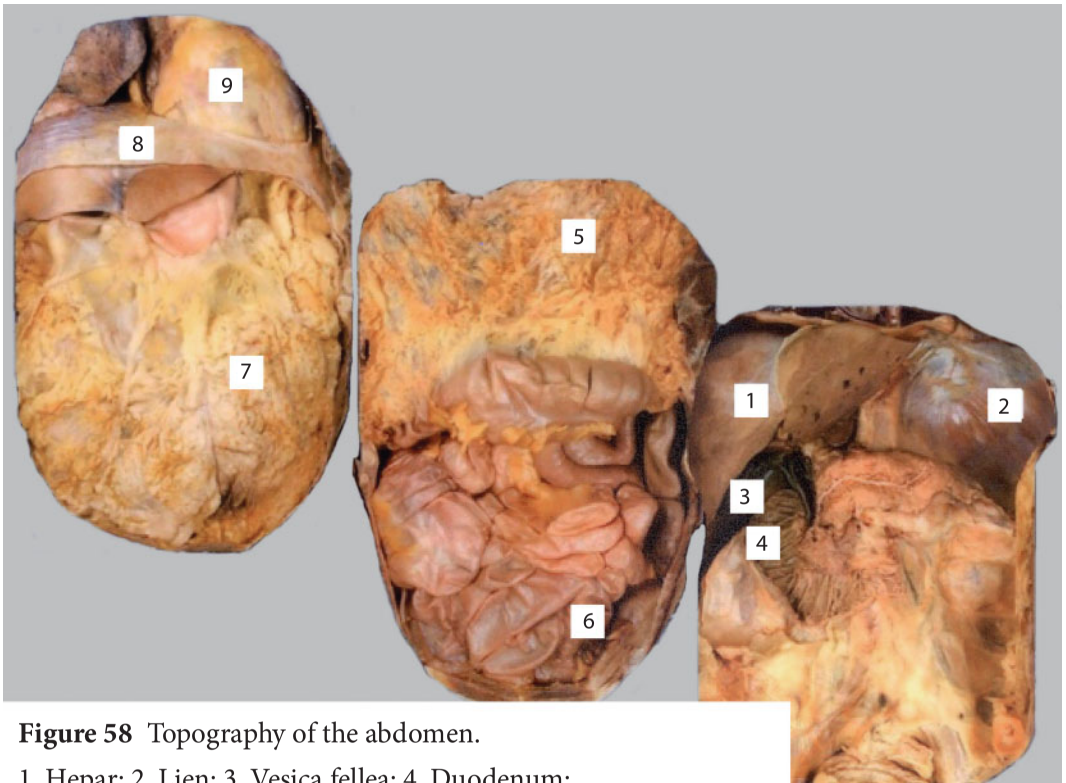

Figure 58 Topography of the abdomen.

1. Hepar; 2. Lien; 3. Vesica fellea; 4. Duodenum;
5. Omentum majus (raised); 6. Ileum; 7. Omentum majus; 8. Diaphragma; 9. Cor.

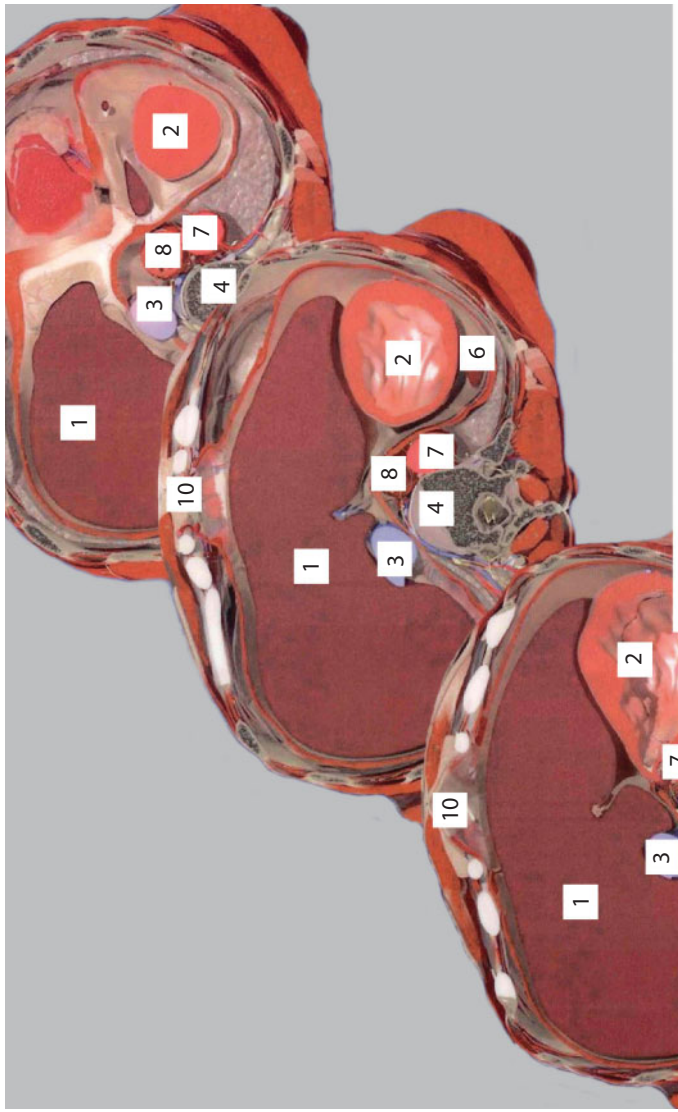

Figure 59 Cross-section at the level of the liver.
1. Liver; 2. Stomach; 3. Inferior vena cava;
4. Vertebra; 6. Spleen; 7. Aorta; 8. Esophagus;
10. Breast bone.

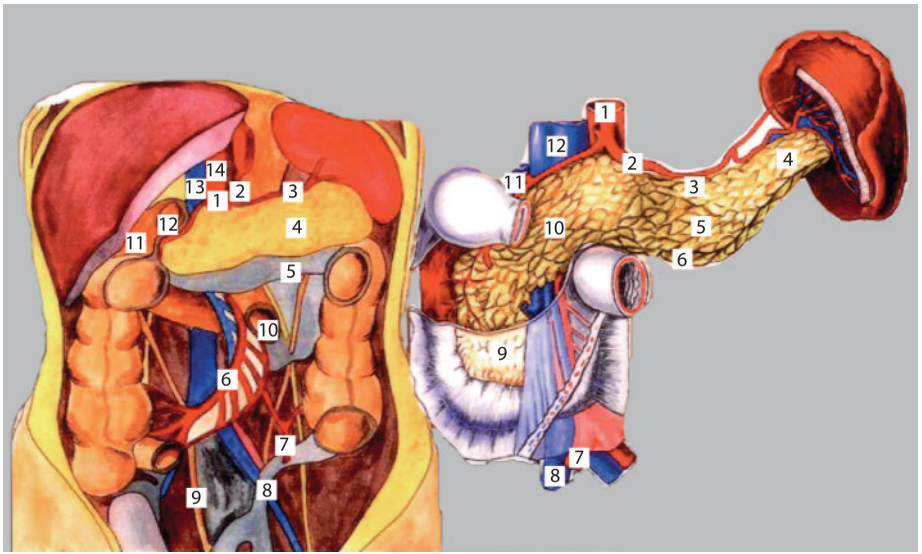

Figure 60 Topography of the abdomen.

1. Truncus coeliacus; 2. A. gastrica dextra; 3. A. licnalis; 4. A. pancreatica; 5. Mesocolon transversum; 6. Vasae mesentericae superiors; 7. A. sigmoideum; 8. Mesocolon sigmoideum; 9. Ureter dexter; 10. Pars superior jejuni; 11. Pars descendens duodeni; 12. Pars horizontalis (inferior) duodeni; 13. V. cava inferior; 14. Aorta abdominalis.

1. Aorta abdominalis; 2. a. lienalis; 3. Margo superior pancreatis; 4. Cauda pancreatis; 5. Margo anterior pancreatis; 6. m inferior pancreatic; 7. a. iliaca communis; 8. v. iliaca communis; 9. Caput pancreatis; 10. Corpus pancreatis; 11. v. portae; 12. v. cava inferior.

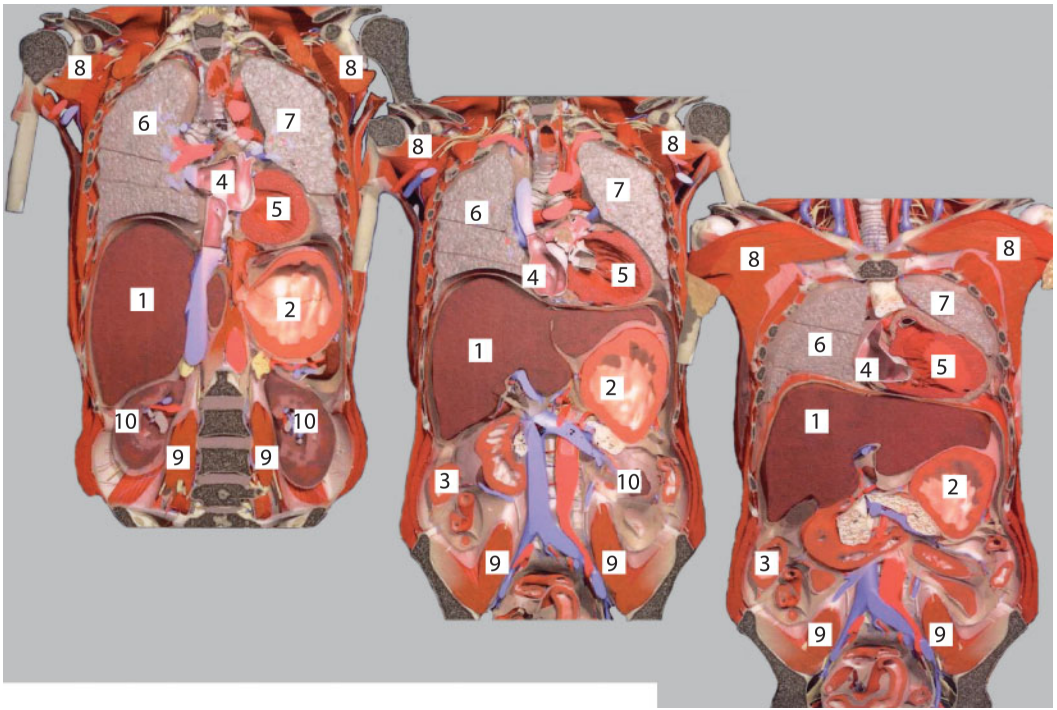

Figure 61 Frontal section at the level of chest and abdomen.

1. Liver; 2. Stomach; 3. Large intestine; 4. Left atrium; 5. Left ventricle; 6. Right lung; 7. Left lung; 8. Greater pectoral muscle; 9. Psoas muscle; 10. Kidney.

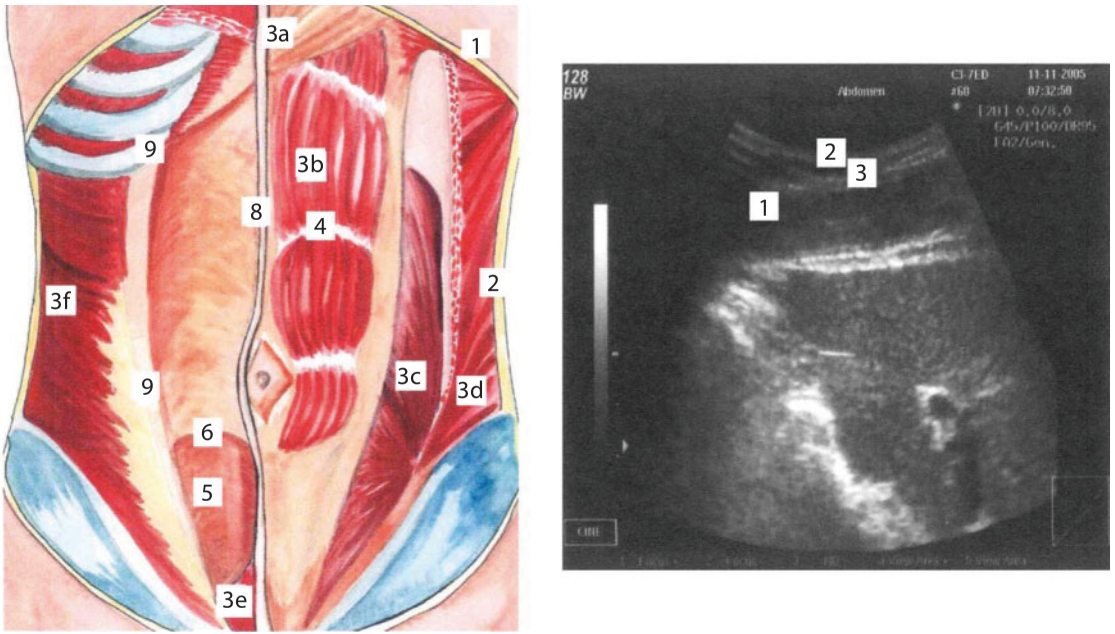

Figure 62 Topography of the anterolateral abdominal wall.

1. Skin; 2. Tendinous intersection; 3. Subcutaneous fat; 3a. Rectus sheath; 3b. Rectus abdominis; 3c. Abdominal internal oblique muscle; 3d. Abdominal external oblique muscle; 3e. Pyramidalis muscle; 3f. Transverse muscle of abdomen; 4. Muscles of the anterior abdominal wall; 5. Transverse fascia; 6. Semicircular line (Douglas line); 7. Semilunar line (Spiegelian line); 8. Linea alba; 9. Costal arch.

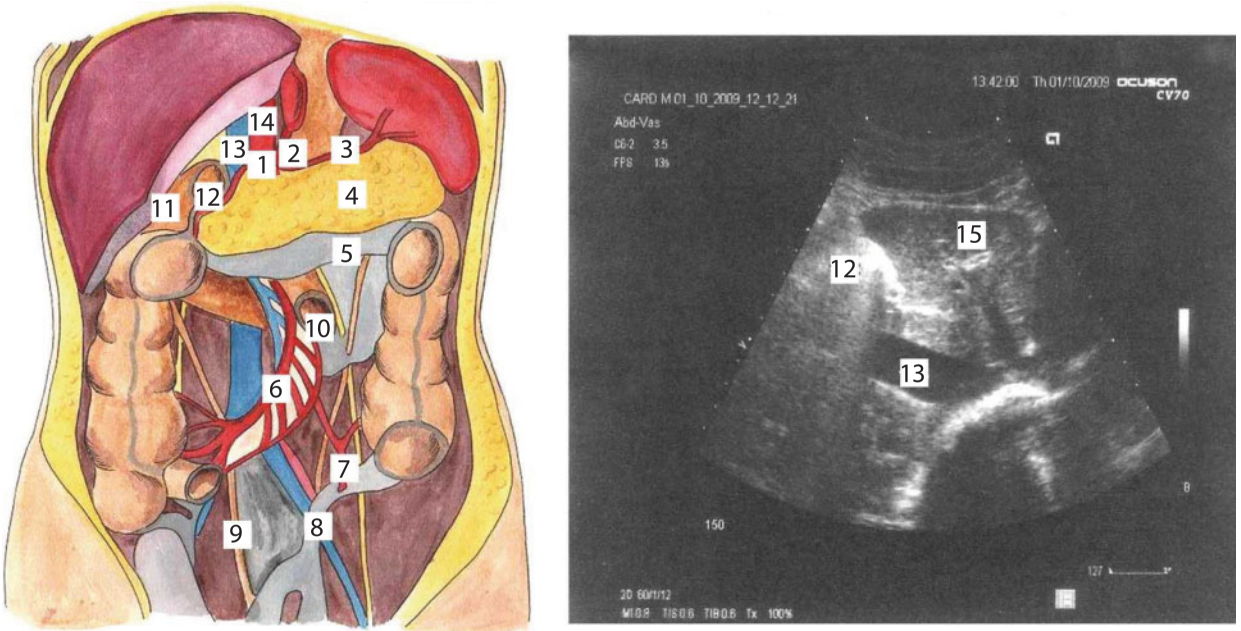

Figure 63 Syntopy of the abdominal cavity organs.

1. Celiac trunk; 2. Right gastric artery; 3. Splenic artery; 4. Pancreas; 5. Mesentery of the transverse colon; 6. Superior mesenteric vessels; 7. Sigmoid artery; 8. Mesosigmoid; 9. Right ureter; 10. Initial segment of the jejunum; 11. Descending duodenum; 12. Upper horizontal part of the duodenum; 13. Inferior vena cava; 14. Abdominal aorta; 15. Left hepatic lobe.

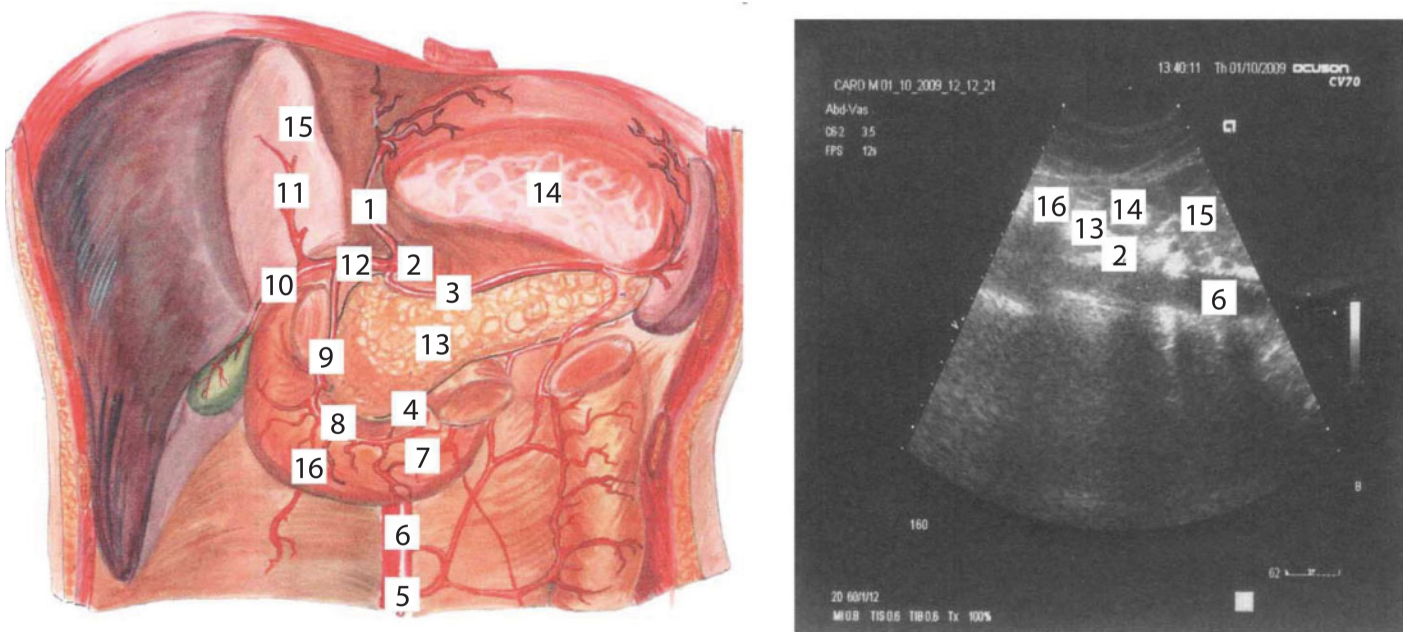

Figure 64 Arteries of the upper part of the abdominal cavity.

1. Left gastric artery; 2. Celiac trunk; 3. Splenic artery; 4. Superior mesenteric artery; 5. Inferior mesenteric artery; 6. Abdominal aorta; 7. Inferior pancreaticoduodenal artery; 8. Superior pancreaticoduodenal artery; 9. Gastroduodenal artery; 10. Right branch of the hepatic artery; 11. Left branch of the hepatic artery; 12. Common hepatic artery; 13. Pancreas; 14. Stomach; 15. Left hepatic lobe; 16. Duodenum.

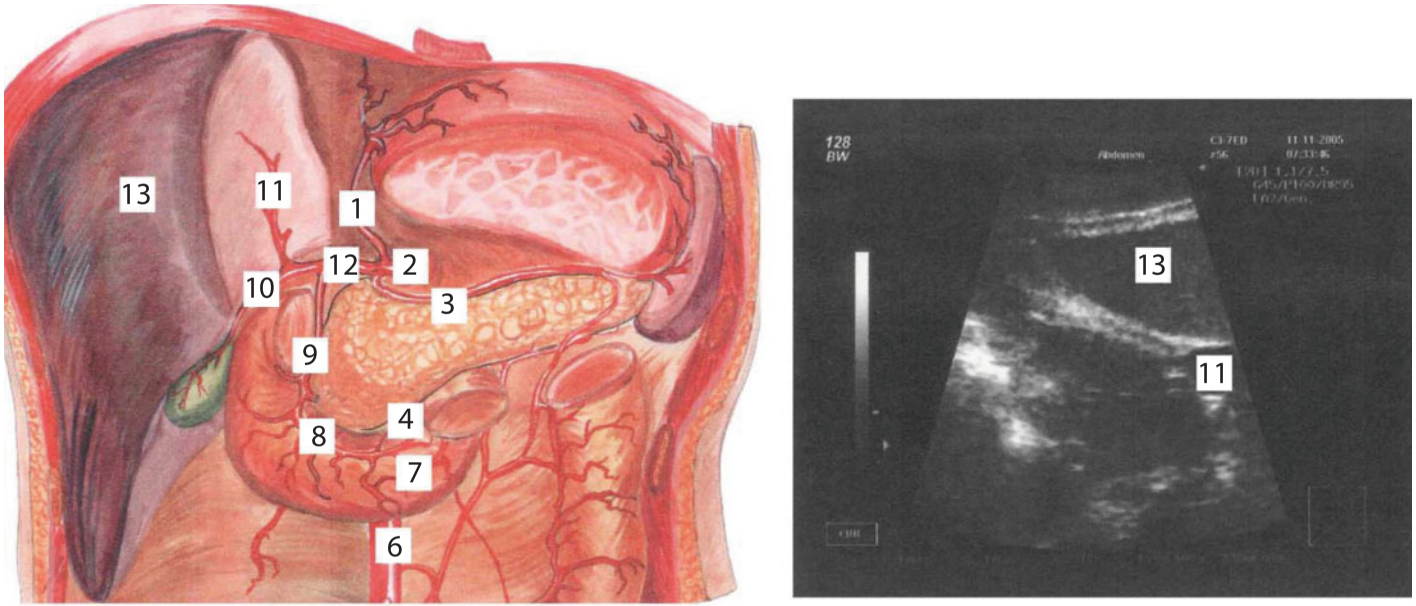

Figure 65 Arteries of the upper part of the abdominal cavity.

1. Left gastric artery; 2. Celiac trunk; 3. Splenic artery; 4. Superior mesenteric artery; 5. Inferior mesenteric artery; 6. Abdominal aorta; 7. Inferior pancreaticoduodenal artery; 8. Superior pancreaticoduodenal artery; 9. Gastroduodenal artery; 10. Right branch of the hepatic artery; 11. Left branch of the hepatic artery; 12. Common hepatic artery; 13. Liver.

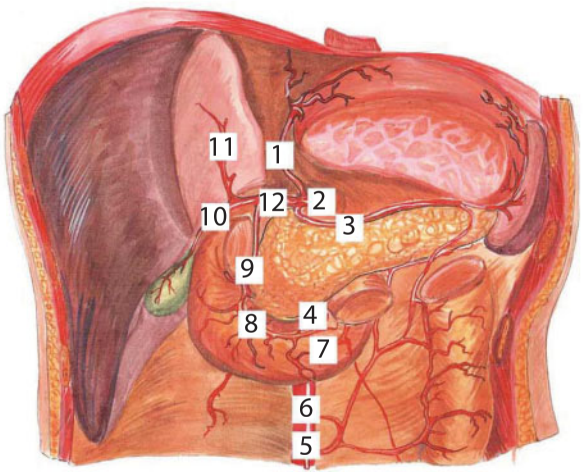

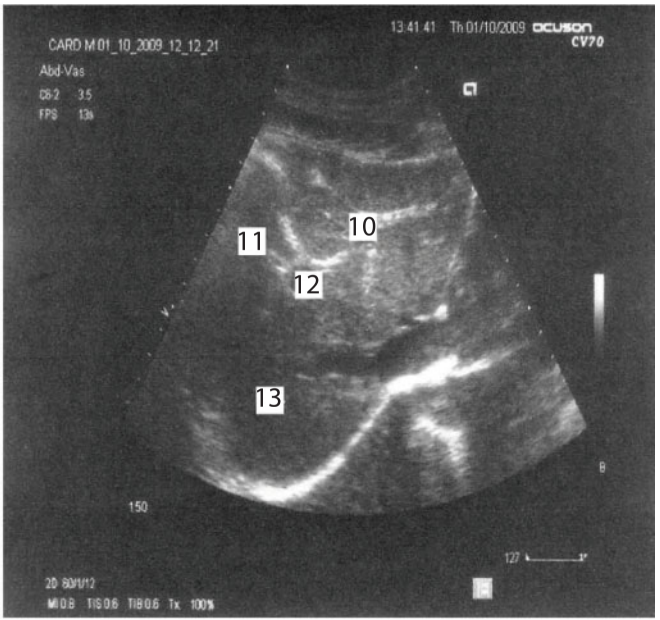

Figure 66 Arteries of the upper part of the abdominal cavity.

1. Left gastric artery; 2. Celiac trunk; 3. Splenic artery; 4. Superior mesenteric artery; 5. Inferior mesenteric artery; 6. Abdominal aorta; 7. Inferior pancreaticoduodenal artery; 8. Superior pancreaticoduodenal artery; 9. Gastroduodenal artery; 10. Right branch of the hepatic artery; 11. Left branch of the hepatic artery; 12. Common hepatic artery; 13. Right hepatic lobe.

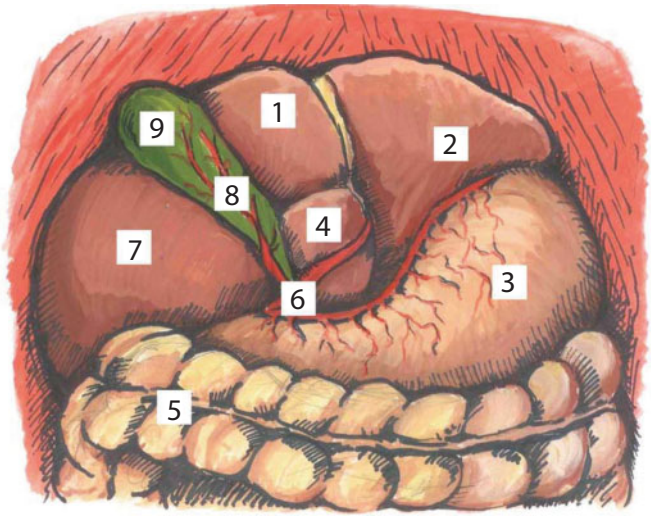

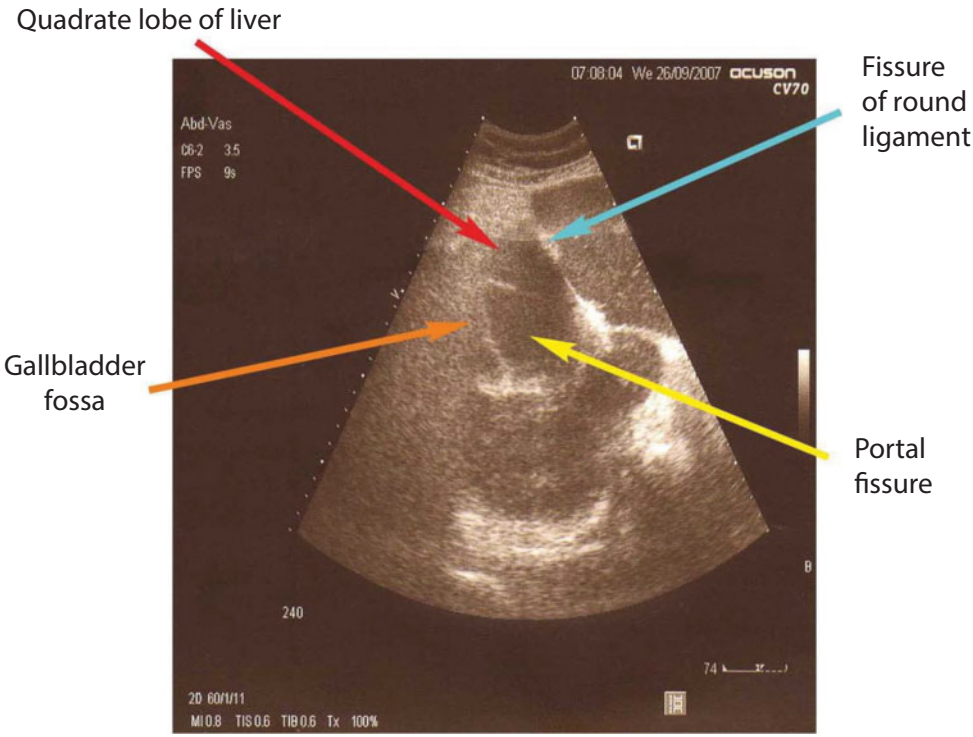

Figure 67 Liver.

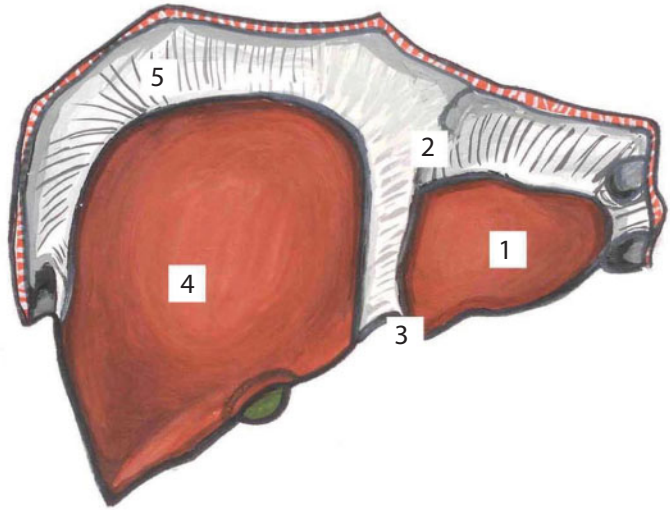

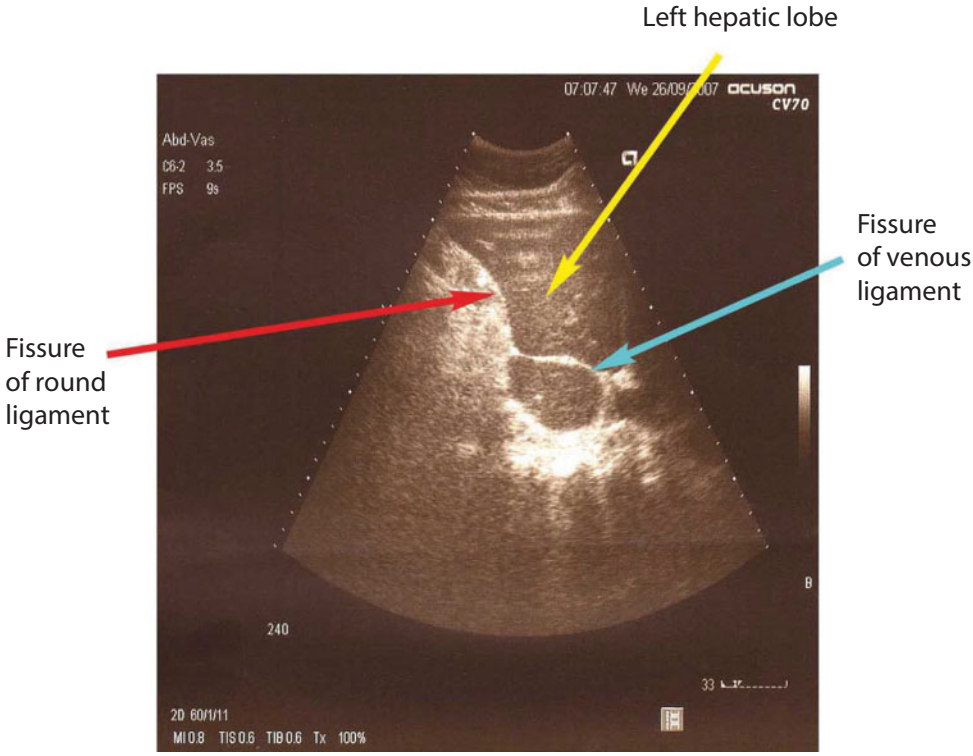

Figure 68 Liver.

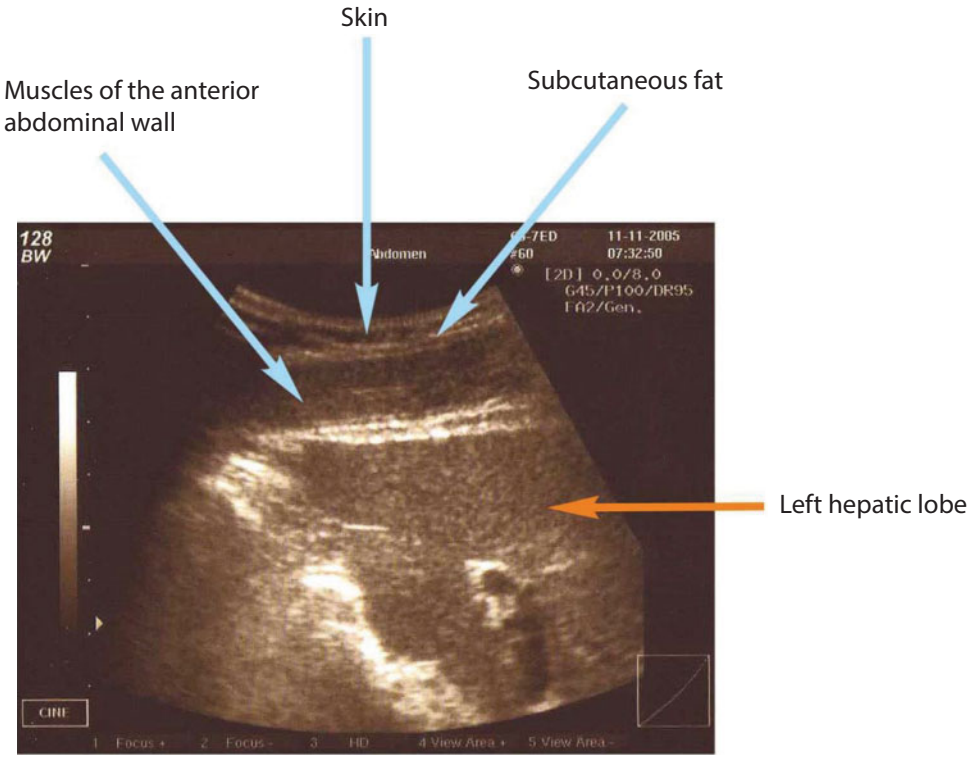

Figure 69 Liver.

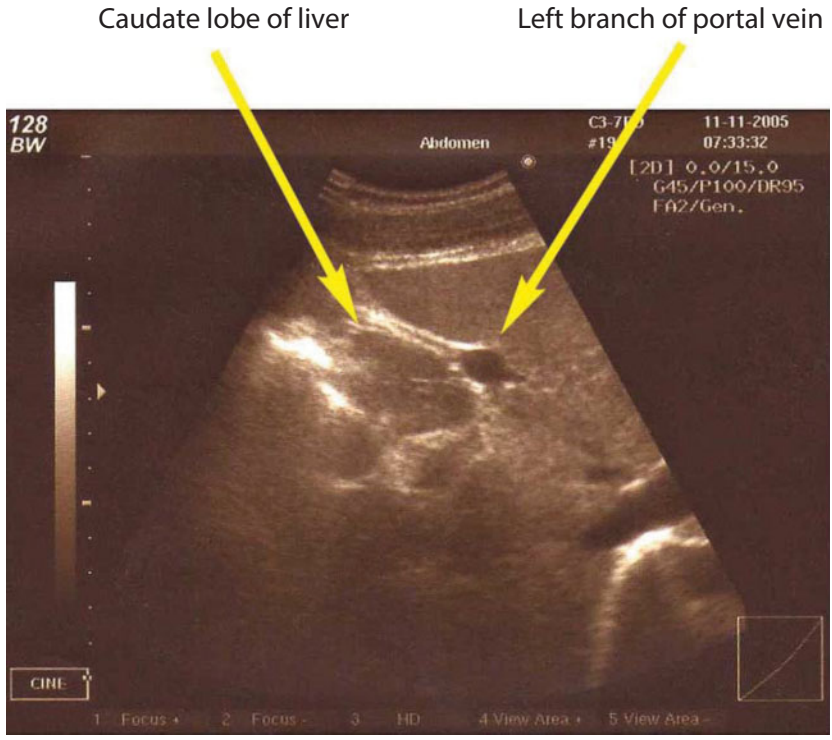

Figure 70 Liver.

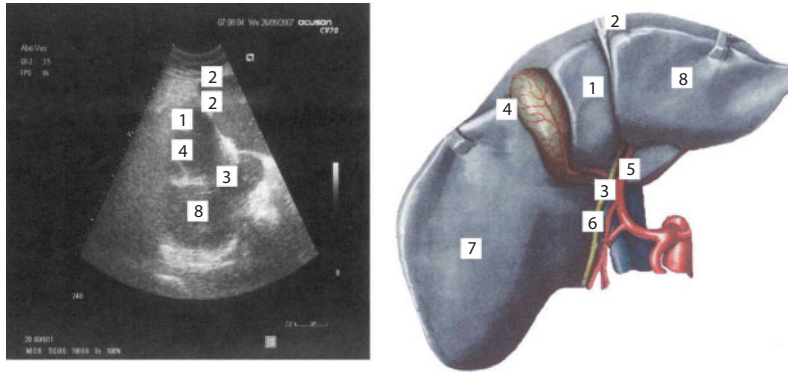

Figure 71 Liver.

1. Quadrate lobe of liver; 2. Grooves of round ligament; 3. Portal fissure; 4. Gallbladder bed; 5. Inherent hepatic artery; 6. Ductus choledochus; 7. Right hepatic lobe; 8. Left hepatic lobe.

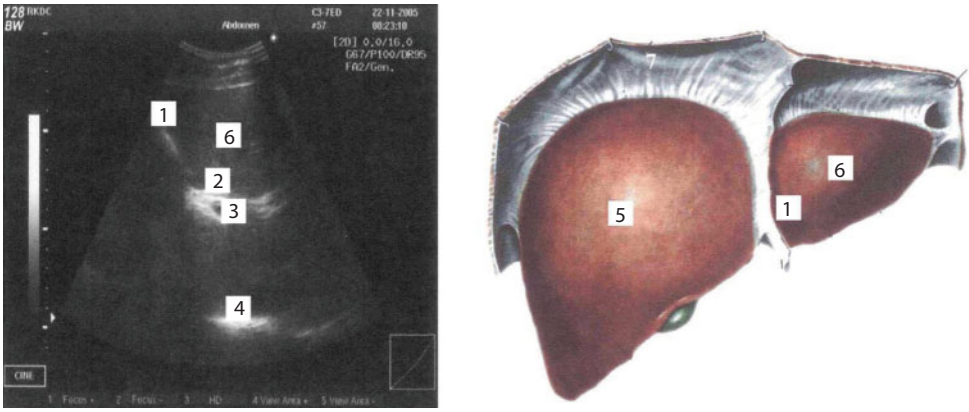

Figure 72 Liver.

1. Fissure of round ligament; 2. Left branch of intrahepatic ducts; 3. Left branch of portal vein; 4. Notch for venous ligament; 5. Right hepatic lobe; 6. Left hepatic lobe; 7. Coronary hepatic ligament.

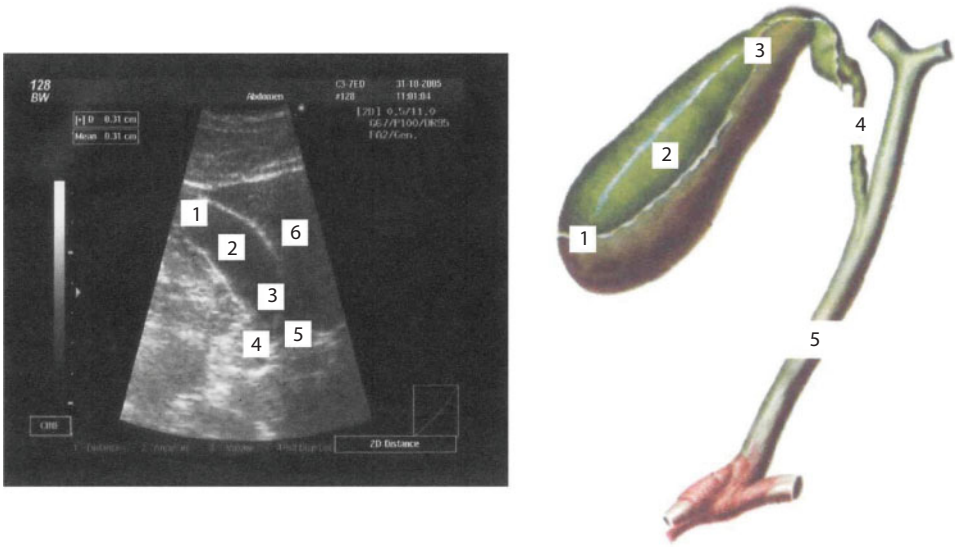

Figure 73 Gallbladder.

1. Gallbladder bottom; 2. Body of the gallbladder; 3. Gallbladder cervix; 4. Cystic duct; 5. Ductus choledochus; 6. Liver.

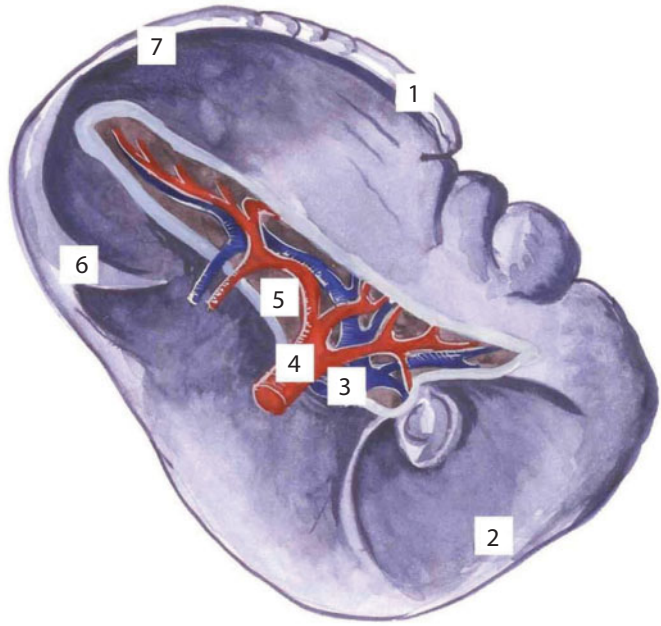

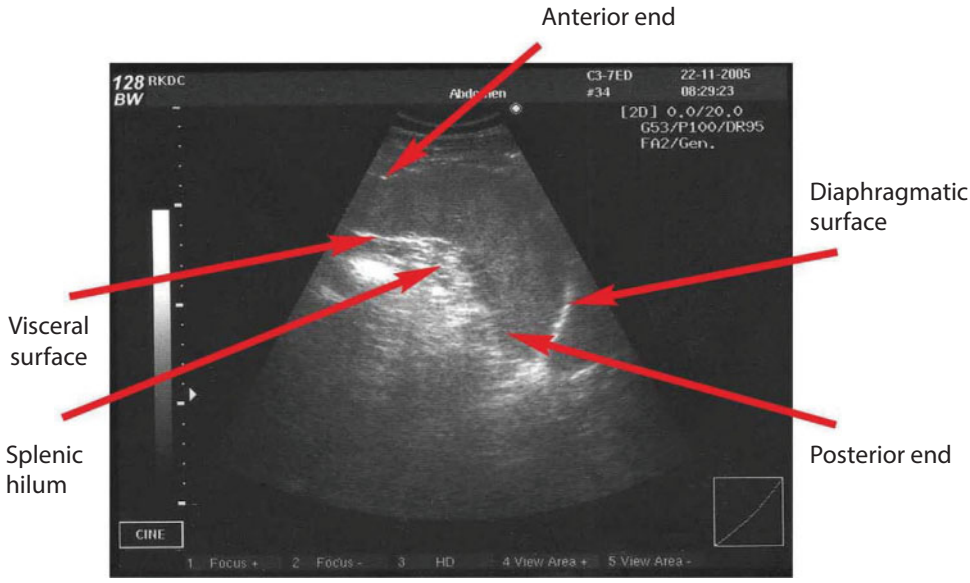

Figure 74 Spleen.

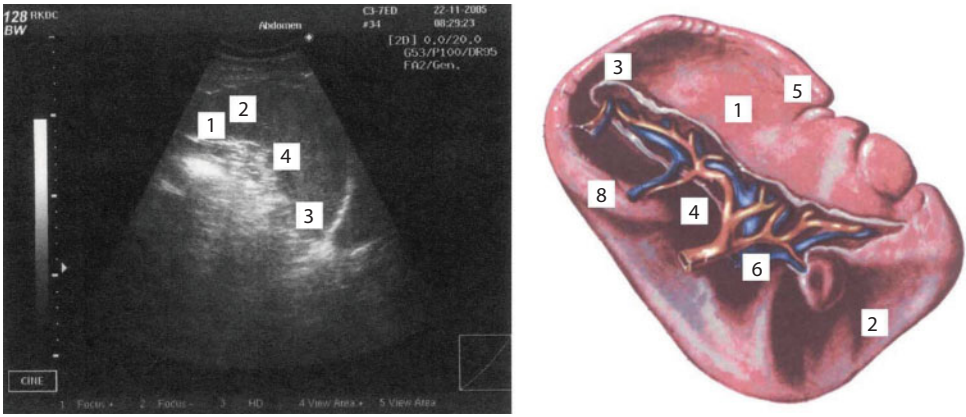

Figure 75 Spleen.

1. Visceral surface; 2. Anterior end; 3. Posterior end; 4. Splenic hilum; 5. Superior border; 6. Splenic vein; 7. Splenic artery; 8. Inferior border.

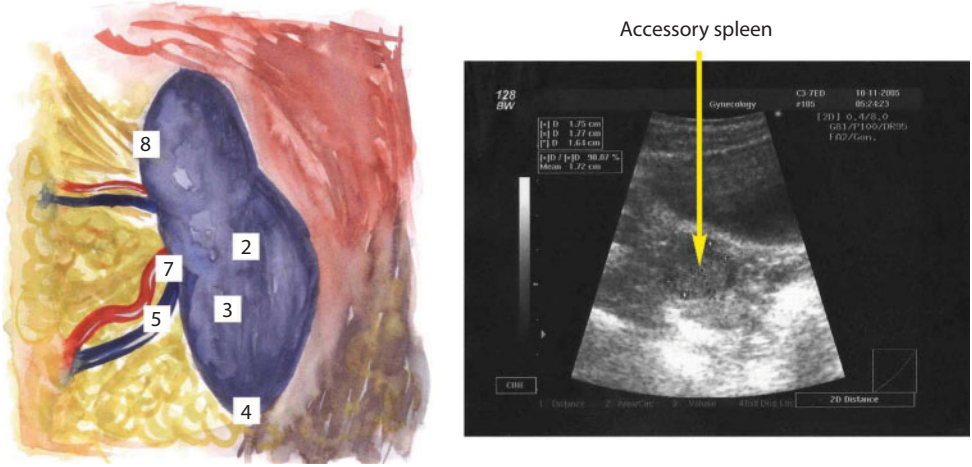

Figure 76 Spleen.

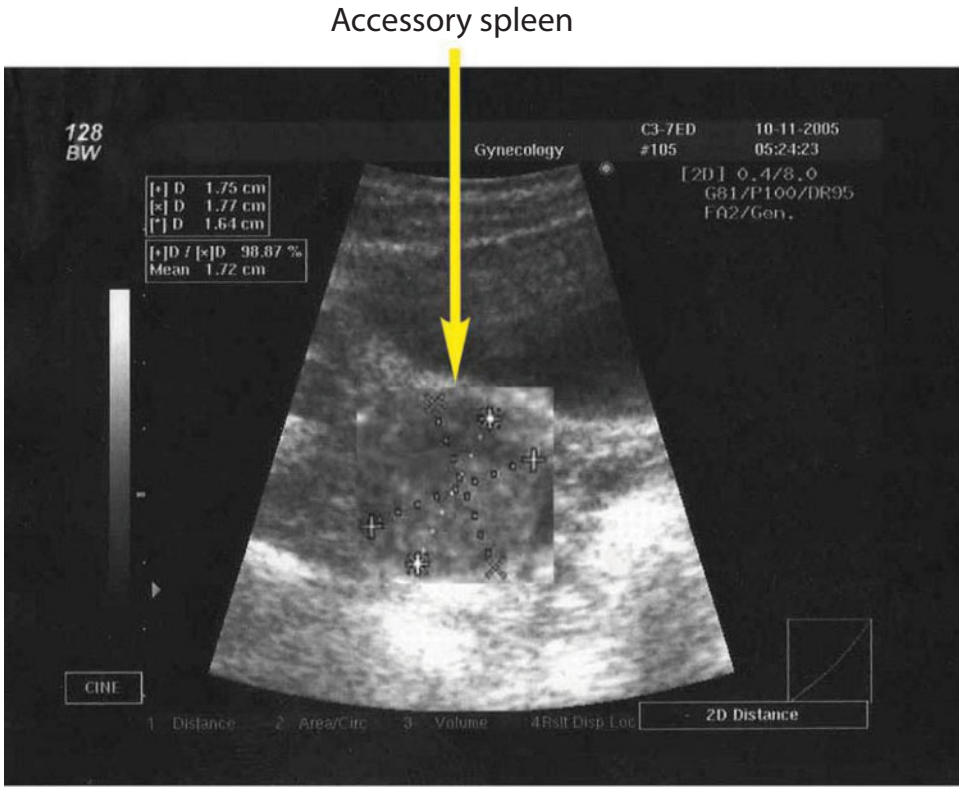

Figure 77 Spleen.

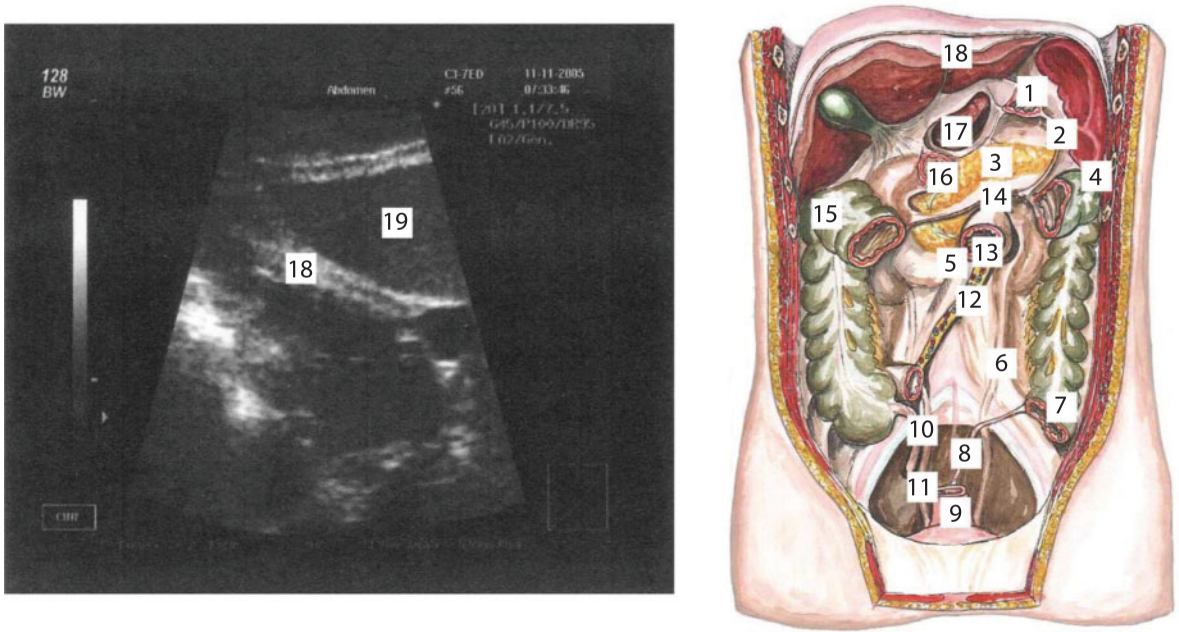

Figure 78 Lines of attachment of mesostenium and mesocolon.

1. Cardia; 2. Gastrosplenic ligament; 3. Pancreas; 4. Phrenicocolic ligament; 5. Ascending duodenum; 6. Mucosal relief of the left ureter; 7. Sigmoid; 8. Mesosigmoid; 9. Rectum; 10. Appendix; 11. Mucosal relief of the right ureter; 12. Root of the mesentery; 13. Duodenojejunal junction; 14. Mesentery of transverse colon; 15. Right colic flexure; 16. Gastrohepatic omentum; 17. Falciform ligament of the liver; 18. Liver.

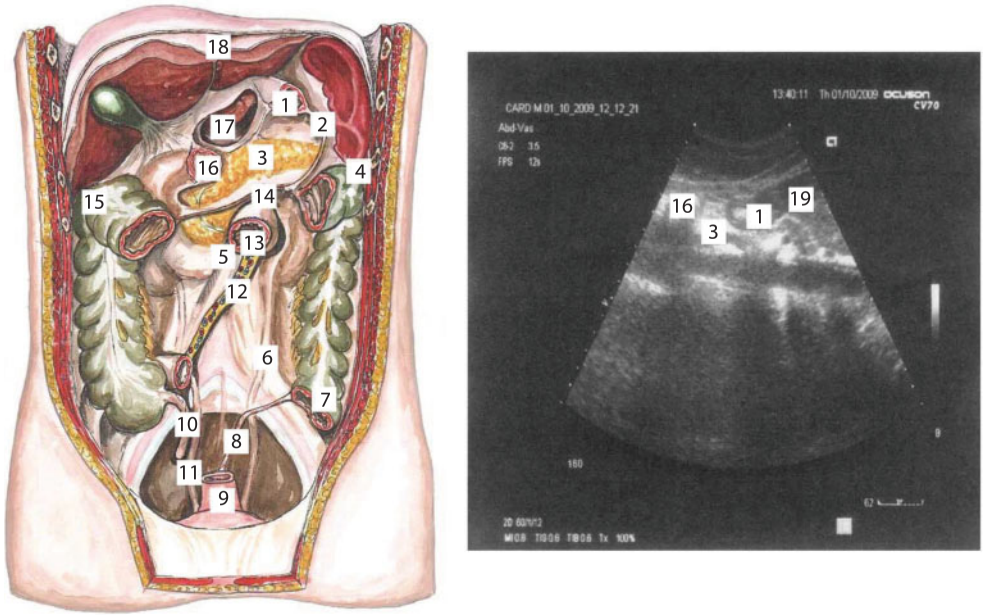

Figure 79 Lines of attachment of mesostenium and mesocolon.

1. Cardia; 2. Gastrosplenic ligament; 3. Pancreas; 4. Phrenicocolic ligament; 5. Ascending duodenum; 6. Mucosal relief of the left ureter; 7. Sigmoid; 8. Mesosigmoid; 9. Rectum; 10. Appendix; 11. Mucosal relief of the right ureter; 12. Root of mesentery; 13. Duodenojejunal junction; 14. Mesentery of transverse colon; 15. Right colic flexure; 17. Gastrohepatic omentum; 18. Falciform ligament of the liver; 19. Left hepatic lobe.

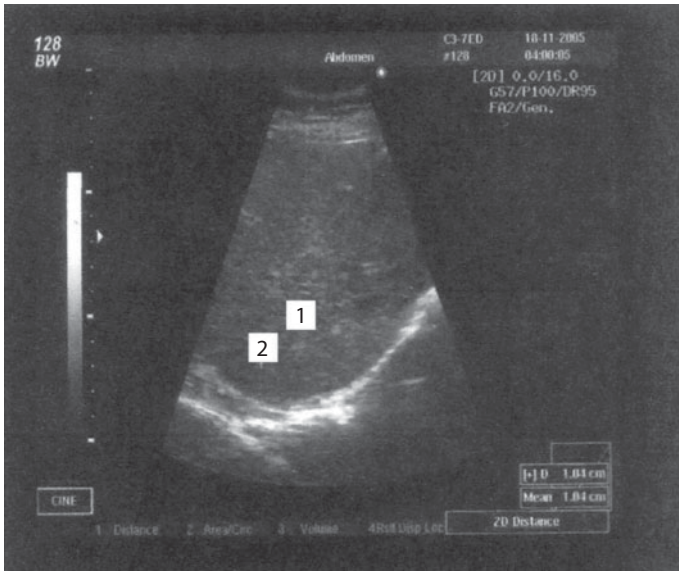

Figure 80 Liver pathology.
1. Right hepatic lobe; 2. Hemangioma of the right hepatic lobe.

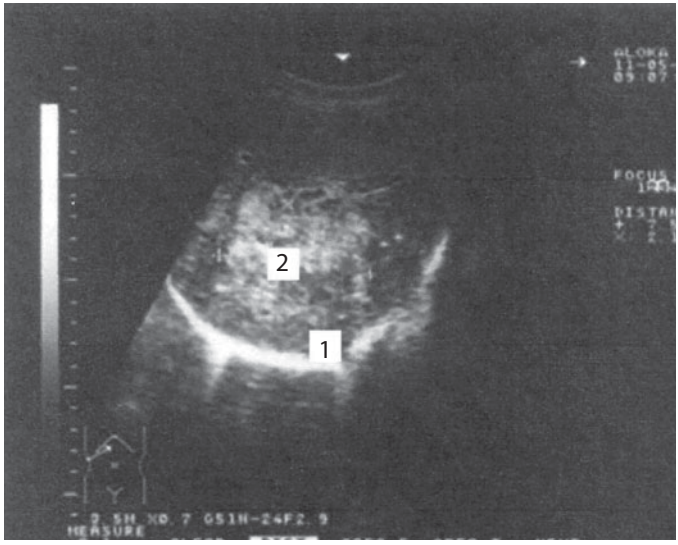

Figure 81 Tumor of the right hepatic lobe.
1. Right hepatic lobe; 2. Tumor-like mass.

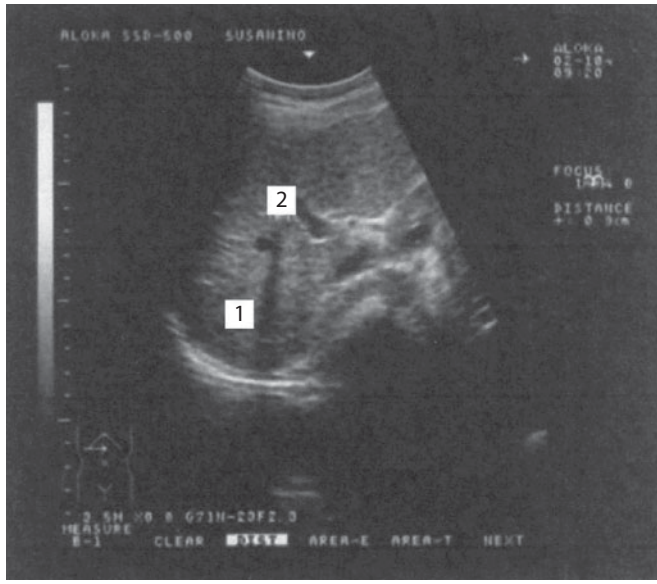

Figure 82 Liver concrement.

1. Liver; 2. Concrement.

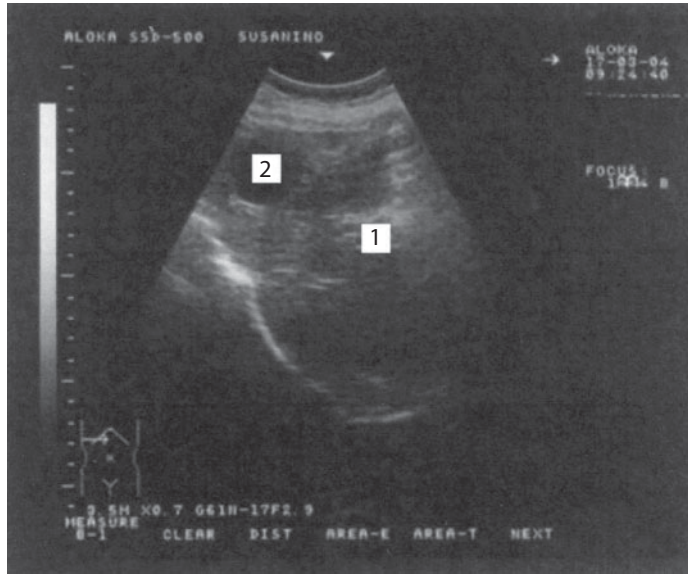

Figure 83 Hepatic cyst.

1. Liver; 2. Cyst.

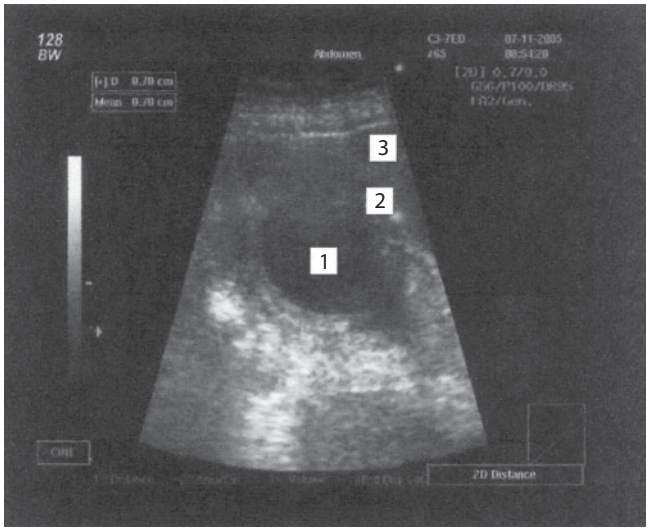

Acute cholecystitis

Figure 84 Gallbladder pathology.

1. Body of the gallbladder; 2. Thick wall of the gallbladder; 3. Liver.

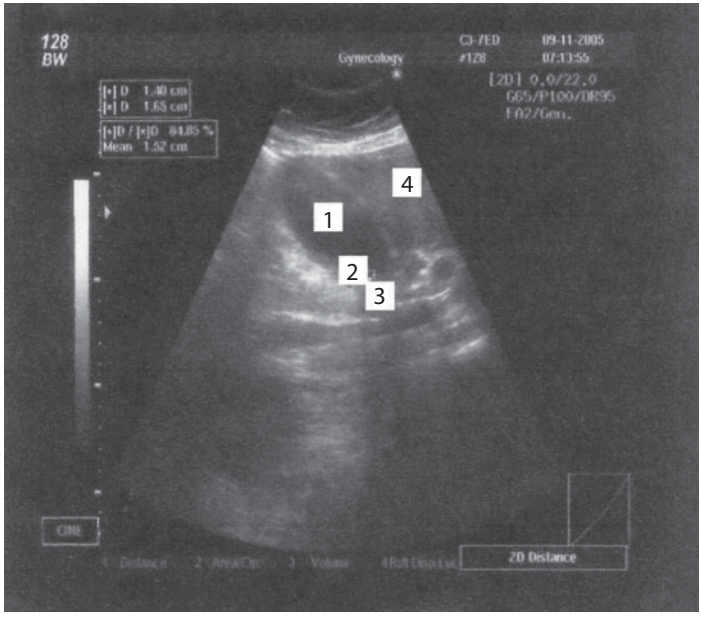

Figure 85 Cholelithiasis.

1. Body of the gallbladder; 2. Cystic duct; 3. Concrement; 4. Liver.

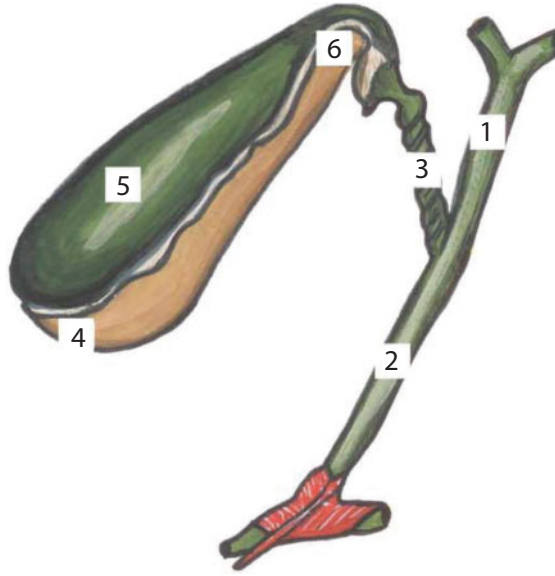

Figure 86 Biliary system.

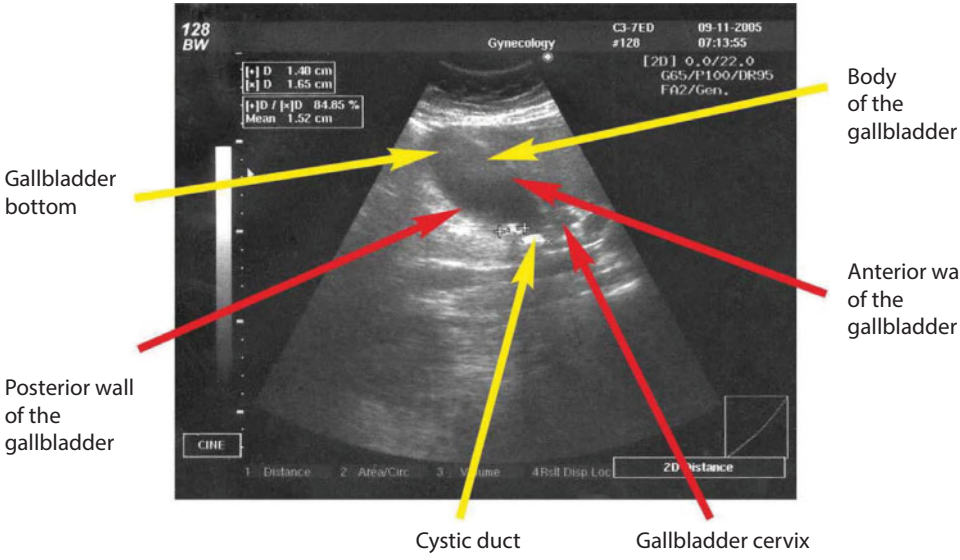

Figure 87 Gallbladder.

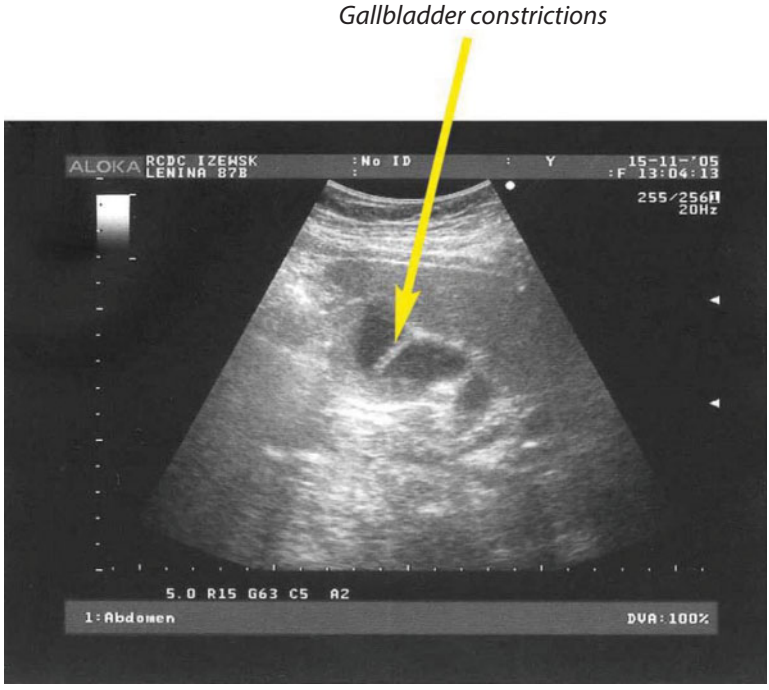

Figure 88 Abnormal development of the gallbladder.

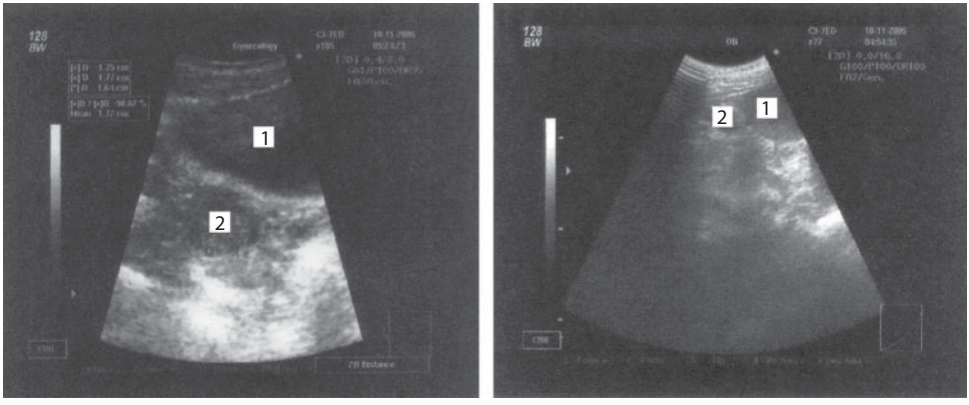

Figure 89 Spleen pathology.

1. Spleen; 2. Accessory spleen.

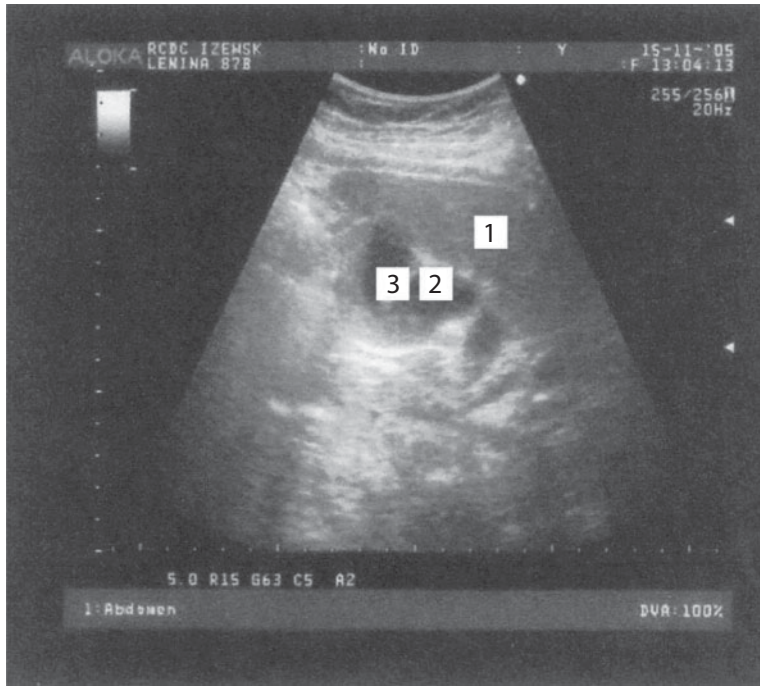

Figure 90 Abnormal development of the gallbladder.

1. Liver; 2. Gallbladder; 3. Gallbladder constrictions.

Topographical and Pathotopographical Anatomy of the Retroperitoneal Space

Topographical and pathotopographical anatomy of the retroperitoneal space is represented by the layer-by-layer topographical anatomy. Abdominal aorta and kidneys are compared with contrastless angiograms. Renal pyramids, parenchyma, sinuses, upper pole, duplication of the pelvicalyceal system are differentiated in kidneys. Renal circulation is represented by the renal artery, interlobar and interlobular arteries. Ultrasonic testing of the pancreas provides valuable diagnostic information for differentiation of the pancreas segments and celiac trunk and aorta, as well as the right hepatic artery and superior mesenteric vein.

Changes in the structure of pancreatic parenchyma caused by chronic pancreatitis, pancreatic cyst, renal cyst, urolithiasis, tumors and renal hemangioma are of significant diagnostic value. Extension of the boundaries of differential diagnosis of focal and diffuse pathologies of the retroperitoneal space organs, as well as correlation with pathotopographical anatomy typical for a specific diagnosis, provide new, promising, and atraumatic methods of examination.

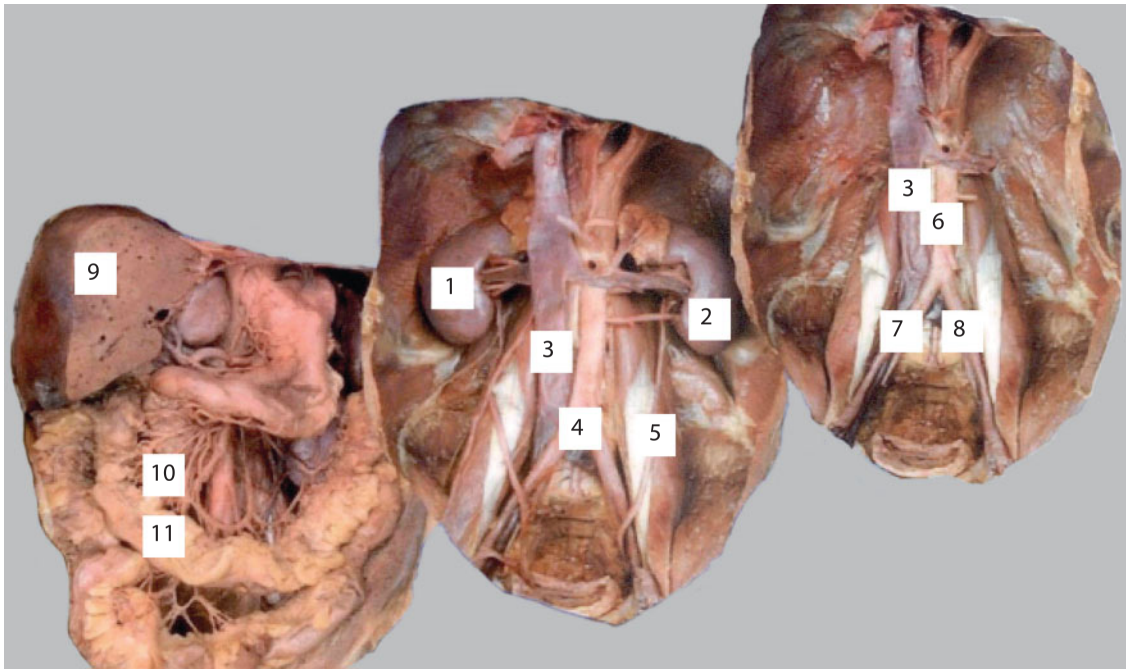

Figure 91 Retroperitoneal space organs.

1. Ren dexter; 2. Ren sinister; 3. Vena cava inferior; 4. Bifurcation aortae abdominis; 5. Ureter; 6. Aorta abdominalis; 7. a. iliaca communis dextra; 8. a. iliaca communis sinistra; 9. Hepar; 10. aa. jejunales; 11. Intestinum tenue.

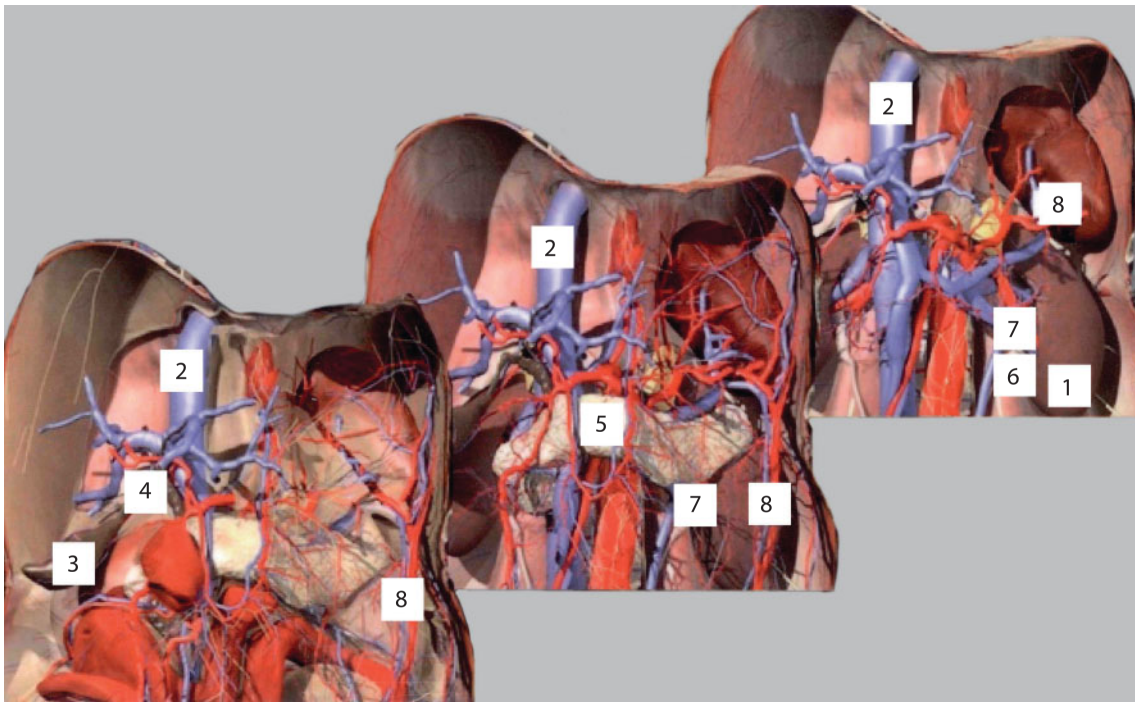

Figure 92 Blood vessels of the retroperitoneal space.

1. Ren; 2. Vena cava inferior; 3. Vesica fellea; 4. Ductus cysticus; 5. Pancreas; 6. Ureter; 7. v. renalis; 8. a et v. lienalis.

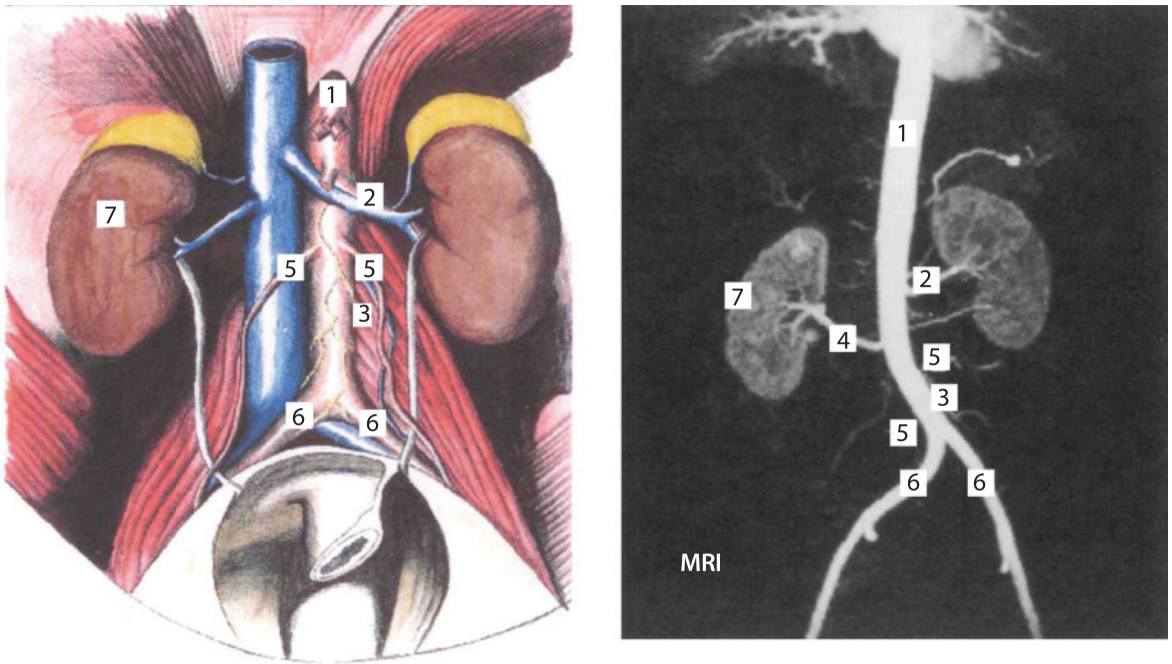

Figure 93 Abdominal aorta and kidneys. Contrastless angiography.

1. Abdominal aorta; 2. Renal artery; 3. Inferior mesenteric artery; 4. Renal artery; 5. Lumbar arteries; 6. Common iliac artery; 7. Kidneys.

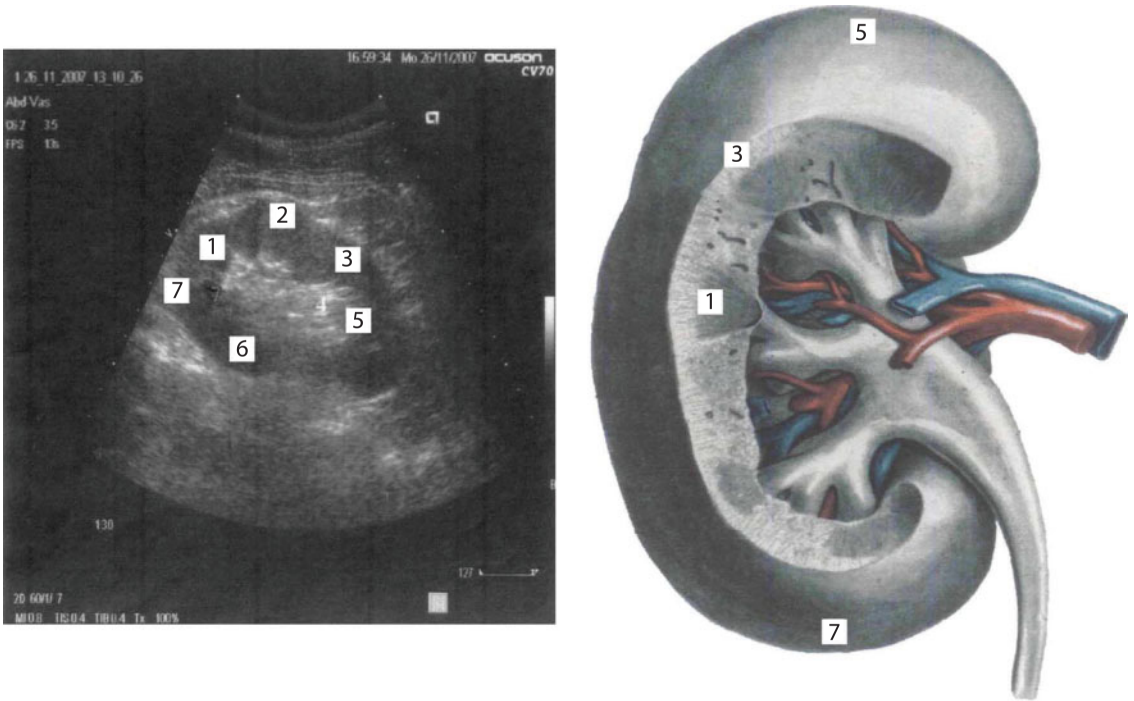

Figure 94 Kidney.

1. Pyramids (renal medulla); 2. Lateral surface; 3. Parenchyma (renal cortex); 4. Renal sinus; 5. Upper pole; 6. Medial side; 7. Lower pole.

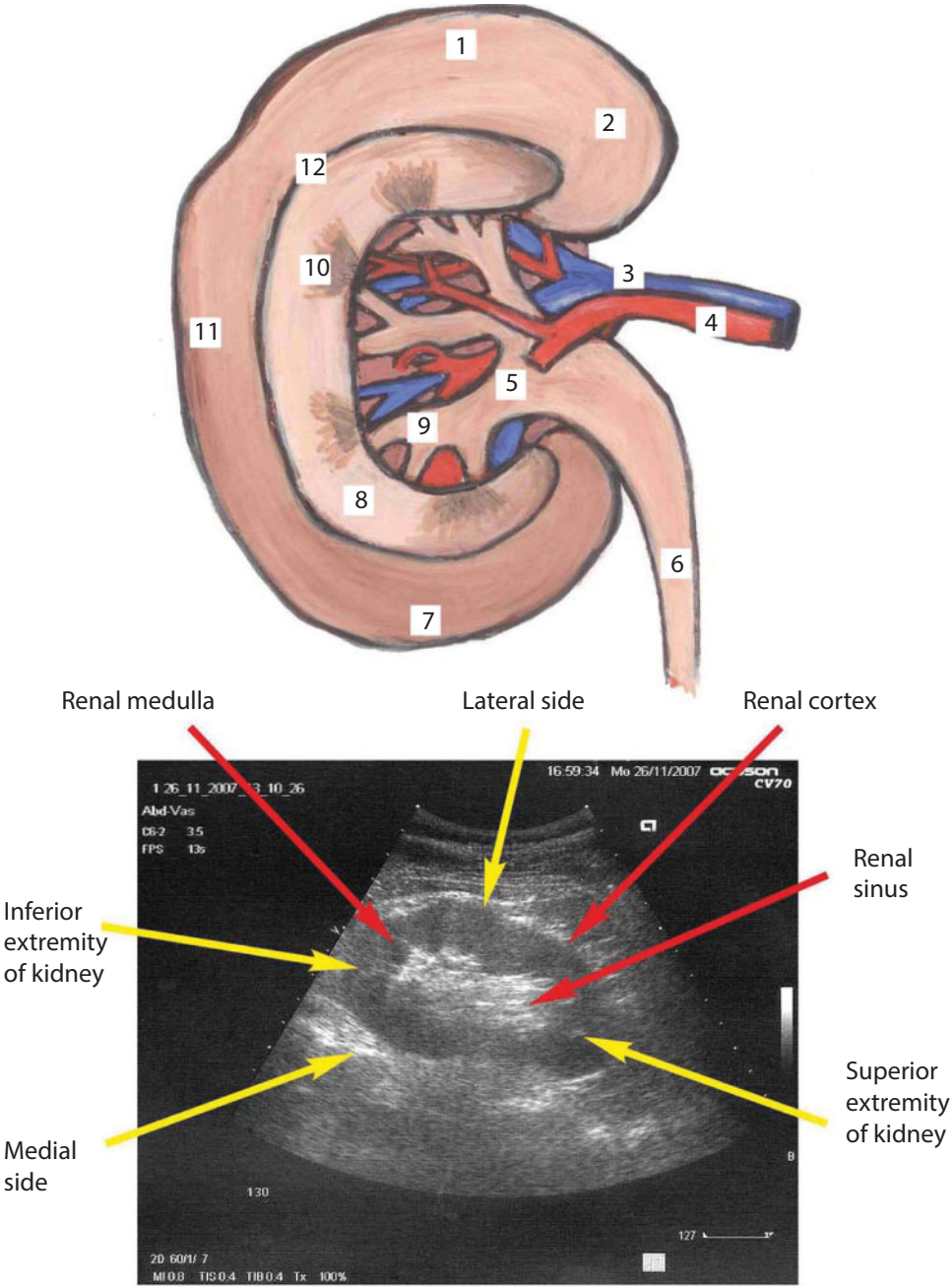

Figure 95 Kidney.

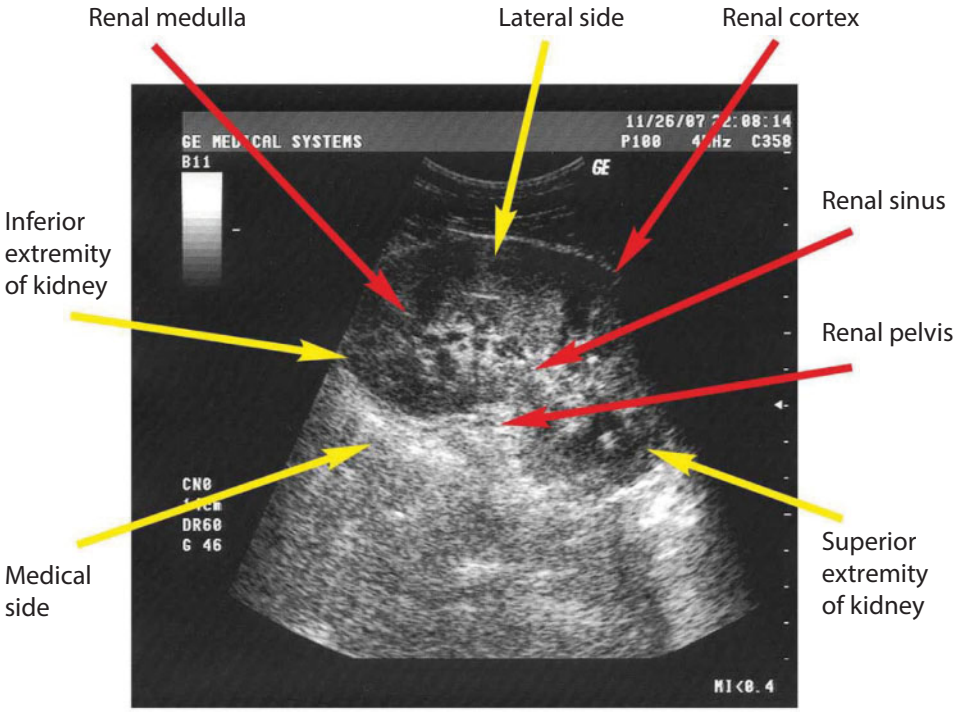

Figure 96 Kidney.

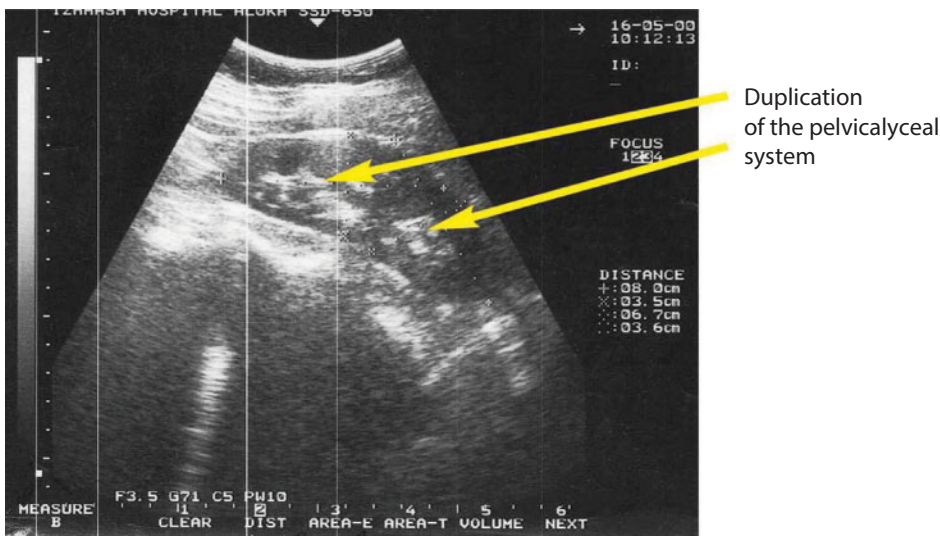

Figure 97 Kidney.

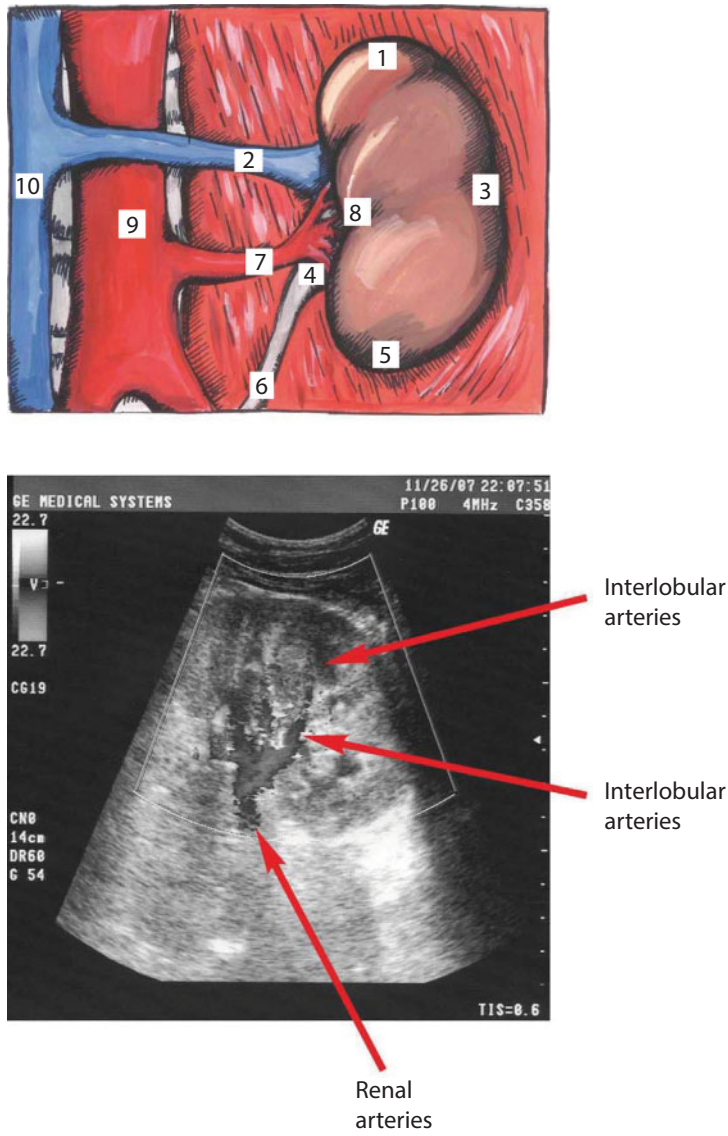

Figure 98 Renal circulation.

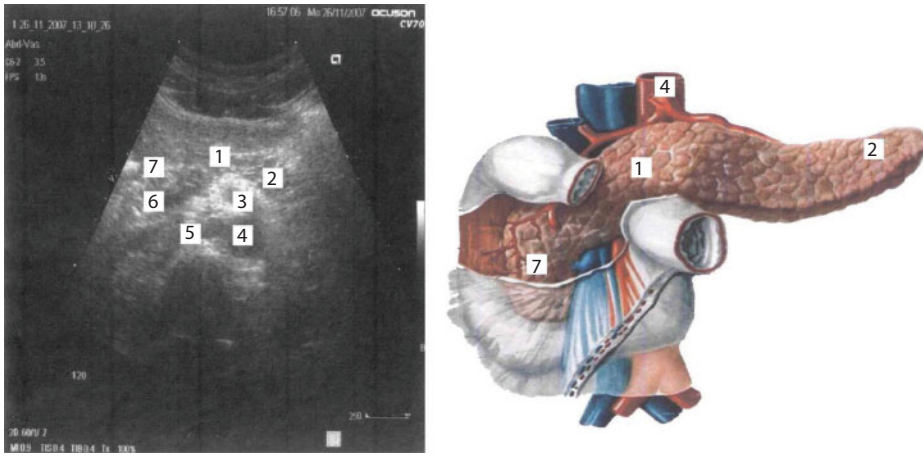

Figure 99 Pancreas.

1. Body of pancreas; 2. Tail of pancreas; 3. Celiac trunk; 4. Aorta; 5. Right hepatic artery; 6. Superior mesenteric vein; 7. Head of pancreas.

Pancreas pathology

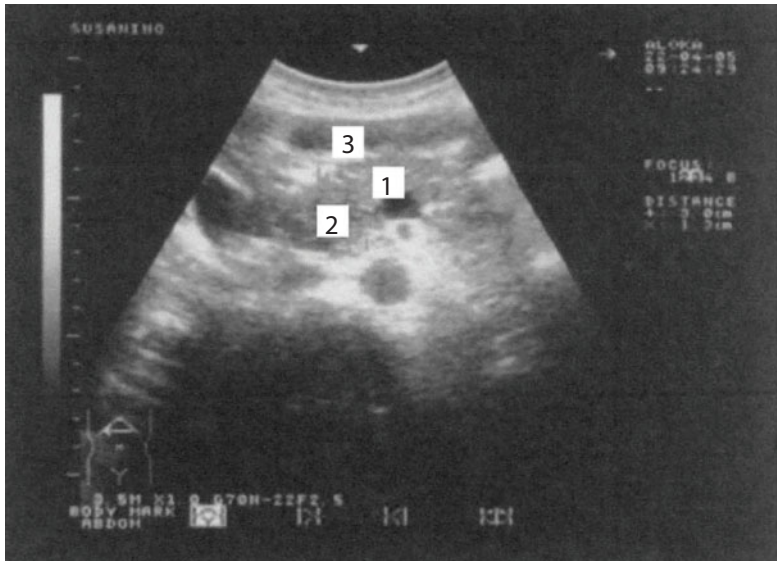

Figure 100 Chronic pancreatitis.

1,2. Modified structure of pancreatic parenchyma; 3. Liver.

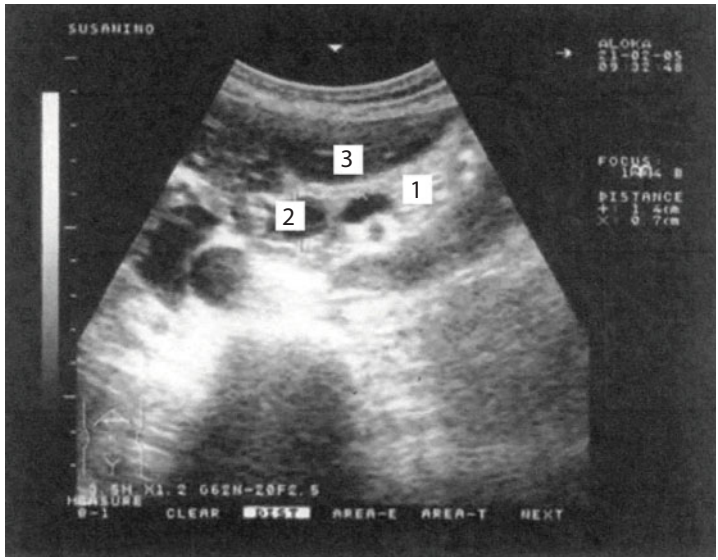

Figure 101 Pancreatic cyst.

1. Pancreas; 2. Pancreatic cyst; 3. Liver.

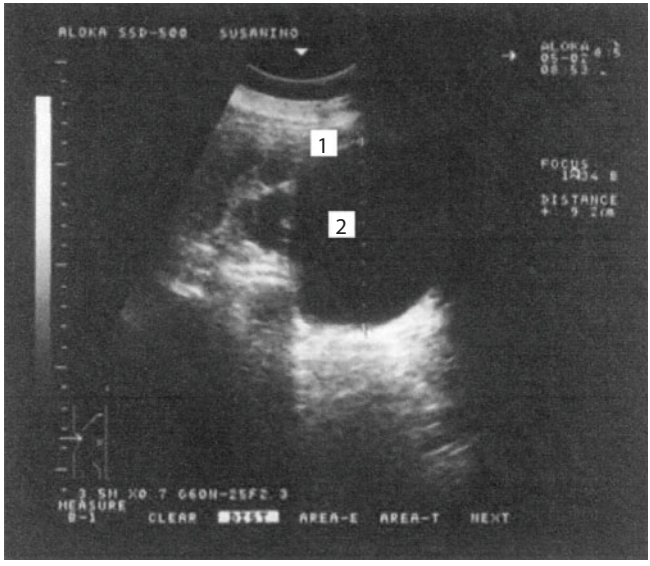

Figure 102 Renal cyst.

1. Kidney; 2. Cyst.

Hepatic pathology

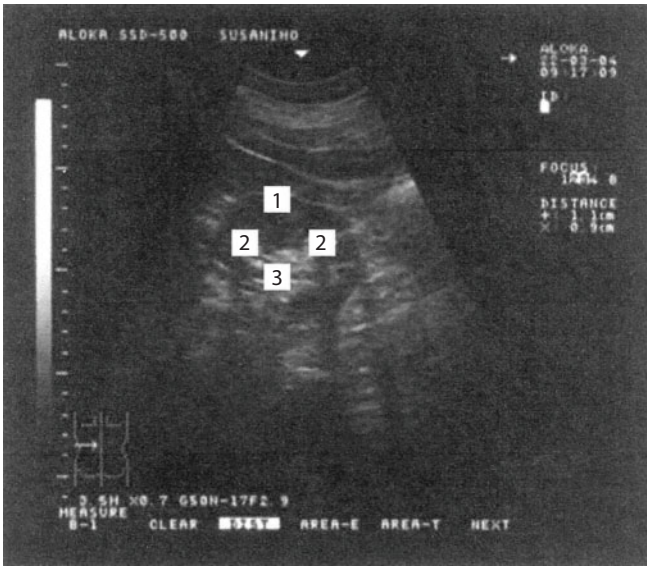

Figure 103 Urolithiasis.

1. Kidney; 2. Concrement in the renal pelvis; 3. Renal pelvis.

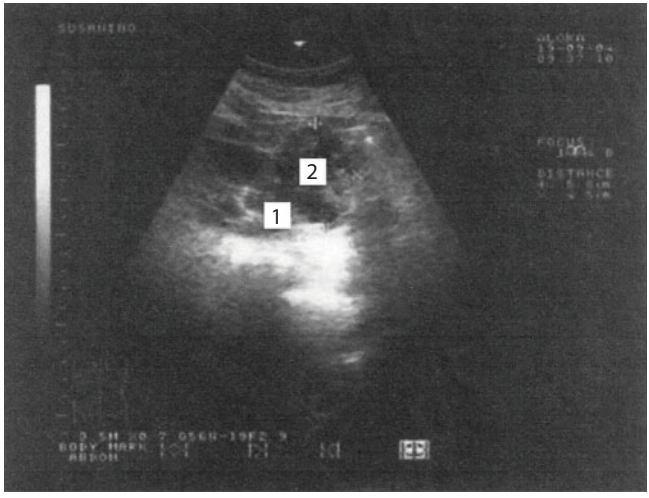

Figure 104 Renal tumor.

1. Kidney; 2. Renal neoplasm (tumor).

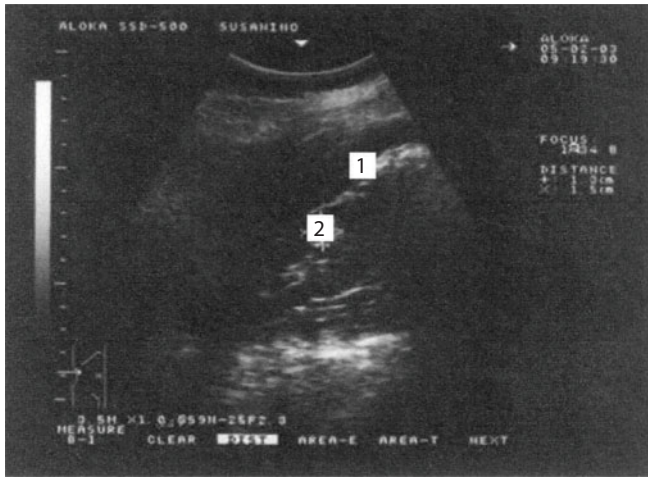

Figure 105 Renal hemangioma.

1. Kidney; 2. Hemangioma.

Topography and Pathotopography of the Pelvis

Topographical anatomy of the pelvic organs

The small pelvis is divided into three levels: upper, middle, and lower.

The upper pelvic area corresponds to the peritoneal sack descending to the small pelvis. It was given the name of cavum pelvis peritoneale. It contains the major part of the rectum and urinary bladder. In females, it also contains the uterus.

The middle pelvic area is located between the parietal peritoneum and the elevator muscle of the anus covered with the fascia diaphragmatis pelvis superior. In addition to the fat cellular tissue occupying this fissured space, it also contains the main blood and lymph vessels of the small pelvis, as well as the nerve trunks. This space was given the name cavum pelvis subperitoneale.

The lower area of the small pelvis contains the fossa ischiorectalis; it was given the name cavum pelvis subcutaneum. The cavum pelvis

subcutaneum is located between the skin cover and elevator muscle of the anus covered with the fascia diaphragmatis pelvis superior. It also contains terminal branches of the main arterial and nerve trunks.

Examination of the upper area of the small pelvis should be focused on the two lateral folds of peritoneum. These folds in males and females were given the names plicae rectovesicales and plicae rectouterinae, respectively. They contain unstriated muscles; in females, m. rectouterinus providing fixation of the uterus. Thus, below the folds the peritoneal cavity again becomes enlarged. In males, this cavity was given the name rectovesical pouch; in females, rectouterine pouch.

Topography of the female pelvis

The urinary bladder is situated in the anterior small pelvis. The anterior surface of the bladder is directed toward the pubic symphysis; posterior surface, toward the uterine cervix and top of the anterior wall of the vagina. The inferolateral segment of the bladder is adjacent to the elevator muscle of the anus. When full, the bladder reaches above the level of the symphysis, while its lateral surfaces touch the internal anal sphincter. Loose connective tissue, hypogastric plexus, lateral umbilical ligament, and round ligament of the uterus are located between the muscles and bladder wall.

The uterus is an unpaired muscular organ located in the small pelvis between the bladder at the front and the rectum at the back. The uterus and the mesodesma are located transversally in the pelvis. The back of the mesodesma is attached to ovaries by the mesentery. The fallopian tubes, which are 10–12 cm long and narrow, connect the ovary to the uterus. They are located at the loose superior end of the mesodesma. The fallopian tubes are attached to the mesodesma by the mesentery.

The vagina connects the uterus with the pudenda. It is a tube, usually no longer than 10 cm, the top end of which embraces the uterine cervix. The vagina extends from the small pelvis to the vulvar slit passing through

the urogenital diaphragm. The superior part of the anterior vaginal wall is adjacent to the base of the bladder, being separated from it by a layer of loose cellular tissue. Below, it is connected to the urinary tract. The upper quarter of the posterior vaginal wall is covered by the peritoneum (Douglas pouch). Below, it is adjacent to the rectum, gradually separating from it at the perineum area.

Scanning along the linea alba provides imaging of the longitudinal cross-section of the abdominal cavity and pelvis. Images of contours of the bladder with its liquid content, uterus, vagina, rectum, and sacral bone, as well as an undifferentiated image of small intestine, are obtained. Skin, subcutaneous fat, fasciae, muscles, and peritoneum are seen in the echogram as an interlayer. The thickness of the interlayer depends on the subcutaneous fat thickness. The echogram of the bladder is triangular with distinct contours. Its size depends on the degree of filling.

Behind the bladder, a distinct echographic image of the uterus is obtained. It is pear-shaped in the case of longitudinal scanning; in transverse scans it is oval. Only the outer contour of the uterus is distinct in the image. The ultrasonic image of the uterus structure is represented by many point and linear echo signals.

The echography allows the uterus position in the small pelvis to be located. The left or right shift of the uterus with respect to the lateral pelvic walls, as well as the backward tilt of the uterus, can be detected.

Ultrasonic examination allows the uterine body length, its anteroposterior and transverse sizes, perimeter, area, and volume to be measured. Uterus size in non-pregnant women depends on a number of factors and varies over a wide range.

In healthy women of reproductive age, the mean length of the uterine body is 71 mm (60–80 mm), the antero-posterior size is 40 mm (36–44 mm), and the transverse size is 50 mm (46–60 mm). In parous women, these values are usually somewhat greater, especially after two to three labors.

Uterus cervix visualization depends on the degree of bladder filling and the uterus position in the female pelvis. Visualization sometimes fails to reveal the border between the cervix and the uterine body. Transvaginal ultrasound provides more distinct visualization of the vaginal portion of the cervix and vagina.

Ovaries can be more effectively visualized using transverse or sector scanning. The ovary echogram demonstrates an oval-shaped structure near the uterus. The acoustic structure of the uterus and ovaries is homogeneous.

Undistorted visualization of fallopian tubes is virtually impossible.

Behind the uterus and vagina, a segment of large intestine is visualized. Its imaging depends on the filling degree and the character of the content.

Use of ultrasound considerably increased the diagnostic capabilities. The first works on ultrasonic diagnosis in obstetrics and gynecology date back to the early 1960s.

Presently, the diagnostic equipment for ultrasonic examination provides high resolution, thereby facilitating diagnosis of complicated cases. Use of ultrasound led to a twofold increase in the accuracy of the diagnosis. This method of examination is fast, safe, and provides valuable diagnostic information.

Ultrasonic diagnosis is especially useful in obstetrics. Primarily, it is used to detect early intrauterine pregnancy. Pregnancy termination dangers, small-for-date fetus, various fetal abnormalities, placenta location, placental maturity grade, multiple pregnancy, and missed miscarriage can also be effectively diagnosed using this method.

The echographic symptom of the early pregnancy is the presence of the gestational sac in the uterine cavity. The gestational sac is a sphere with a thick wall in the upper uterine segment. The gestational sac grows as pregnancy develops. It becomes oval due to the increase in the longitudinal and transverse dimensions.

Ultrasonic diagnosis allows valuable information about congenital anomalies of internal genital organs, the presence or absence of internal genital organs, hysteromyoma, cysts and ovarian cysts, tumors and tumor-like neoplasms of uterine adnexa to be obtained.

Hysteromyoma. The echogram visualizes a magnified uterus with modified contours of the uterine body. The image contains spherical structures with increased acoustic density manifesting itself as a reduction in sharpness of the image of the posterior wall of the myomatous nodule. There is also no reflection from the structures situated behind it.

Ovarian cysts. The echographic visualization of the ovarian cysts is based on detection of the liquid content of the cyst formation. The main echographic symptoms of the ovarian cysts are large size, internal septa, parietal indurations, and highly dispersed heterogeneous internal echostructure.

Topography of male pelvis

The urinary bladder is situated in the anterior small pelvis. The anterior surface of the bladder is directed toward the pubic symphysis; the surface, toward the rectum. The inferolateral segment of the bladder is adjacent to the elevator muscle of the anus. When full, the bladder reaches above the level of the symphysis, while its lateral surfaces touch the internal anal sphincter. Loose connective tissue, hypogastric plexus, lateral umbilical ligament, and deferent duct are located between the muscles and bladder wall.

The anterior surface of the bladder is separated from the symphysis by prevesical cellular tissue. The posterior surface of the bladder is covered by the peritoneum, whereas at the bottom of the bladder it is separated from the rectum by retrovesical cellular tissue.

The prostate gland is located between the urogenital diaphragm and the base of the bladder. The posterior wall of the prostate gland is

adjacent to the rectum. The base of the prostate gland is attached to the bladder neck. Inferior segments of spermatocysts (paired 6–7 cm long structures consisting of a body and a neck) are adjacent to a small segment of the prostate gland base.

A 2.5 cm long segment of the urinary tract (pars prostatica) emerges from the bladder and passes through the prostate gland. Then, the urinary tract passes through the urogenital diaphragm (pars membranacea, 1 cm long) and through the penis, where it is surrounded by the cavernous bodies (pars spongiosa).

Ultrasonic topographical anatomy of male pelvis

An empty bladder is not detected in echograms. Therefore, sufficient bladder filling is a necessary condition for its ultrasonic examination. In the norm, the intact bladder is visualized in cross-section scanograms as a barrel-shaped structure, while in longitudinal scanograms it is seen as a distinct ovoid structure with smooth surface, echonegative, and free of internal structures. Behind the bladder the echographic image shows the prostate gland and, in some cases, the rectosigmoid.

The prostate gland is situated in the inferoanterior third of the small pelvis, under the bladder, between the pubic symphysis and rectum. It is chestnut-shaped. Its anterior surface is slightly concave and directed toward symphysis; its posterior convex surface, toward the rectum. The echographically non-modified prostate gland is visualized in longitudinal scans as an oval structure, whereas in cross-section scans it is seen as a symmetric round structure with a smooth contour and a distinct capsule. The prostate gland tissue is sufficiently homogeneous; in most cases it is represented by many small-sized point or linear structures.

Prostate gland cancer has specific echographic features. Asymmetry of the gland, deformation of contours, and thinning of some segments of the capsule are observed. The inner structure of the gland

becomes heterogeneous. In gland parenchyma, segments with lower echogenicity and higher homogeneity of structure are observed. In case of malignant invasion into adjacent tissues, the capsule integrity is broken.

Chronic prostatitis, if not exacerbated, does not lead to changes in the normal echographic pattern of the gland. In some cases, the contour is modified. The echogram visualizes multiple (in most cases) prostatic calculi often located in both lateral lobes. In some cases, the prostatic calculi form groups detected as distinct echopositive structures.

Urolithiasis. Cystic calculi and intramural ureteral calculi are successfully diagnosed using ultrasonic examination. In the echogram, the calculi are imaged as distinctly contoured individual or multiple echopositive structures located at the posterior wall of the bladder or in the ureter.

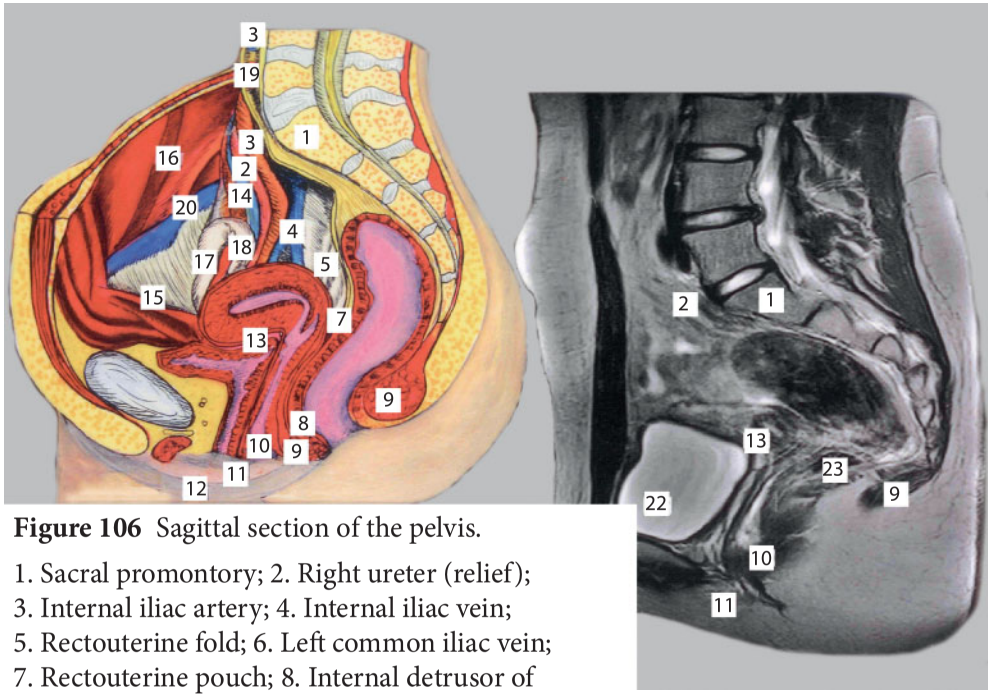

Figure 106 Sagittal section of the pelvis.

1. Sacral promontory; 2. Right ureter (relief); 3. Internal iliac artery; 4. Internal iliac vein; 5. Rectouterine fold; 6. Left common iliac vein; 7. Rectouterine pouch; 8. Internal detrusor of anal canal; 9. External detrusor of rectum; 10. Vagina; 11. Labia minora; 12. Labia majora; 13. Uterovesical pouch; 14. Blood vessels of the ovary (in suspensory ligament of ovary); 15. Round ligament of uterus; 16. Internal iliac artery; 17. Fallopian tube; 18. Ovary; 19. Right common iliac artery; 20. External iliac vein; 22. Urinary bladder; 23. Rectum.

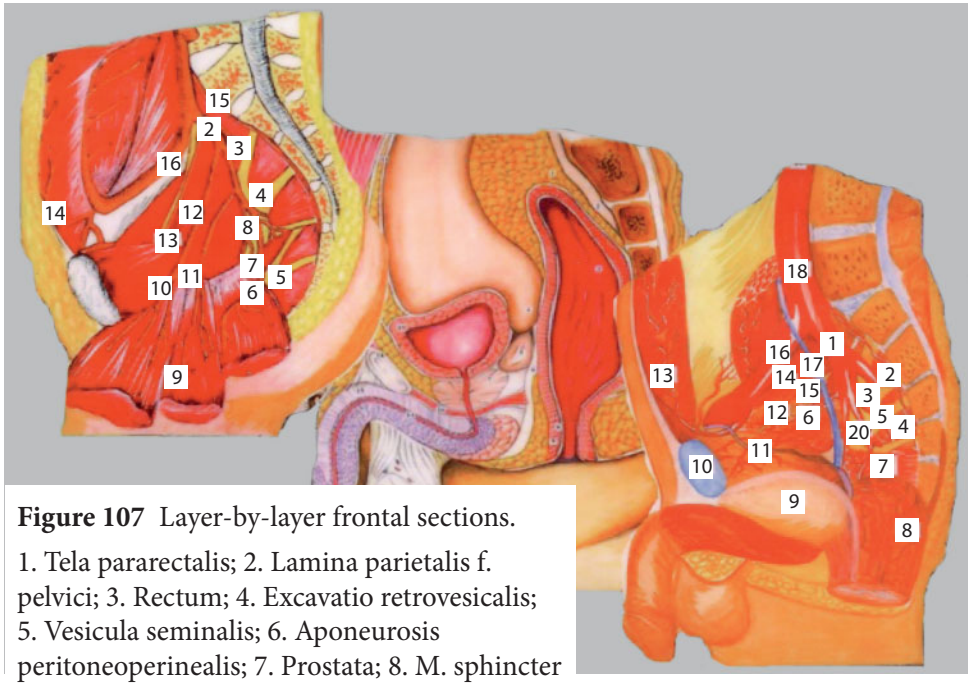

Figure 107 Layer-by-layer frontal sections.

1. Tela pararectalis; 2. Lamina parietalis f. pelvici; 3. Rectum; 4. Excavatio retrovesicalis; 5. Vesicula seminalis; 6. Aponeurosis peritoneoperinealis; 7. Prostata; 8. M. sphincter ani internus; 9. M. sphincter ani externus; 10. Testis; 11. Peritoneum; 12. M. rectus abdominis scu f. transversa; 13. F. prevesicalis; 14. Urethra; 15. Corpus cavernosum penis; 16. Diaphragma urogenitale; 17. Tela preperitoneale; 18. Symphisis; 19. Vesica urinaria; 20. Tela prevesicalis.

1. A. iliaca communis; 2. A. iliaca interna; 3. A. glutea superior; 4. Plexus sacralis; 5. Plexus pudendus; 6. A. glutea interior; 7. A. rectalis media; 8. A. pudenda interna; 9. A. uterine; 10. A. cyctica; 11. Margo f. pelvina; 12. M. piriformis; 13. A. et nervi obturatorii; 14. A. epigastnca inferior; 15. A. sacralis externa; 16. A. iliaca externa.

1. A. iliaca interna; 2. A. sacralis mediana; 3. Plexus sacralis; 4. M. piriformis; 5. A. glutea inferior; 6. A. umbilicalis; 7. M. levator ani; 8. Rectum; 9. Vesica urinaria; 10. Os pubis; 11. Ductus deferens; 12. Os ilium; 13. A. epigastrica inferior; 14. M. iliacus; 15. N. obturatorius; 16. A. iliaca externa; 17. Ureter; 18. A. iliaca communis; 19. Aorta abdominalis; 20. A. pudenda interna.

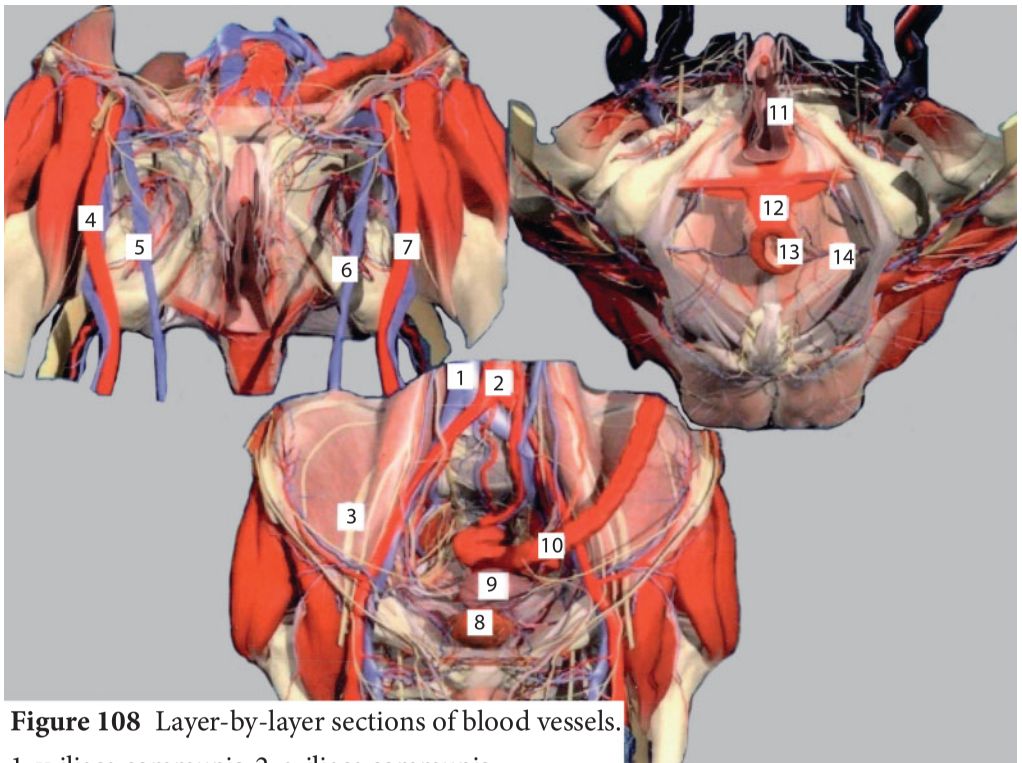

Figure 108 Layer-by-layer sections of blood vessels.

1. v. iliaca communis; 2. a. iliaca communis;
3. n. ischiadicus; 4. a. iliaca externa dextra; 5. v. iliaca externa dextra; 6. v. iliaca externa sinistra;
7. a. iliaca externa sinistra; 8. Vesica urinaria; 9. Uterus; 10. Colon sigmoideum; 11. Vagina;
12. Centrum tendinous perinea; 13. m. sphincter ani externus; 14. v. et n. rectales inferiores.

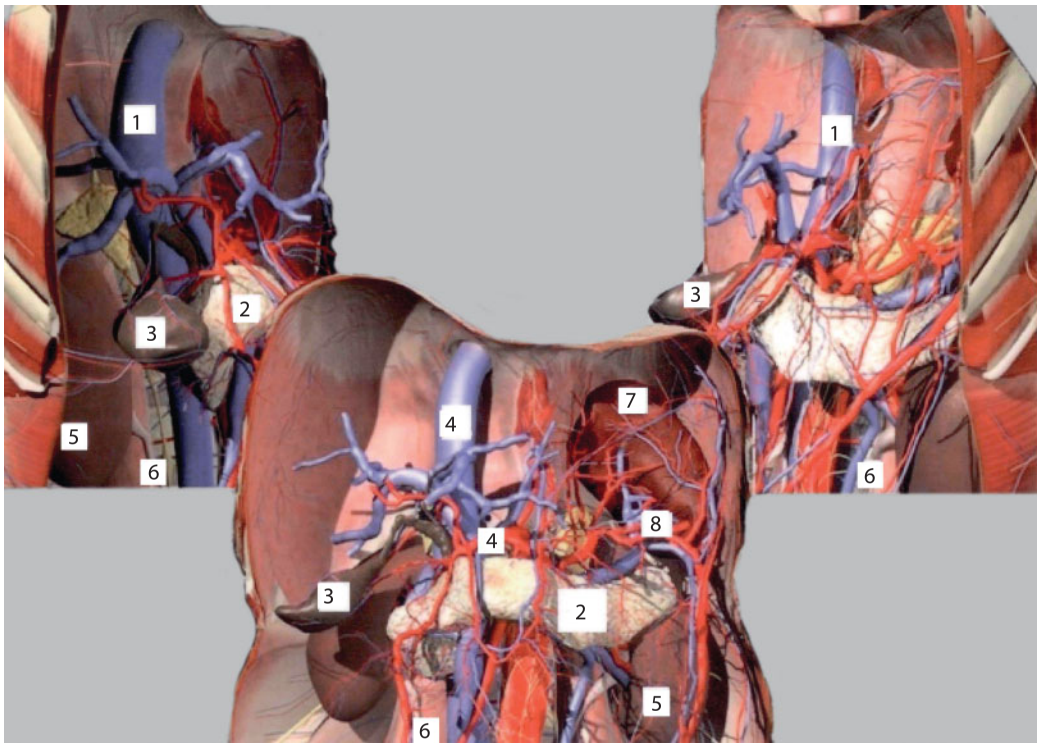

Figure 109 Frontal sections.

1. v. cava inferior; 2. Pancreas; 3. Vesica fellea; 4. a. mesenterica superior; 5. Ren; 6. Ureter; 7. Lien; 8. a. et v. lienalis.

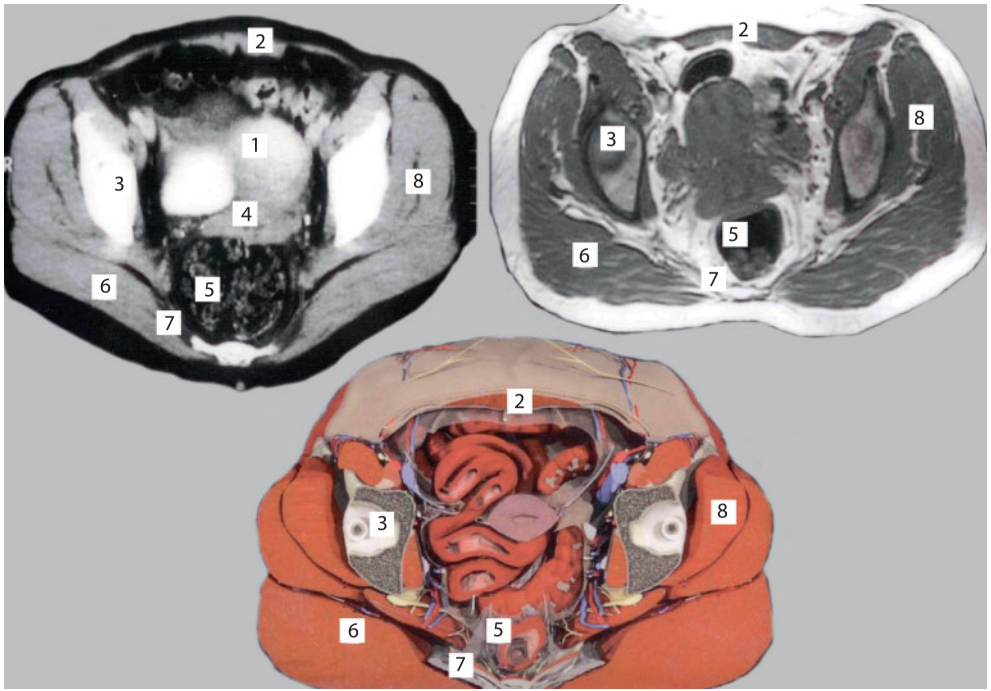

Figure 110 Cross-section of the pelvis.

1. Urinary bladder; 2. Rectus abdominis; 3. Cotyloid cavity; 4. Uterus; 5. Rectum; 6. Gluteus maximus; 7. Sacrospinal ligament; 8. Gluteus medius.

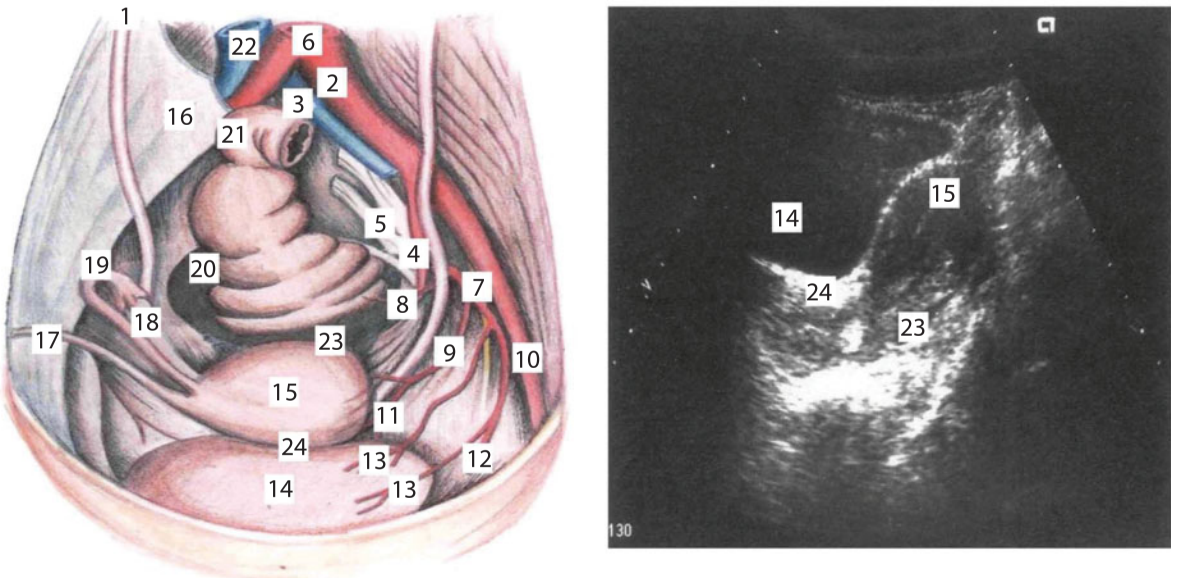

Figure 111 Topography of the female pelvis.

1. Uterus; 2. Common iliac artery; 3. Common iliac vein; 4. Internal iliac artery; 5. Sacral plexus; 6. Aorta; 7. Obturator nerve; 8. Middle rectal artery; 9. Uterine artery; 10. External iliac artery; 11. Vaginal artery; 12. Umbilical artery; 13. Urinary bladder arteries; 14. Urinary bladder; 15. Uterus; 16. Peritoneum; 17. Round ligament of uterus; 18. Ovary; 19. Fallopian tube; 20. Uterosacral ligament; 21. Rectum; 22. Inferior vena cava; 23. Rectouterine pouch; 24. Uterovesical pouch.

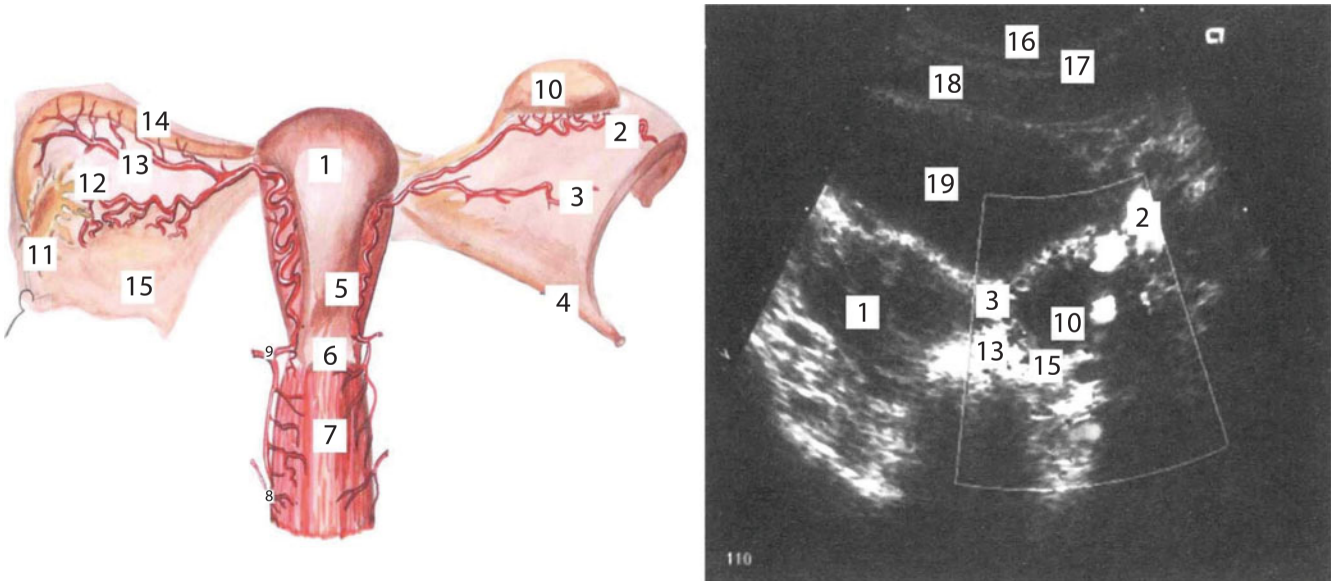

Figure 112 Blood supply to internal female genital organs.

1. Uterine fundus; 2. Ovarian artery; 3. Ovarian branches of uterine artery; 4. Round ligament of uterus; 5. Uterine body; 6. Uterine cervix; 7. Vagina; 8. Vaginal branches of uterine artery; 9. Uterine artery; 10. Ovary; 11. Infundibulum of uterine tube with fimbria; 12. Mesosalpinx; 13. Tubal branch of uterine artery; 14. Fallopian tube; 15. Mesovarian ligament; 16. Skin; 17. Subcutaneous fat; 18. Rectus abdominis; 19. Urinary bladder.

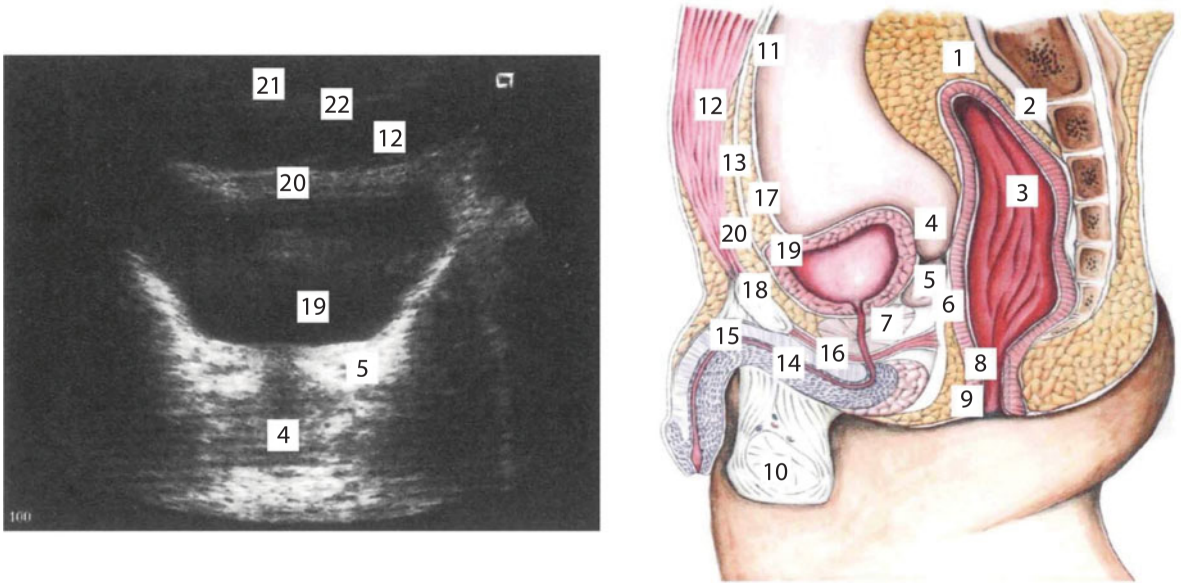

Figure 113 Sagittal cross-section of male pelvis.

1. Paraproctium; 2. Parietal leaf of pelvic fascia; 3. Rectum; 4. Rectovesical recess; 5. Spermatocyst; 6. Denonvilliers aponeurosis; 7. Prostate gland; 8. Internal detrusor of anal canal; 9. External detrusor of anal canal; 10. Testis; 11. Peritoneum; 12. Rectus abdominis and transverse fascia; 13. Prevesical fascia; 14. Urinary tract; 15. Cavernous body of penis; 16. Urogenital diaphragm; 17. Preperitoneal cellular tissue; 18. Symphysis; 19. Urinary bladder; 20. Prevesical cellular tissue; 21. Skin; 22. Subcutaneous fat.

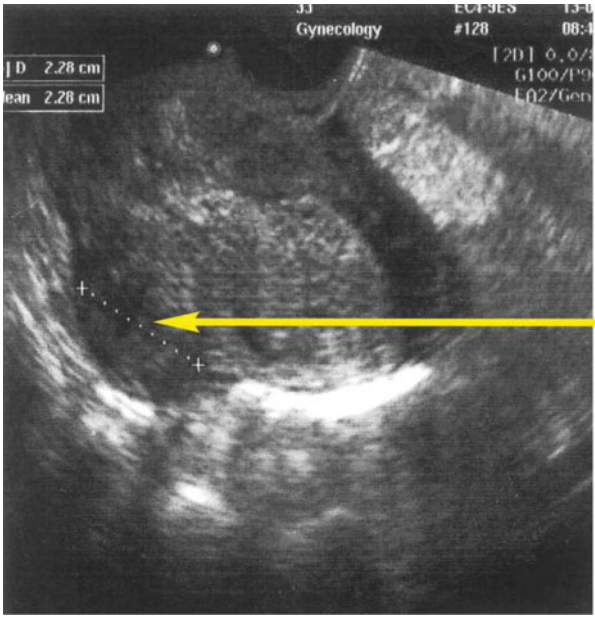

Figure 114 Hysteromyoma.

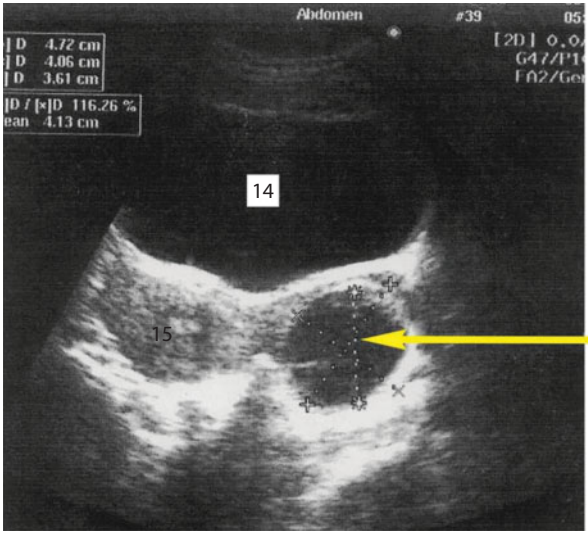

Figure 115 Left ovarian cyst.

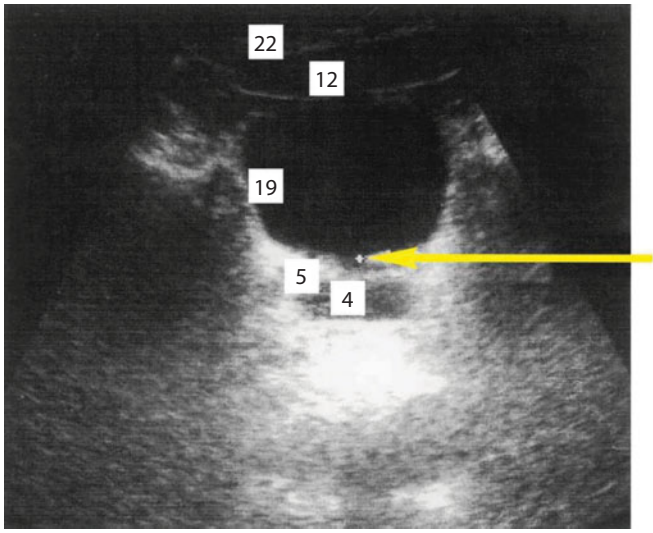

Figure 116 Ureteral opening calculus.

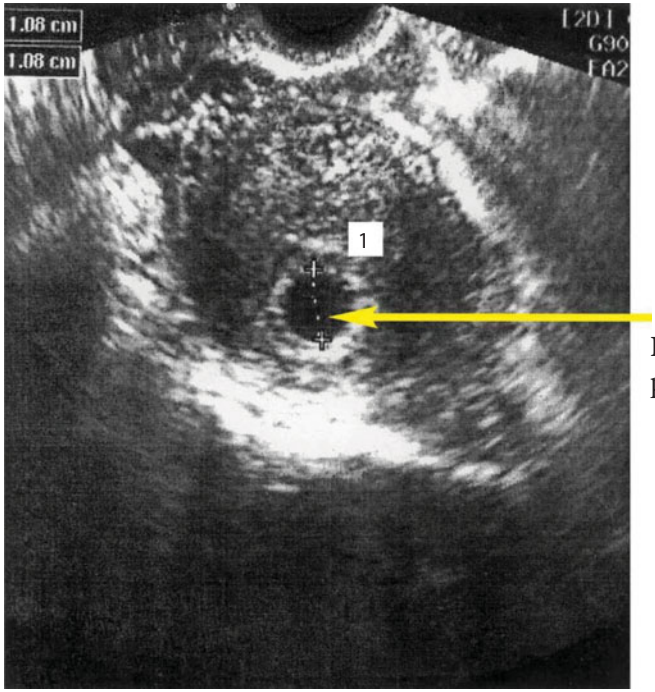

Figure 117 6 weeks pregnancy.

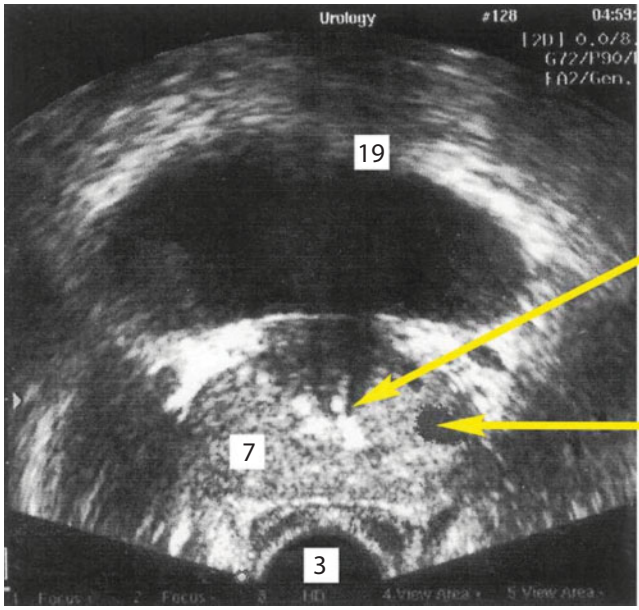

Figure 118 Calcification.

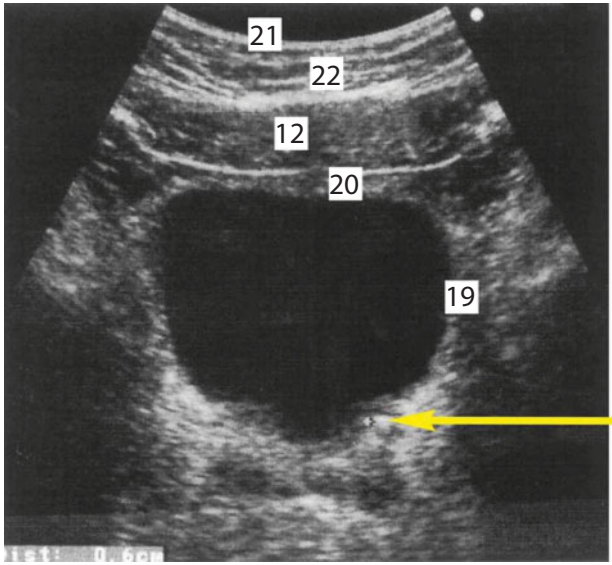

Figure 119 Left ureteral calculus.

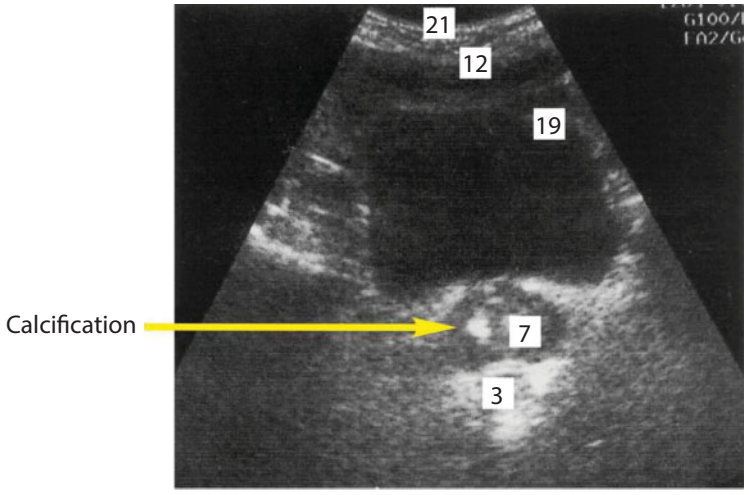

Figure 120 Chronic prostatitis.

Topography and Pathotopography of Lower Extremity

Presently, ultrasonic scanning is the most informative up-to-date method for examination of joints. This is due to the continuous progress in the technology, wide accessibility, and lower cost as compared to computed tomography and magnetic resonance imaging.

The diagnostic capacity of ultrasonic examination of the knee joint is the subject of an ongoing discussion. Ultrasonic methods of diagnostic examination of the knee joint cannot completely replace such methods as MRI and standard X-ray. Nevertheless, ultrasonic diagnosis has certain advantages. The most substantial advantage is the ability to test soft tissues of the knee joint, including ligaments, tendons, connective tissue elements, subcutaneous fat, and neurovascular bundles.

The trial was implemented using the Medison-128 ultrasonic scanner with a 7.5 MHz line scan sensor. The standard method focusing on examination of bursae and tendinoligamentous apparatus in the anterior and posterior projections was used. A total of 1,416 patients have

been tested: 800 males (56.4%) and 616 females (43.5%). The average age of the patients was 43.6 years.

Four standard access methods were used to provide ultrasonic visualization of all elements of the joint: lateral, medial, anterior, and posterior. In ultrasonic visualization of the knee joint, the anatomy of the joint was considered. Anterior access provided visualization of the tendon of the quadriceps muscle of the thigh, anterior recess, knee cap, suprapatellar bursa, patellar ligament, infrapatellar bursa, and bursa of the knee fat pad. Tendons of the quadriceps muscle of the thigh do not have synovial sheaths; at the edge they are surrounded by a hyperechogenic stripe, while at the distal zone, behind the tendon of the quadriceps muscle of the thigh, the suprapatellar bursa is situated. In the norm, the suprapatellar bursa may contain a small amount of liquid. The panoramic scanning mode provides visualization of all four muscle bundles comprising the quadriceps muscle of the thigh.

Medial access provides visualization of medial collateral ligament, medial meniscus body, and medial joint space of the knee. The state of joint space, contours of the femoral and shin bones, the thickness and the state of hyaline cartilage, and presence of gaps in joint cavity are estimated. The epiarticular space contains fibers of medial lateral ligament, which starts from the proximal medial femoral condyle and is attached to the proximal metaphysis of the shin bone. The fibers of the anterior cruciate ligament are visualized only partially.

Lateral access provides visualization of the distal segment of fascia lata, the tendon of the popliteus muscle, the fibular collateral ligament, the distal part of the tendon of the biceps muscle of the thigh, the lateral meniscus body, and the lateral joint space. Cranial scanning provides visualization of the fascia lata fibers. Tendon fibers are attached to the bone near the Gerdy's tubercle on the anterolateral surface of the tibial bone. Fixation of the sensor at the head of the fibula and rotation of the proximal end of the sensor toward the bottom provides detection of the tendon of the lateral head of the biceps muscle of the thigh.

Posterior access provides visualization of the neurovascular bundle of popliteal fossa, medial and lateral heads of the gastrocnemius muscle, the distal part of fibers of the tendon of the semimembranosus muscle, the posterior horn of the medial meniscus, the posterior horn of the lateral meniscus, and the posterior cruciate ligament. The neurovascular bundle is shifted in a lateral direction in the popliteal fossa. The popliteal artery is located behind the vein. The muscular fascicles of the popliteus muscle are visualized below. Panoramic scanning using energy mapping provides visualization of the popliteal artery. A small bursa with collum of Baker's cyst is located between the tendon of the semimembranosus muscle and the medial head of the gastrocnemius muscle. To visualize this bursa, transverse scanning should be performed in the region of the posterior surface of the medial condyle of the femur covered with hyaline cartilage, tendons of the semimembranosus muscle, and fibers of the gastrocnemius muscle. Longitudinal scanning of the popliteal fossa provides visualization of the posterior horn of the lateral meniscus, as well as the posterior cruciate ligament. Posterior and anterior cruciate ligaments are visualized only partially. Their fibers are hypoechogenic because of the anisotropy effect. The posterior access also provides visualization of fibular nerve, which diverges from the lateral part of the sciatic nerve in the distal femur, passes down laterally along the distal tendon of the biceps femoris, reaches the popliteal fossa, and turns around the head of the fibular bone toward the anterior surface of the shin.

Specific anatomical features and functional loads of the knee joint increase the probability of its overstrain, trauma, and development of various diseases. Even insignificant dysfunction of the knee joint leads to substantial discomfort and impairment of work capability. More significant dysfunctions can lead to disability.

Ultrasonic examination provides detection of changes in bone structure at an early stage, which cannot be detected by X-ray. The main features of the pathotopographic ultrasonic anatomy of deforming arthrosis are heterogeneous thinning of hyaline cartilage, irregular contours of

the femoral and shin bones, marginal osteophytes, narrowing of joint space and prolapse of menisci. The presence of hyperechogenic marginal osteophytes in patients with normal values of the joint space size and hyaline cartilage thickness is typical of the early stage of the disease. The progress of the disease results in formation of marginal osteophytes with acoustic shadow, joint space narrowing and pronounced thinning of the hyaline cartilage. Further development of the disease leads to the hyaline cartilage thinning to 1 mm, formation of rough osteophytes, and prolapse of menisci to a third of their width. At the stage of pronounced pathological changes, complete prolapse of menisci, intraarticular deformation, disappearance of joint space, and formation of rough massive osteophytes at the edges of the articular surface are observed.

Knee joint injuries are often accompanied by internal bleeding in the joint. Hemorrhagic effusion observed two hours after injury may be indicative of disruption of lateral or cruciate ligaments, meniscus disruption, knee cap dislocation, or intra-articular fracture of the femoral condyle. The amount of blood in the knee joint space caused by hemarthrosis may vary. Presence of blood in the joint stimulates production of synovial fluid, which leads to further extension of bursa and capsule of knee joint. The greater the amount of fluid in the joint, the more severe is the pain. Fluid in the joint is more effectively detected using medial and lateral access. In patients with fluid in joints pathotopographical anatomy manifests itself as non-echogenic space in a number of synovial bursae. Baker's cyst is one of the most frequent pathologies in athletes. Usually, such cysts are asymptomatic and reveal themselves during ultrasonic or clinical examination. Distension of the bursa located between the tendons of the semimembranosus muscle and the gastrocnemius muscle acts as substrate for this type of cyst. Baker's cyst is differentially diagnosed using visualization of the collum of cyst connected to the knee joint cavity at the medial part of the popliteal fossa between the medial head of the gastrocnemius muscle and the tendon of the semimembranosus muscle. The cyst content is variable: recent cysts are non-echogenic, whereas long-standing cysts have heterogeneous content. In recent Baker's cysts the content is liquid,

whereas in long-standing cysts it is jellylike. The inflammation of surrounding tissues is manifested as vascularization, which is detected in the energy mapping mode. Rupture of the Baker's cyst is diagnosed as the presence of a typical sharp edge and a fluid stripe along fibers of the tendon of the gastrocnemius muscle. Rupture more typically occurs at the bottom of the cyst. The panoramic scanning mode provides complete visualization of the cyst.

Optometry was implemented by the Seagal method using the Seagal hemodynamics monitoring device. The sensitive element consists of two AL 107V LEDs and the FKD-155 photodetector mounted in a sealed cylindrical case, which is connected by cable to a chart recorder. The transrectal examination was implemented using a special probe. ELKAR-6 or EK1T-03M electrocardiographs with magnification × 10 or × 20 mm/mV were used as recorders. The chart recording rate was 5 mm/sec. The system was calibrated using an optical method. The useful signal was obtained using radiation in a broad range of spectral and power characteristics. The wide range of sensitivity of photodetectors and the relative positioning of the optocoupler elements were also important. The duration of a single session of detection of functional parameters was 10–30 sec. The optical calibration allowed the clinical parameters to be compared with each other. The transillumination hemomotorodynamics method is based on monitoring of variation of the pulsation and non-pulsation levels of the optical density of blood flow.

The optical density at the normal and pathological areas of the organ was measured during the tests together with pulse characteristics. The optometry was carried out by applying the optocoupler to the zone of interest. During this procedure the patient's breath should be held. In the norm, the optical density in the bursa of the lateral recess of the knee joint was 40–45 mA, while in the deep suprapatellar bursa it was 45 mA; amplitude of pulse oscillations (APO), 15–20 mm. In patients with rheumatoid arthritis, the optical density in the bursa of the lateral recess reached 53 mA; APO, 12–18 mm.

Further development of the ultrasonic and transillumination optical monitoring procedures can be important for the clinical purpose of detection of specific pathological symptoms, determination of the character of morphological disorders, elaboration of the tactics of surgery under monitoring, and development of new methods of treatment.

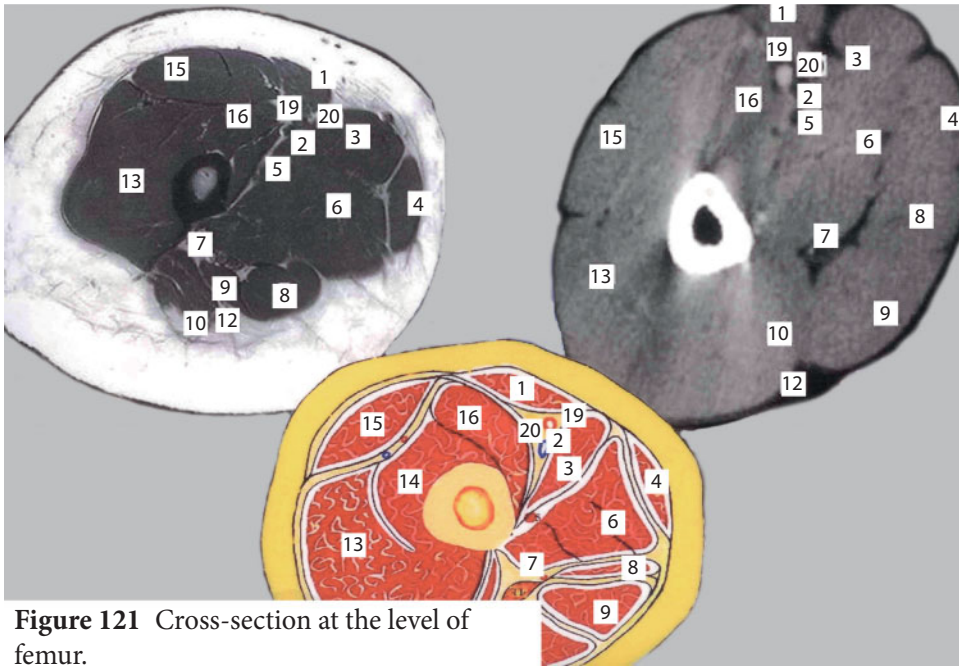

Figure 121 Cross-section at the level of femur.

1. Tailor muscle; 2. Internal intermuscular septum and femoral vessels; 3. Long adductor muscle; 4. Gracilis muscle; 5. Perforating artery; 6. Great adductor muscle; 7. Posterior intermuscular septum; 8. Semimembranosus muscle; 9. Semitendinous muscle; 10. Biceps; 11. Sciatic nerve; 12. External intermuscular septum; 13. External vastus muscle; 14. Medial vastus muscle; 15. Rectus muscle of thigh; 16. Internal vastus muscle; 19. Adductor canal; 20. Saphenous nerve.

Figure 122 Cross-section at the level of shin bone.

1. Shin bone; 2. Tibial nerve; 3. Long flexor muscle of toes; 4. Long saphenous vein; 5. Crural fascia; 6. Posterior tibial arteries and veins; 7. Tendons of plantar muscle; 8. Medial head of gastrocnemius muscle; 9. Salens muscle; 10. Small saphenous vein; 11. Lateral head of gastrocnemius muscle; 12. Flexor hallucis longus; 13. Posterior tibial muscle; 14. Posterior intermuscular septum; 15. Fibular bone; 16. Peroneus longus; 17. Anterior intermuscular fibular septum; 18. Long extensor muscle of toes; 19. Interosseous membrane; 20. Anterior tibial arteries and veins; 21. Anterior tibial muscle.

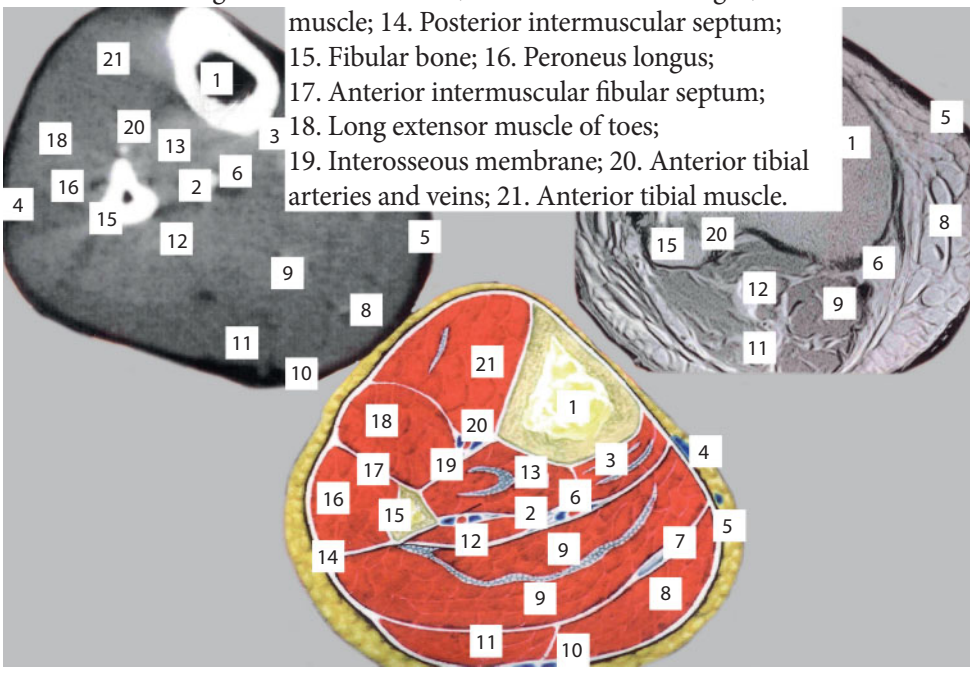

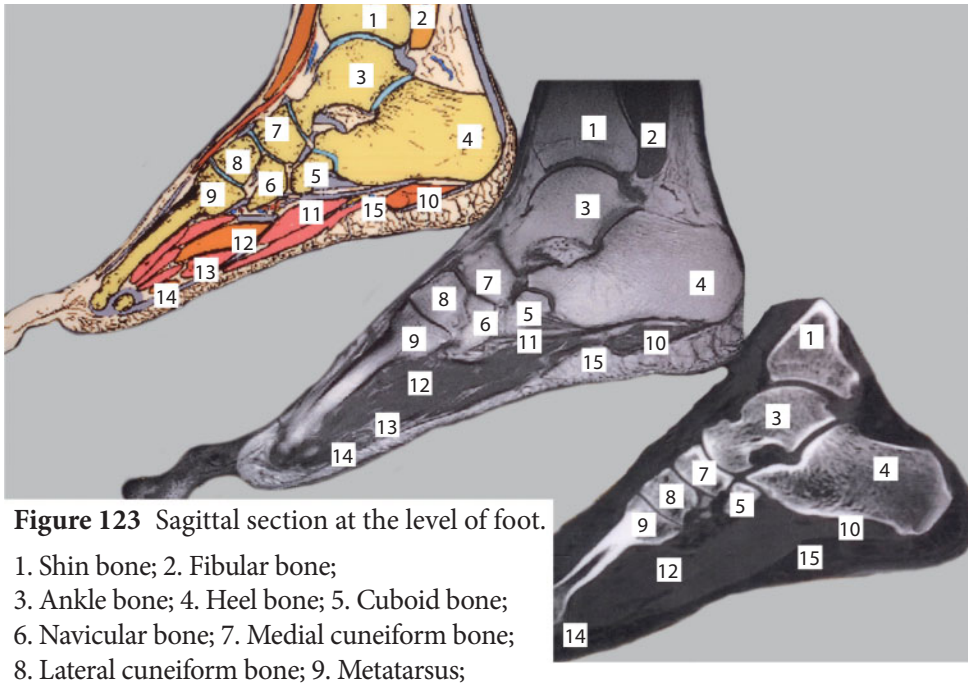

Figure 123 Sagittal section at the level of foot.

1. Shin bone; 2. Fibular bone; 3. Ankle bone; 4. Heel bone; 5. Cuboid bone; 6. Navicular bone; 7. Medial cuneiform bone; 8. Lateral cuneiform bone; 9. Metatarsus; 10. Abductor muscle of little toe; 11. Short flexor muscle of toes; 12. Adductor muscle of great toe (oblique head); 13. Lumbrical muscle; 14. Adductor muscle of great toe (transverse head); 15. Lateral nerve, artery; and vein of foot.

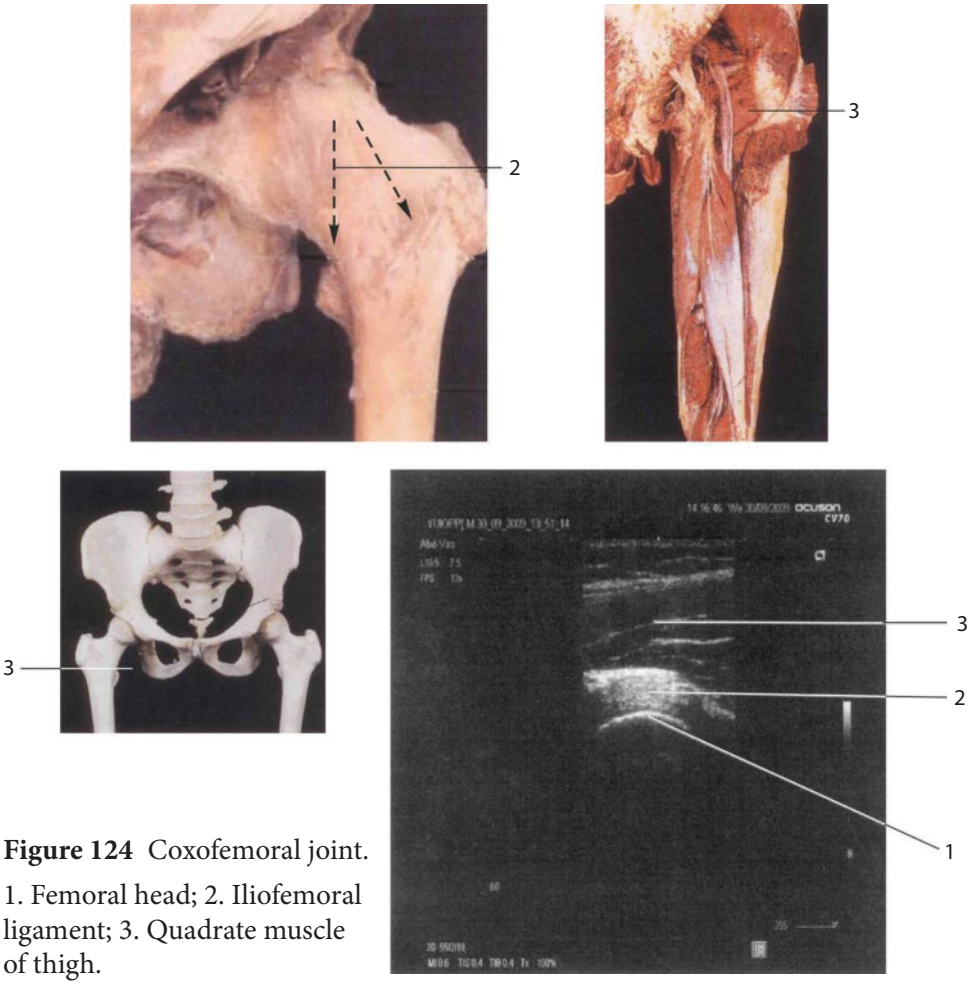

Figure 124 Coxofemoral joint.

1. Femoral head; 2. Iliofemoral ligament; 3. Quadrate muscle of thigh.

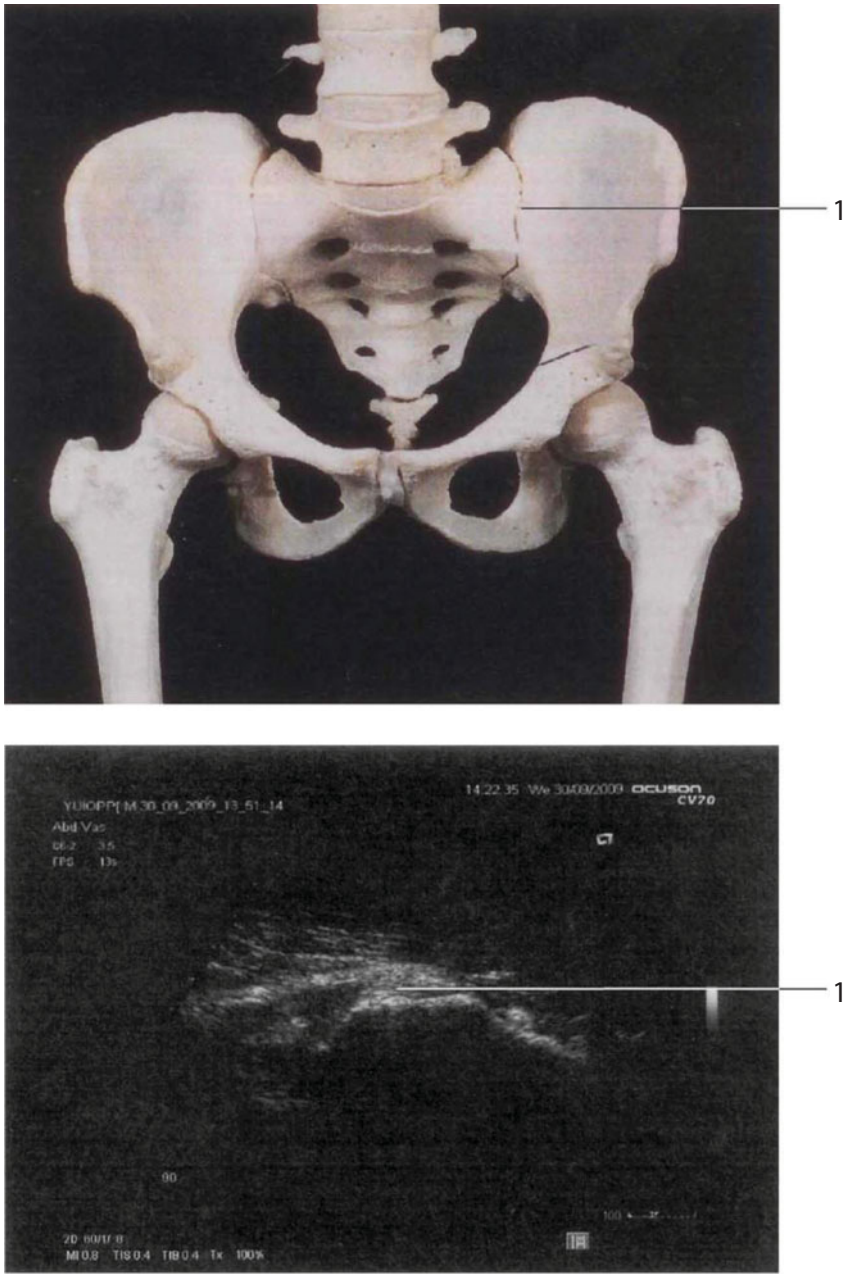

Figure 125 Sacroiliac joint.

1. Sacroiliac joint.

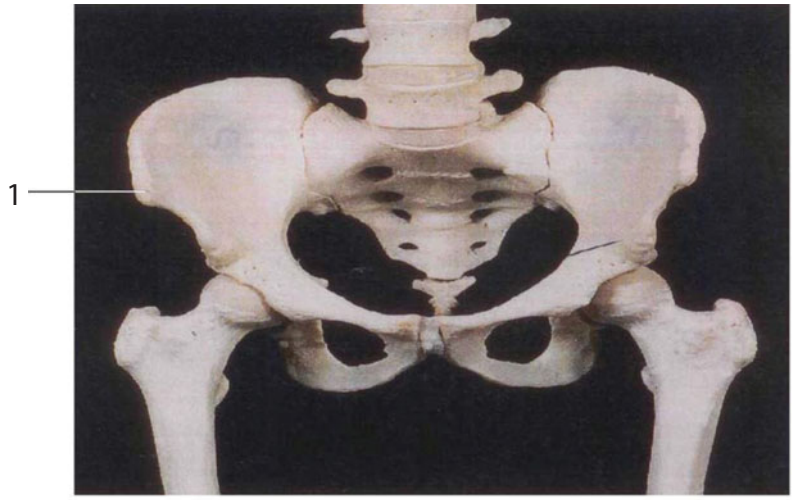

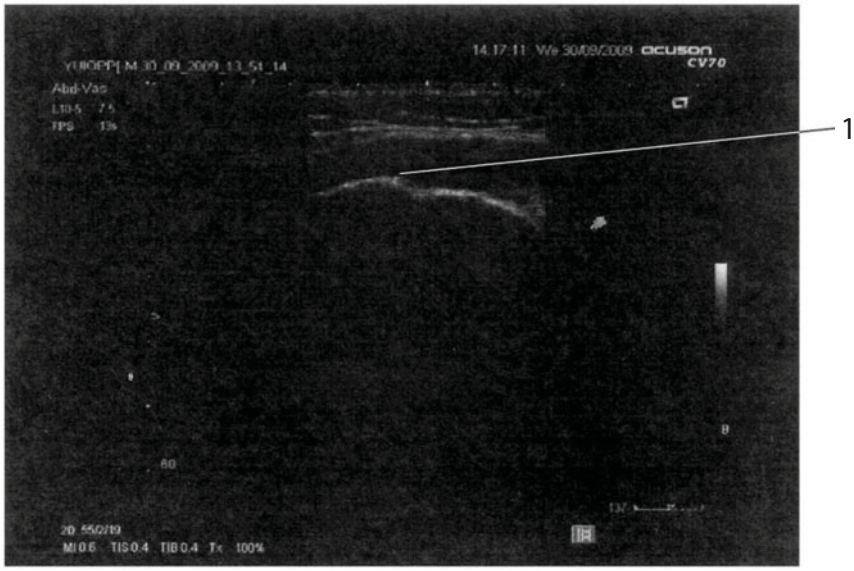

Figure 126 Anterior superior iliac bone.

1. Anterior superior iliac bone.

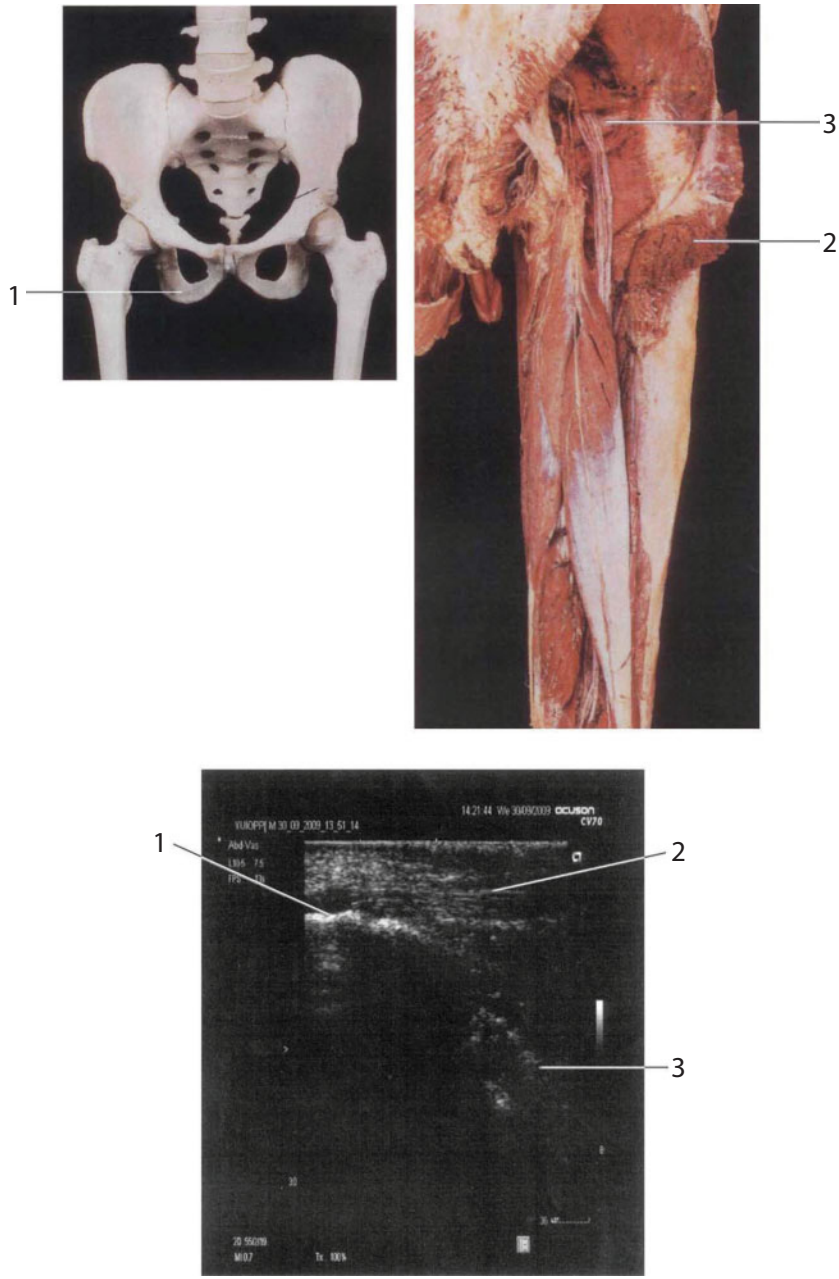

Figure 127 Femoral muscles.

1. Ischial bone; 2. Gluteus maximus muscle; 3. Internal occlusive muscle.

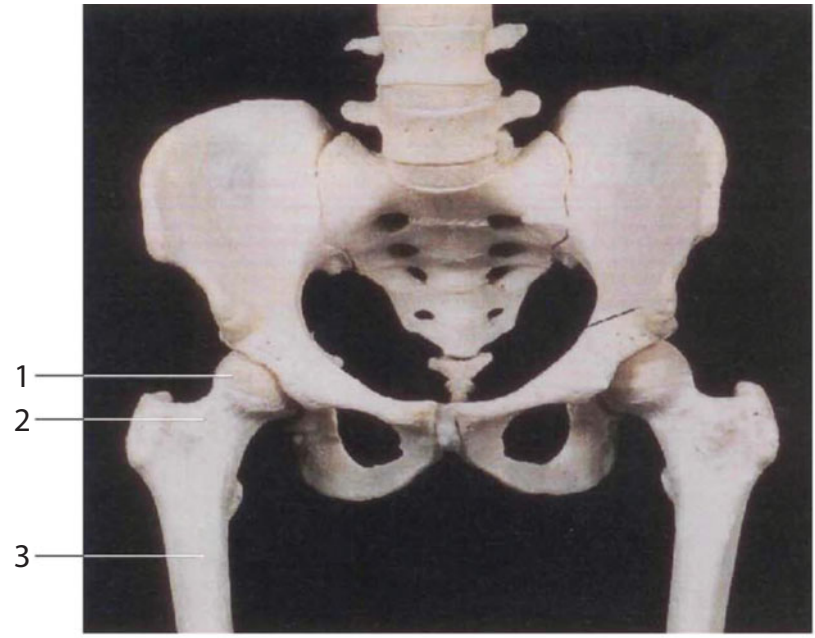

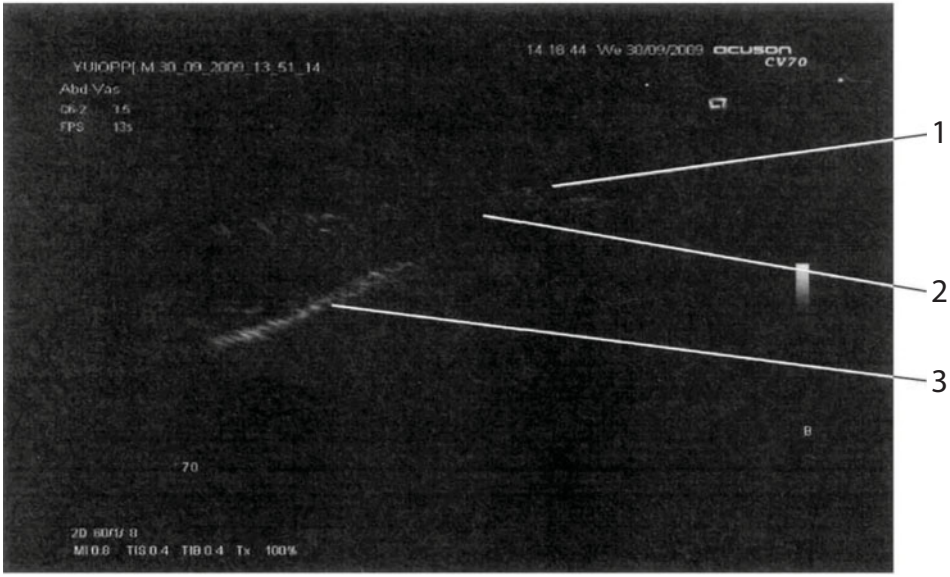

Figure 128 Femoral bone.

1. Femoral head; 2. Femoral neck; 3. Femoral bone.

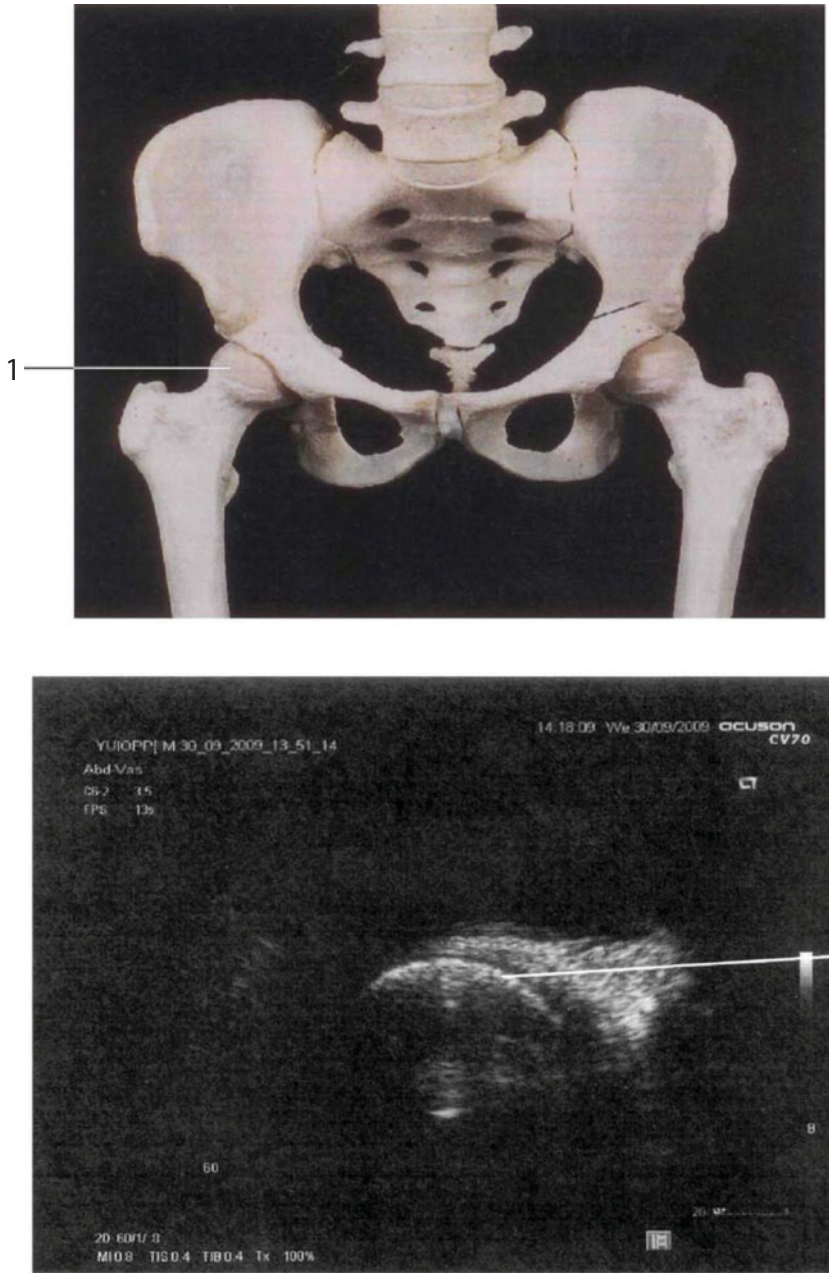

Figure 129 Femoral head.

1. Femoral head.

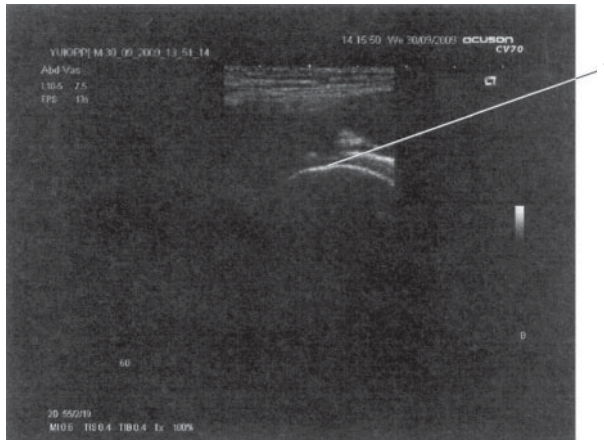

Figure 130 Femoral head.

1. Femoral head.

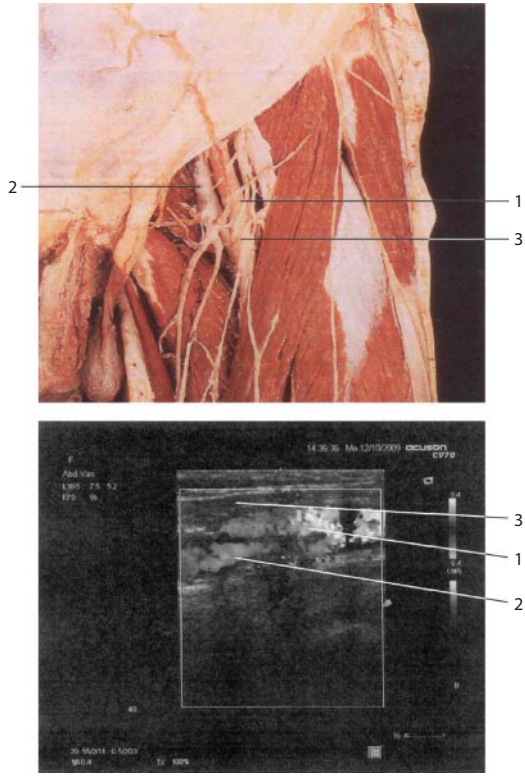

Figure 131 Femoral artery. Femoral vein.

1. Femoral artery; 2. Femoral vein; 3. Tailor muscle.

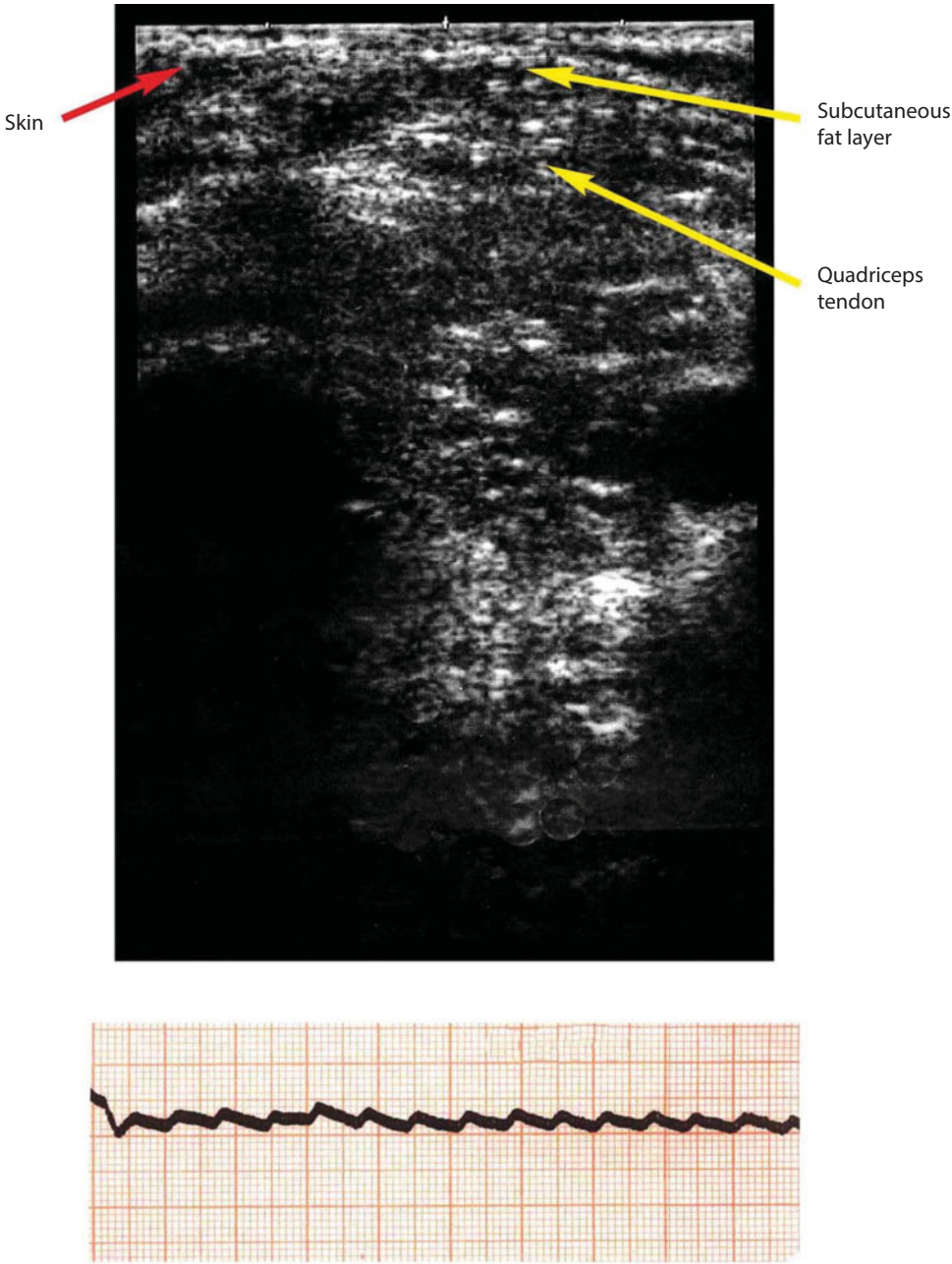

Figure 132 Suprapatellar pouch.

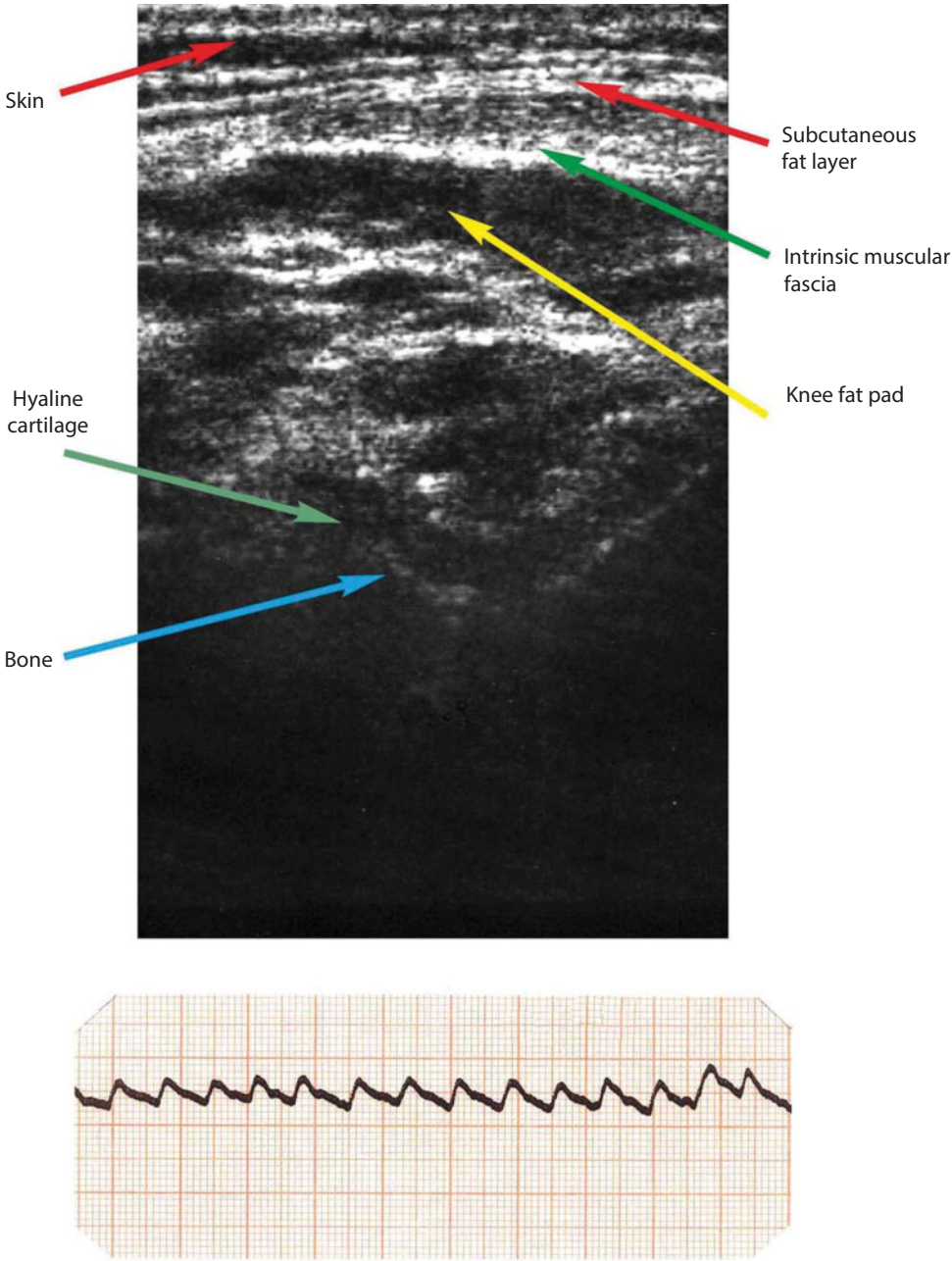

Figure 133 Infrapatellar recess.

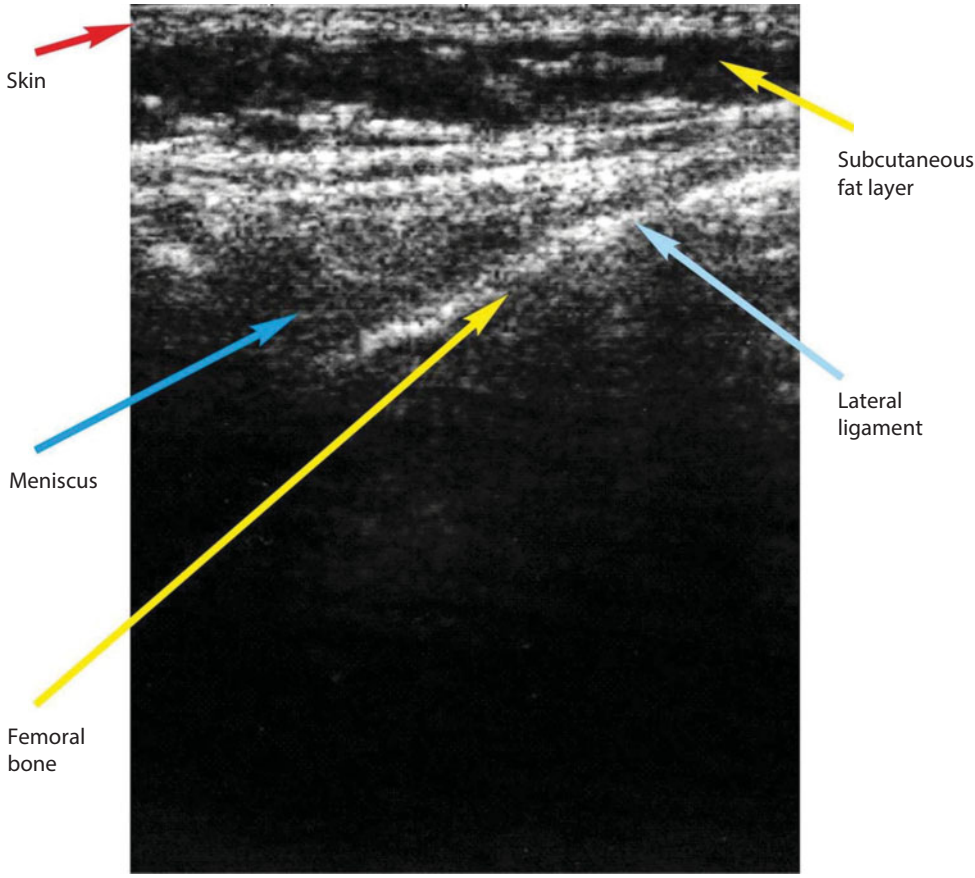

Figure 134 Lateral recess.

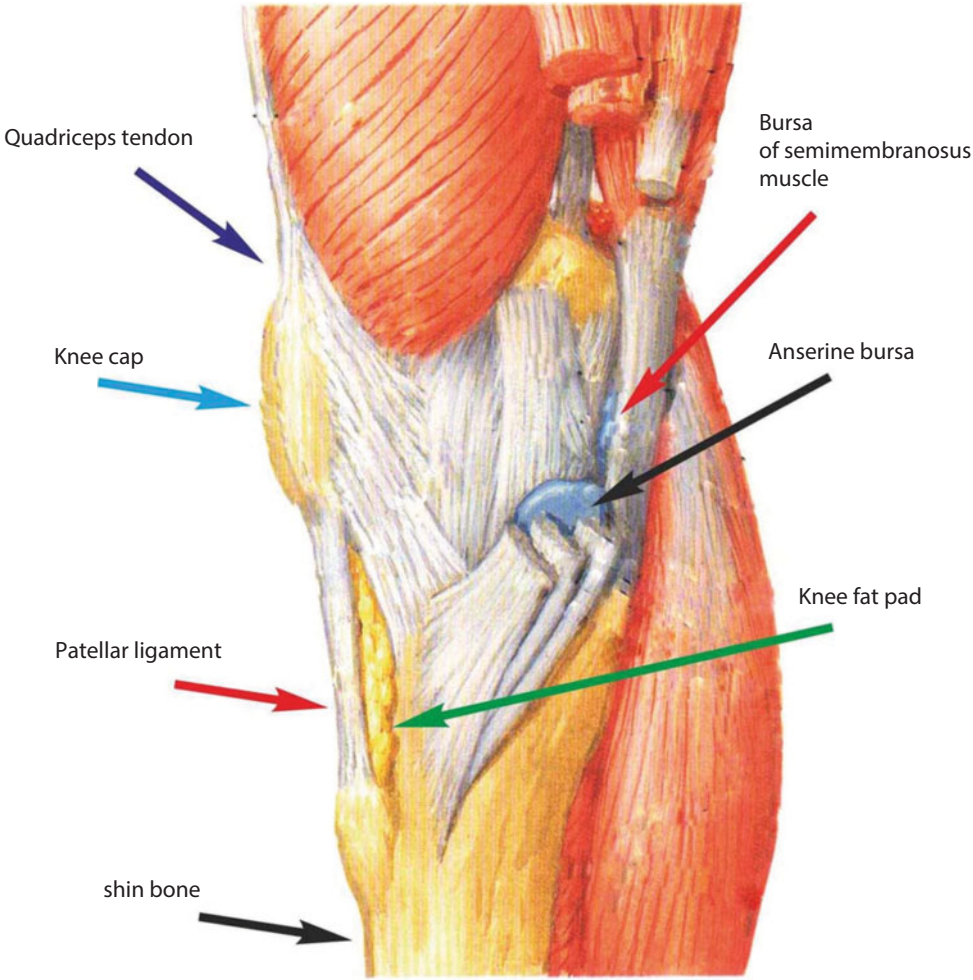

Figure 135 Knee joint. Medial view.

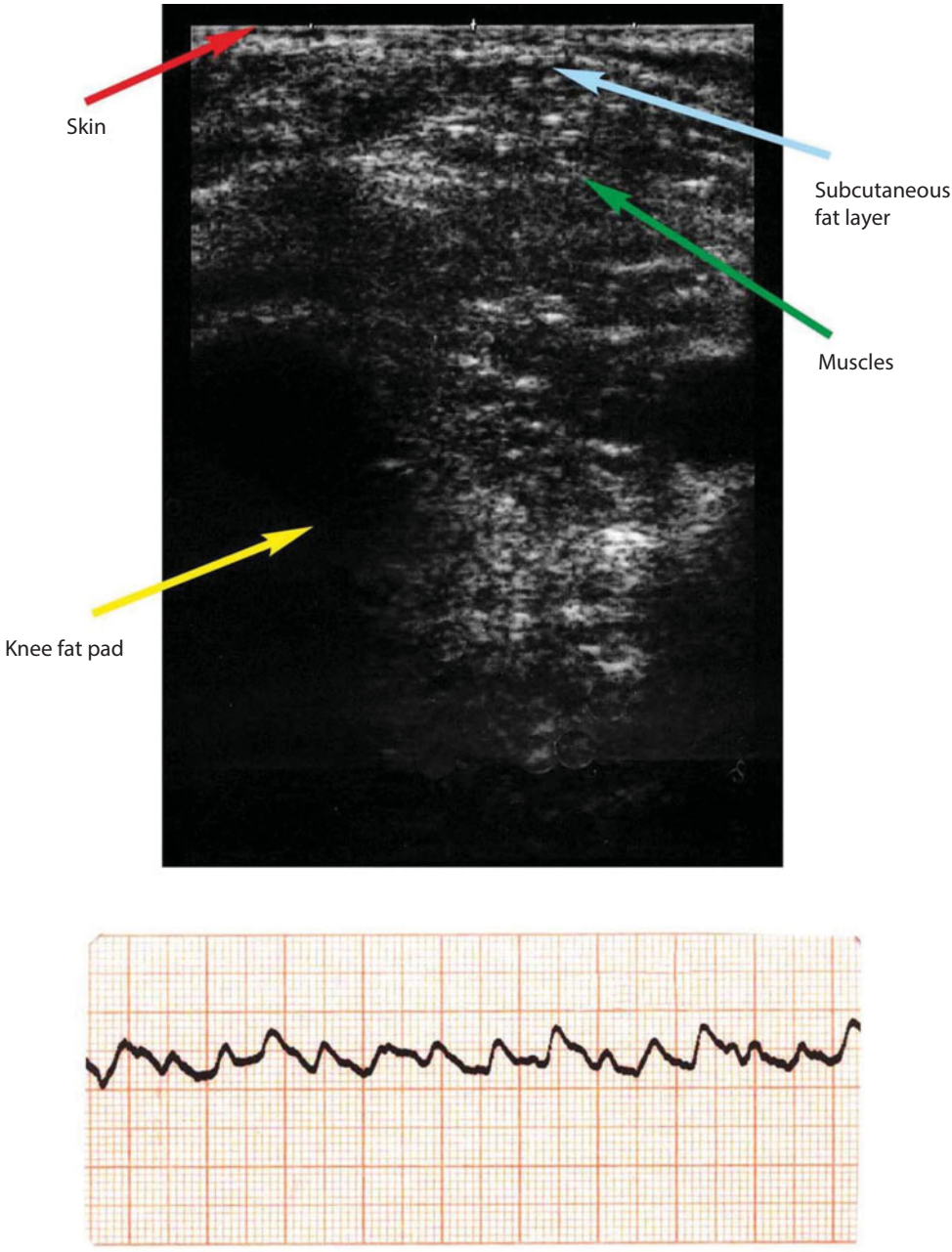

Figure 136 Posterior recess.

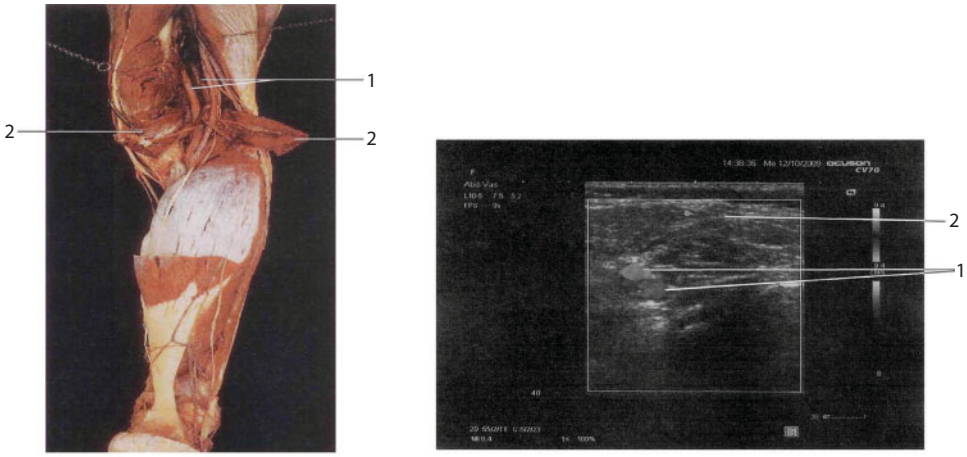

Figure 137 Blood vessels of popliteal fossa.

1. Blood vessels of popliteal fossa; 2. Gastrocnemius muscle.

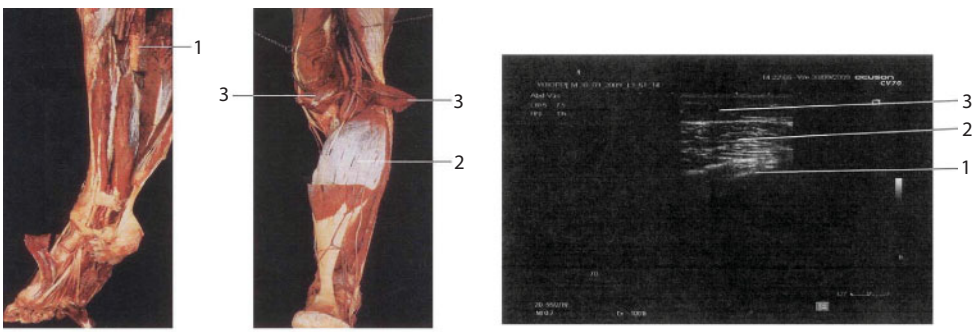

Figure 138 Shin bone muscles, fibular bone.

1. Fibular bone; 2. Salens muscle; 3. Gastrocnemius muscle.

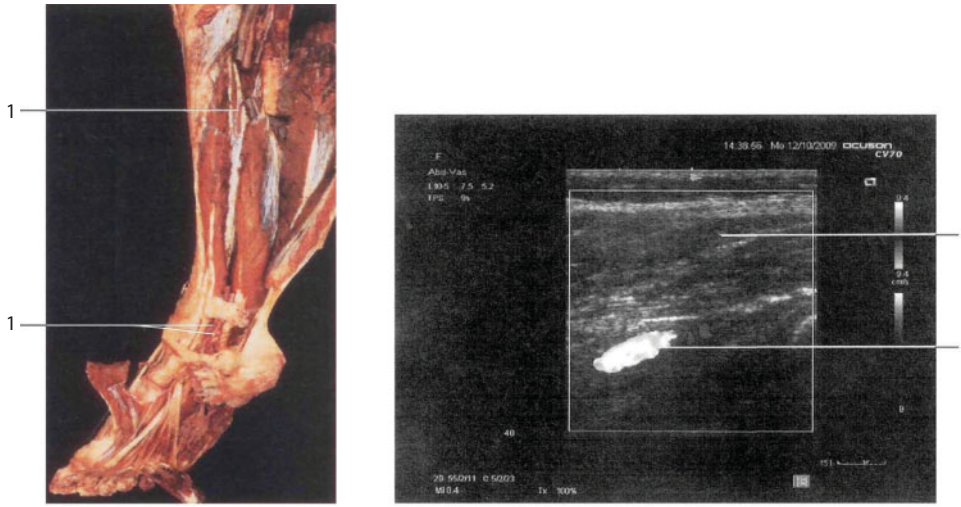

Figure 139 Blood vessels of shin bone, posterior tibial muscle.
1. Posterior tibial muscle; 2. Posterior tibial artery, posterior tibial vein.

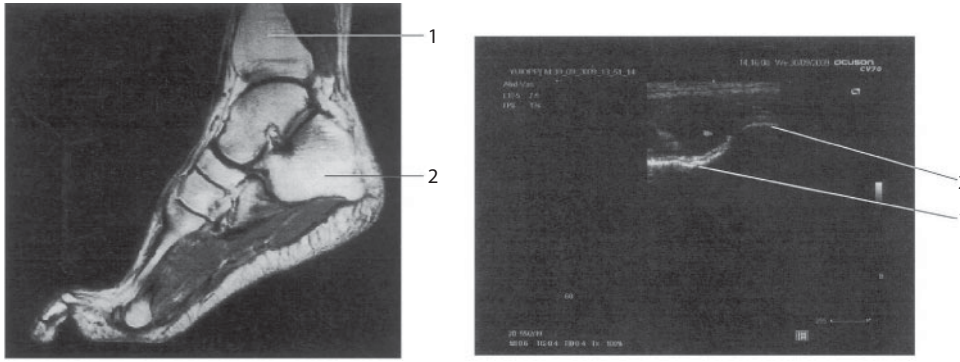

Figure 140 Shin bone, heel bone.
1. Shin bone; 2. Heel bone.

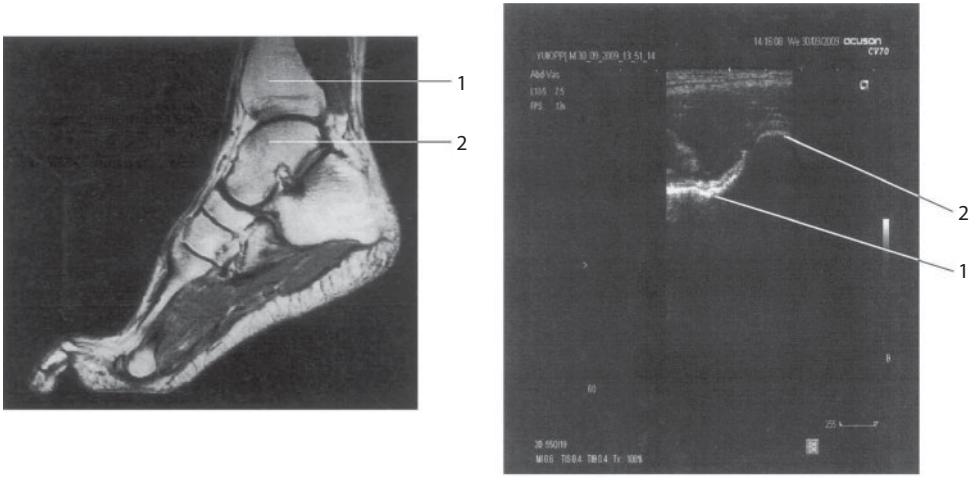

Figure 141 Ankle joint.

1. Shin bone; 2. Ankle joint.

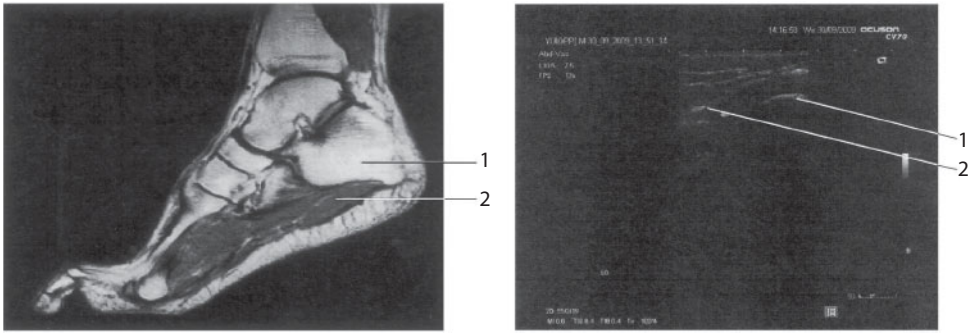

Figure 142 Foot.

1. Heel bone; 2. Short flexor muscle of toes.

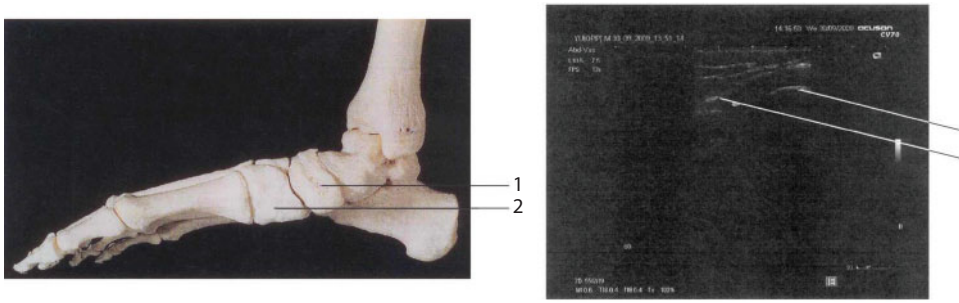

Figure 143 Tarsal bones.

1. Navicular bone; 2. Internal cuneiform tarsal bone.

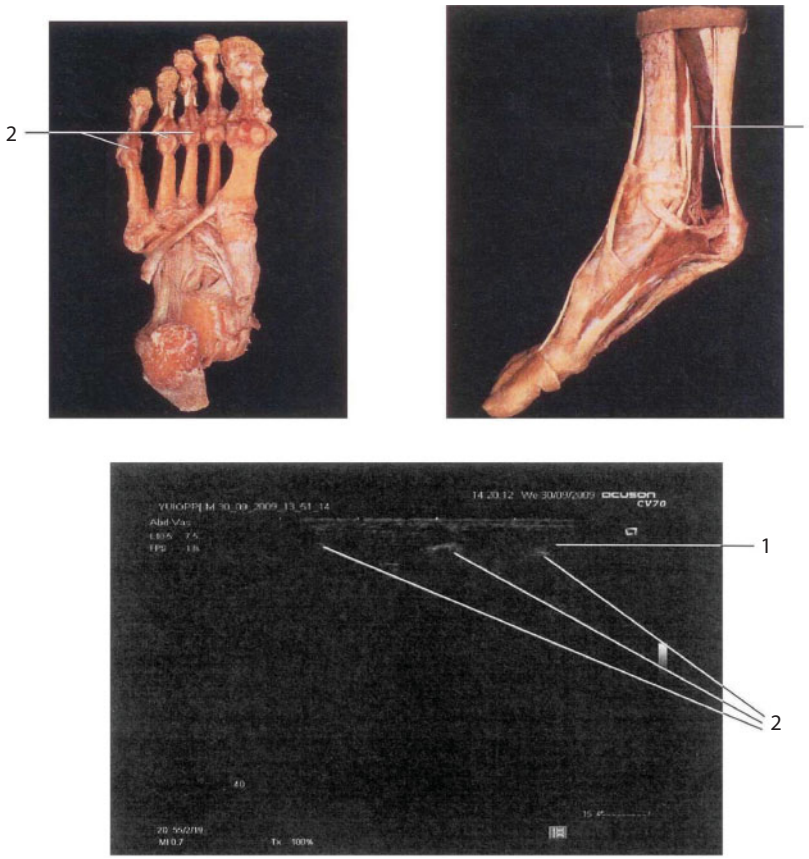

Figure 144 Main joint of toes.

1. Long flexor muscle of toes; 2. Basic toe joints.

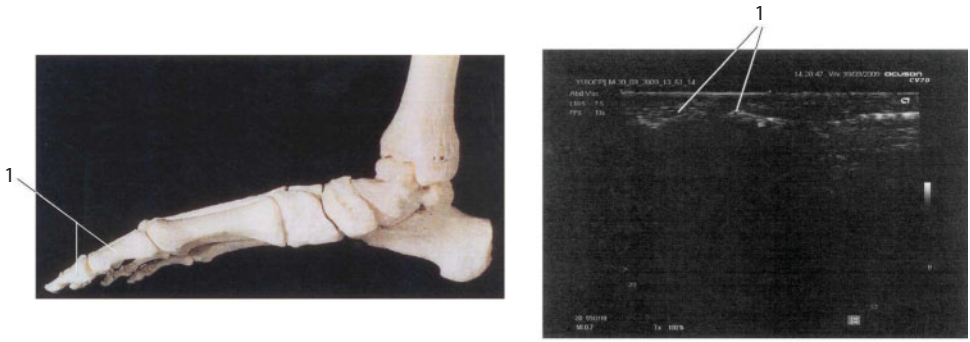

Figure 145 Bones of great toe.

1. Bones of great toe.

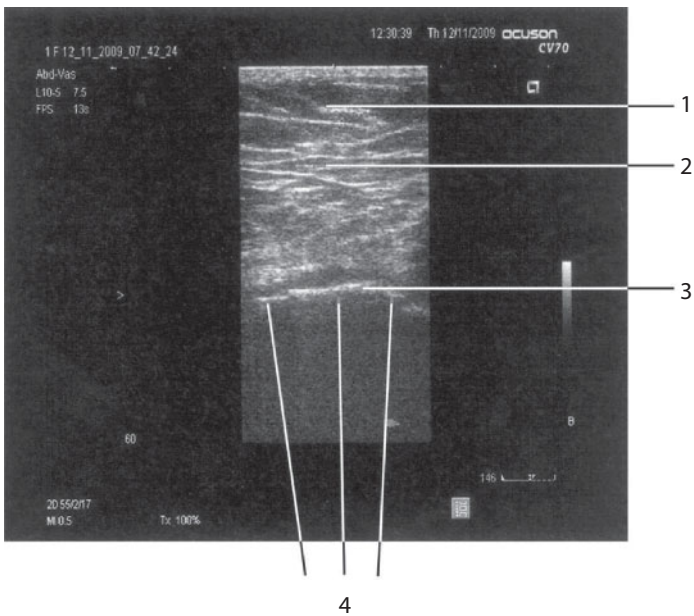

Figure 146 Aseptic necrosis of femoral head.

1. Subcutaneous fat; 2. Gluteus maximus muscle; 3. Femoral head;
4. Aseptic necrosis of femoral head.

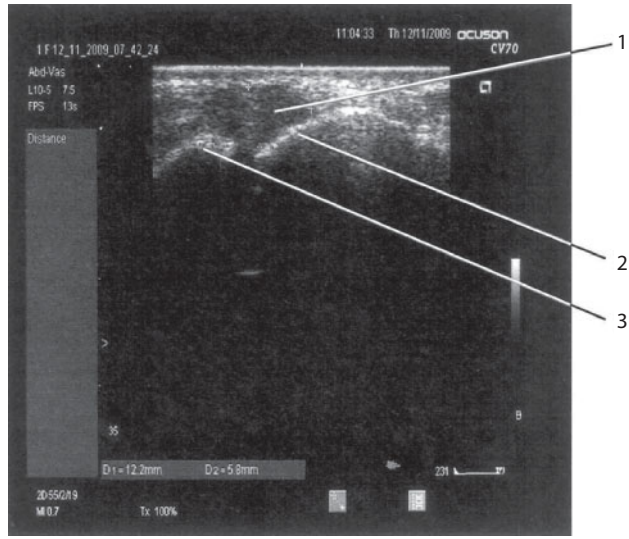

Figure 147 Rheumatoid arthritis.

1. Effusion in bursa of lateral ankle of ankle joint; 2. Lateral ankle; 3. Heel bone.

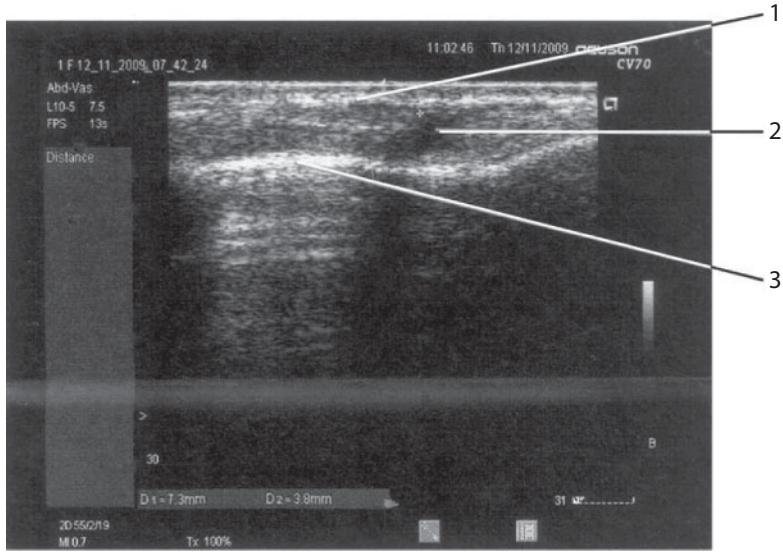

Figure 148 Rheumatoid arthritis.

1. Achilles tendon; 2. Effusion; 3. Shin bone.

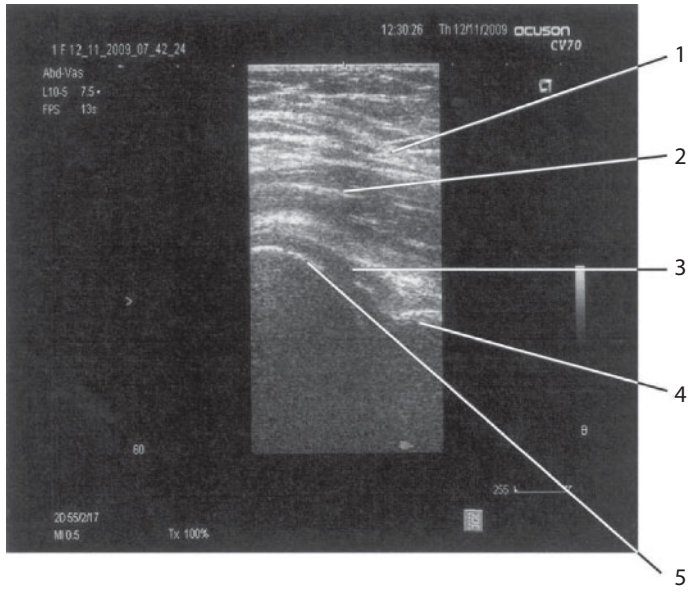

Figure 149 Rheumatoid arthritis.

1. Tailor muscle; 2. Quadriceps muscle of thigh; 3. Effusion; 4. Femoral neck; 5. Femoral head.

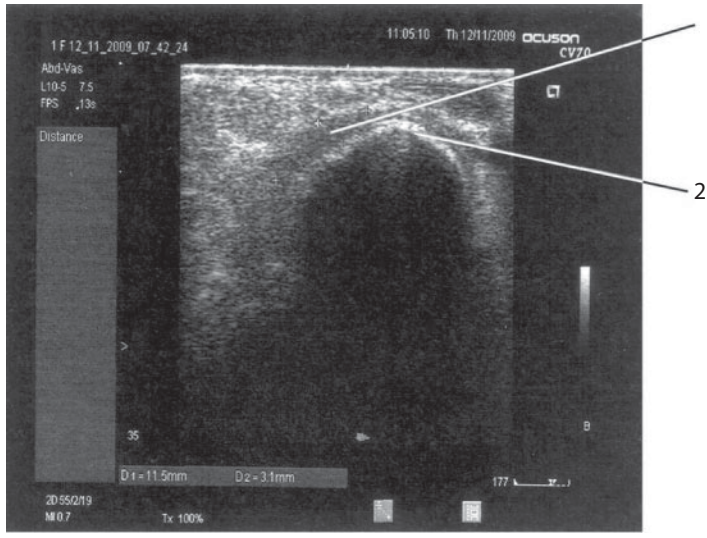

Figure 150 Rheumatoid arthritis.

1. Effusion; 2. Femoral head.

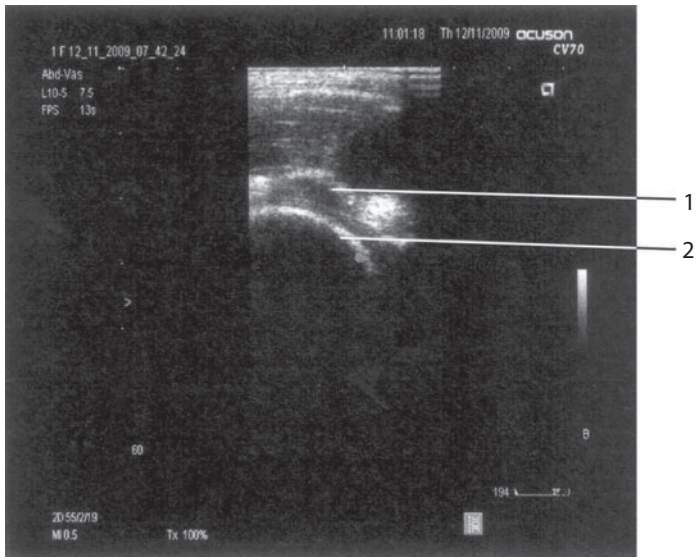

Figure 151 Rheumatoid arthritis.

1. Effusion; 2. Femoral head.

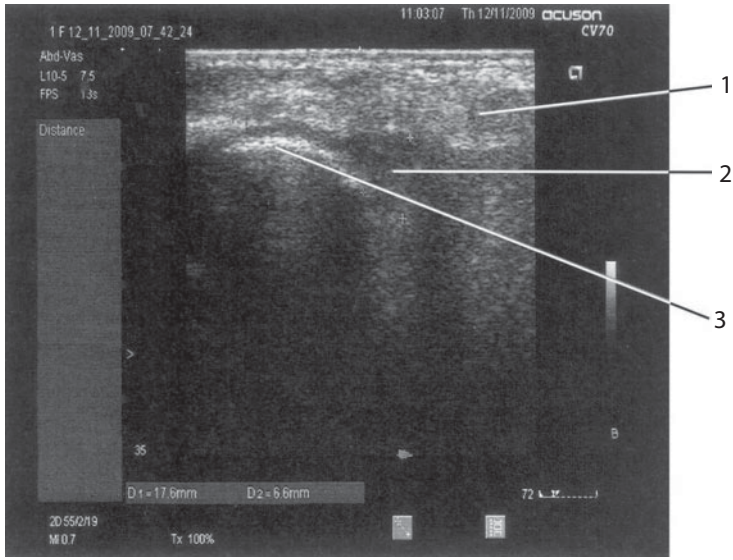

Figure 152 Rheumatoid arthritis.

1. Quadriceps muscle of thigh; 2. Effusion; 3. Femoral head.

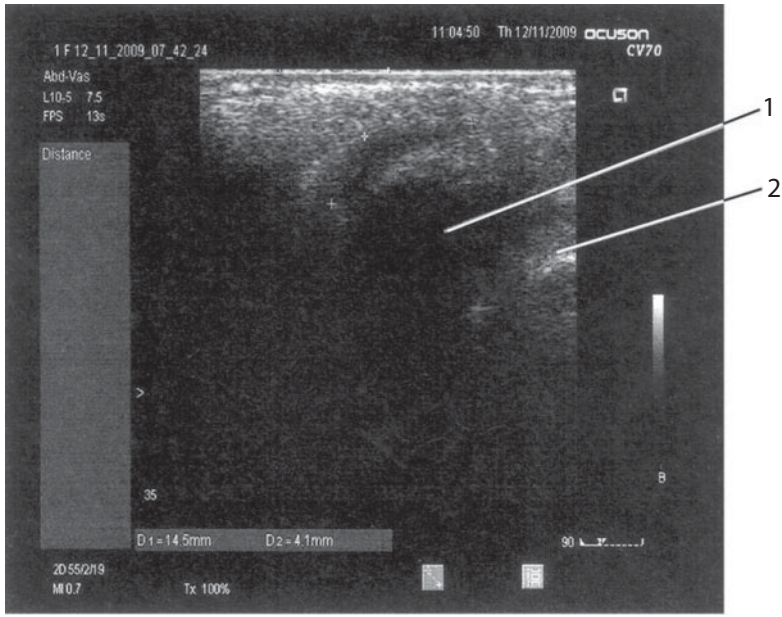

Figure 153 Rheumatoid arthritis.

1. Effusion; 2. Femoral head.

Conclusion

Ultrasonic diagnosis of organ pathology finds continuously increasing use. However, progress in ultrasonic diagnosis does not involve the pathotopographical anatomy, in spite of the diagnostic and prognostic importance of its data. In the literature there is no sufficient data on the use of ultrasonic diagnosis for development and assessment of methods of treatment of various pathologies. The ultrasonic monitoring of surgical procedures is not developed. On the other hand, there are several problems related to insufficient confidence of diagnosis of surgical pathologies, false positive and false negative results of ultrasonic diagnosis, revision of ethiopathogenetic mechanisms of pathology, and development of new methods of effective therapy supported by objective express-methods of monitoring. These problems contribute to the uncertainty of the ultrasonic diagnosis.

Ultrasonic and optical monitoring was used in clinical research of thyroid, mammary glands, knee joints, and prostate. The ultrasonic diagnosis was implemented in the Siemens Acuson Antares and Esote

MyLab 70 apparatuses. Thyroid, mammary glands, and knee joints were scanned using a 5–7 MHz linear sensor. Examination of prostate was performed transrectally using a 5–7.5 MHz sensor.

Optometry was performed using a device for the detection of hemodynamic parameters. The sensitive element consists of two AL 107V LEDs and the FKD-155 photodetector mounted in a sealed cylindrical case, which is connected by cable to a chart recorder. The transrectal examination was implemented using a special probe. ELKAR-6 or EK1T-03M electrocardiographs with magnification of electric signal ×10 or 20 mm/mV were used as recorders. The chart recording rate was 5 mm/sec. Optical calibration was used. The useful signal was obtained using radiation in a broad range of spectral and power characteristics. The wide range of sensitivity of photodetectors and the relative positioning of the optocoupler elements were also important. The duration of a single session of detection of functional parameters was 10–30 sec. The optical calibration allowed the clinical parameters to be compared with each other. The transillumination hemomotorodynamics method is based on monitoring of variation of the pulsation and non-pulsation levels of the optical density of blood flow.

The optical density at the normal and pathological areas of the organ was measured during the tests together with pulse characteristics. The optometry was carried out by applying the optocoupler to the zone of interest. During this procedure the patient's breath should be held. In the thyroid the optical density was 40–48 mA; amplitude of pulse oscillations (APO), 5–10 mm (magnification of electric signal, ×20 mm/mV). The optical density of the mammary gland fibroadenoma was 45-49 mA. The optical density of the mammary gland cyst was 40–42; APO, 2–7 mm. In the norm, the optical density in the bursa of the lateral recess of the knee joint was 40–45 mA, whereas in the deep suprapatellar bursa it was 45 mA; APO, 15–20 mm. In patients with rheumatoid arthritis, the optical density in the bursa of the lateral recess reached 53 mA; APO, 12–18 mm. The prostate optometry was implemented transrectally, applying considerable pressure to the wall of the rectum to measure the optical density of prostate. In patients with chronic

prostatitis, the normal optical density of prostate was 40-55 mA; APO, 3–12 mm (magnification of electric signal, ×10 mm/mV).

Ultrasonic topographical anatomy of the thyroid is represented by the parenchymatous organ consisting of two lobes and an isthmus. Echography usually reveals thyroid tissues in anterior segments of the neck from the thyroid cartilage to the posterior triangle of the neck. In scanning, the posteromedian surfaces of lateral lobes are adjacent to the trachea and inferior larynx. The posterolateral segments almost reach the esophagus. The parathyroid glands are located in the paratracheal cellular tissue behind the thyroid. Ultrasonic scanning in the lateral direction from the thyroid lobes reveals the vascular bundle represented by the common carotid artery and external jugular vein. On each side of the thyroid lobes projections of sternocleidomastoid muscles are observed along the entire length of the neck. A thin skin layer is projected closer to the surface. In case of pathology (thyroid node), the pathotopographical anatomy of the thyroid reveals itself as abnormal correlation between thyroid lobes and isthmus of thyroid: an increase in size toward the isthmus of the thyroid is observed. The anterior adjacent muscles become inaccessible for visualization, thereby indicating disorders in proportions of inter-tissue pattern.

Ultrasonic topographical anatomy of the mammary gland is echographically represented by skin, subcutaneous fat layer, and Cooper ligaments. Echographically, the mammary gland body is a glandular organ containing fat and glandular and connective tissues, as well as a network of milk ducts. Ribs, intercostal muscles, and pleura are located in deeper layers. In the case of fibroadenoma or cyst, the pathotopographical anatomy of the mammary gland is observed. Normal inter-tissue pattern is damaged. Development of the pathological focus reduces the amount of healthy glandular tissue. The differentiation of healthy tissue in the projection of the pathological focus is violated. Deformation of neighboring tissues (skin, subcutaneous fat, milk ducts) is observed.

Ultrasonic topographical anatomy of the knee joint visualizes joint surfaces, lateral ligaments, bursa of lateral recess, muscles, subcutaneous

fat, and skin. In patients with pathological processes (inflammation), pathotopographical anatomy of the knee joint is revealed as liquid in joint bursa and thickening of synovial membranes. Tissue differentiation is disordered; new topographical structures appear in the projection of healthy tissues.

Ultrasonic transrectal examination detects prostate as a triangular structure located in the small pelvis between the urinary bladder, anterior wall of the rectum, and the urogenital diaphragm. The anterior surface is directed toward the symphysis; the posterior surface, toward the rectal ampulla. The inferolateral surfaces are directed to the elevator muscle of the anus. In case of pathological process (chronic prostatitis), modified internal topography of the prostate lobes is visualized. Zonal topography is disrupted.

Further development of the ultrasonic and transillumination optical monitoring procedures can be important for the clinical purpose of detection of specific pathological symptoms, determination of the character of morphological disorders, elaboration of the tactics of surgery under monitoring, and development of new methods of treatment.

Also of Interest

Check out these other titles from Scrivener Publishing

Hydrogeochemistry Fundamentals and Advances Volume 1: Groundwater Composition and Chemistry, by Viatcheslav V. Tikhomirov, ISBN 9781119160397. This three-volume set, beginning with this first volume on the fundamental composition and chemistry of groundwater, is the most comprehensive and up-to-date treatment available on hydrogeochemistry, one of the most important earth sciences in industry and environmental science. *NOW AVAILABLE!*

Project Management in the Oil and Gas Industry, by Mohammed A. El-Reedy, ISBN 9781119083610. The most comprehensive treatment of the processes involved in the management and construction of projects in the oil and gas industry. *NOW AVAILABLE!*

Acid Gas Extraction for Disposal and Related Topics, Edited by Ying Wu, John J. Carroll, and Weiyao Zhu, ISBN 9781118938614. This fifth volume in the series, Advances in Natural Gas Engineering, offers the most in-depth and up-to-date treatment of acid gas extraction for disposal, an important innovation in natural gas engineering. *NOW AVAILABLE!*

Pollution Control Handbook for Oil and Gas Engineering, Edited by Nicholas P. Cheremisinoff, ISBN 9781119117612. This handbook is intended to provide students, petroleum engineers, environmental managers, environmental engineers, and chemical engineers with

practical information and calculation methods for pollution control, management, technologies, and practices, as well as a convenient source of information on equipment and process terminology, and overviews of U.S. and European Community regulations in the oil and gas sector. *NOW AVAILABLE!*

Hydraulic Modeling, by Victor Lyatkher and Alexander M. Proudovsky, ISBN 9781118946190 Combining mathematical and physical modeling, the authors of this groundbreaking new volume explore the theories and applications of hydraulic modeling, an important field of engineering that affects many industries, including energy, the process industries, manufacturing, and environmental science. *NOW AVAILABLE!*

Seismic Loads, by Victor Lyatkher, ISBN 9781118946244. Combining mathematical and physical modeling, the author of this groundbreaking new volume explores the theories and applications of seismic loads and how to mitigate the risks of seismic activity in buildings and other structures. *NOW AVAILABLE!*

Fundamentals of Biophysics, by Andrey B. Rubin, ISBN 9781118842454. The most up-to-date and thorough textbook on the fundamentals of biophysics, for the student, professor, or engineer. *NOW AVAILABLE!*

i-*Smooth Analysis: Theory and Applications*, by A.V. Kim, ISBN 9781118998366. A totally new direction in mathematics, this revolutionary new study introduces a new class of invariant derivatives of functions and establishes relations with other derivatives, such as the Sobolev generalized derivative and the generalized derivative of the distribution theory. *NOW AVAILABLE!*

Reverse Osmosis: Design, Processes, and Applications for Engineers 2nd Edition, by Jane Kucera, ISBN 9781118639740. This is the most comprehensive and up-to-date coverage of the "green" process of reverse osmosis in industrial applications, completely updated in this new edition to cover all of the processes and equipment necessary to design, operate, and troubleshoot reverse osmosis systems. *NOW AVAILABLE!*

Pavement Asset Management, by Ralph Haas and W. Ronald Hudson, with Lynne Cowe Falls, ISBN 9781119038702. Written by the founders of the subject, this is the single must-have volume ever published on pavement asset management. *NOW AVAILABLE!*

Open Ended Problems: A Future Chemical Engineering Approach, by J. Patrick Abulencia and Louis Theodore, ISBN 9781118946046. Although the primary market is chemical engineers, the book covers all engineering areas so those from all disciplines will find this book useful. *NOW AVAILABLE!*

WILEY END USER LICENSE AGREEMENT

Go to www.wiley.com/go/eula to access Wiley’s ebook EULA.